ABSTRACT

Title: ON THE RAPID INTENSIFICATION OF HURRICANE WILMA (2005)

Hua Chen, Doctor of Philosophy, 2012

Directed By: Professor Da-Lin Zhang
Department of Atmospheric and Oceanic Science

Previous studies have focused mostly on the roles of environmental factors in the rapid intensification (RI) of tropical cyclones (TCs) due to the lack of high-resolution data in the inner-core regions. In this study, we examine the RI issue by analyzing 72-h cloud-permitting model predictions of Hurricane Wilma (2005) with the Weather and Research Forecast (WRF) model at the finest grid sizes of 1-2 km. The 72-h predictions cover Hurricane Wilma's initial 18-h spin up, an 18-h RI and the subsequent 36-h weakening stage. The model prediction uses the initial and lateral boundary conditions, including a bogus vortex, that are identical to the Geophysical Fluid Dynamics Laboratory's then-operational data, except for the time-independent sea surface temperature (SST) field. The model predicts an RI rate of more than 4 hPa $h^{-1}$ for an 18-h period, with the minimum central pressure of less than 889 hPa.

It was found that an upper-level warm core forms in the same layer as the upper outflow, in coincidence with the onset of RI. The warm core results from the subsidence of stratospheric air associated with the detrainment of convective bursts (CBs). The upper divergent outflow appears to play an important role in protecting

the warm core from ventilation by environmental flows. Results also show the development of more CBs preceding RI, but most subsidence warming radiates away by internal gravity waves and storm-relative flows. In contrast, many fewer CBs occur during RI, but more subsidence warming contributes to the balanced upper-level cyclonic circulation in the warm core (as intense as 20°C) region. Furthermore, considerable CB activity can still take place in the outer eyewall as the storm weakens during its eyewall replacement. Sensitivity simulations reveal that the upper-level warm core and CB activity depend critically on warm SST. We conclude that significant CB activity in the inner-core regions is an important ingredient in generating an upper-level warm core that is hydrostatically more efficient to the RI of TCs, given all the other favorable environmental conditions.

The formation of a divergent upper-level outflow that prevents the warm core from ventilation is examined through asymmetric contraction processes associated with new rainbands forming inside the eyewall. The relative vorticity, generated in the downshear region and then advected cyclonically downstream, can induce convergence in the boundary layer. With the aid of high moisture content, the convergence can trigger deep convection and contribute to the formation of the new rainbands. Finally, the importance of a small eye size is demonstrated using three widely accepted approximations: angular momentum conservation, solid body rotation and gradient wind balance. Results show that the storm intensifies much faster for a given contraction speed if the eye size is small.

# ON THE RAPID INTENSIFICATION OF HURRICANE WILMA (2005)

By

Hua Chen

Dissertation submitted to the Faculty of the Graduate School of the
University of Maryland, College Park, in partial fulfillment
of the requirements for the degree of
Doctor of Philosophy
2012

Advisory Committee:
Professor Da-Lin Zhang, Chair
Professor James Carton
Professor Chuan Liu (Dean's representative)
Professor Xinzhong Liang
Professor Kayo Ide
Professor Takemasa Miyoshi

# Acknowledgements

First and foremost, my deepest gratitude goes to my thesis advisor, Prof. Da-Lin Zhang, for providing me with valuable guidance not only in my academic life but also my personal life. Thanks for his endless encouragement and patience with my usually long learning curve. I also would like to thank Prof. James Carton for partially funding my research such that I can continue my Ph.D research.

I would also like thank Drs. Chanh Kieu and Wallace Hogsett for their helpful discussions in research, Xiaolei and Lin for hanging out and being there for me.

Finally, I wish to thank my parents for their kind support and Yue for the encouragement over the years. I would not have gone so far without them.

# Table of Contents

# List of Figures

# List of Abbreviations

| | |
|---|---|
| AVHRR: | Advanced Very High Resolution Radiometer |
| CAPE: | Convective Available Potential Energy |
| CB: | Convective Burst |
| CISK: | Conditional Instability of the Second Kind |
| ERC: | Eyewall Replacement Cycle |
| GFDL: | Geophysical Fluid Dynamics Laboratory |
| GFS: | Global Forecast System |
| HRD: | Hurricane research division |
| ITCZ: | Inter-Tropical Convergence Zone |
| MPI: | Maximal Potential Intensity |
| NCEP: | National Centers for Environmental Prediction |
| NHC: | National hurricane center |
| NOAA: | National Oceanic and Atmospheric Administration |
| OLR: | Outgoing Long wave Radiation |
| PMIN: | Mininum surface pressure |
| PV: | Potential vorticity |
| RI: | Rapid Intensification |
| RMW: | Radius of maximum wind |
| SRF: | Storm Relative Flow |
| SST: | Sea Surface Temperature |
| TD: | Tropical Depression |
| TS: | Tropical Storm |

VMAX: Maximum surface wind

VWS: Vertical Wind Shear

WISHE: Wind-Induced Surface Heat Exchange

WRF: Weather Research and Forecasting model

# Chapter 1. Introduction

## *1.1 Background*

Rapid intensification (RI), defined as a deepening rate of greater than 42 hPa $day^{-1}$ (or 1.75 hPa $hr^{-1}$) in the minimum central pressure ($P_{MIN}$) (Holliday and Thompson 1979) or 15 m $s^{-1}$ per day in the surface maximum tangential wind ($V_{MAX}$) (Kaplan and DeMaria 2003), has remained a daunting task for forecasters. The main difficulty behind the RI forecast is the lack of high resolution data, from both the observation and the model simulation, that prevents the in-depth understanding of multiscale interactions accounting for RI. Since 2008 (Kaplan and DeMaria 2010), RI forecast has been declared as top forecast priority by the Tropical Prediction Center/NationalHurricane Center (TPC/NHC) (NHC 2008).

Despite the lack of the high resolution data, previous studies do provide some understanding on RI from the perspective of environmental factors, such as high sea-surface temperature (SST), weak vertical wind shear (VWS), high relative humidity in the lower troposphere, easterly upper-tropospheric flow, and weak forcing from upper-level troughs and cold lows. However, the information of large scale environment factors cannot paint the whole picture of RI process and some storms still go through RI against the presence of unfavorable factors. For example, Hurricane Guillermo (1997) intensified rapidly in spite of the presence of 8 m $s^{-1}$ VWS. In order to accurately forecast RI, the internal physical processes that account for RI and storm structural change associated with RI have to be fully addressed.

Previous observation showed that the intensification of storms was always associated with the size contraction, which can be categorized into two different processes: asymmetric contraction and symmetric contraction. In these two processes, the symmetric contraction has been relatively well addressed. Shaprio and Willoughby (1982) applied Eliassen's (1951) model of forced secondary circulation to tropical cyclones and concluded that the height of standard isobaric surfaces fell rapidly inside the radius of maximum wind (RMW) and much more slowly outside it in response to a heat or a momentum source near a RMW, leading to the contraction of RMW and eyewall. In contrast, asymmetric contraction remains an open issue. Some studies (Montgomery and Kallenbach 1997; Moller and Montgomery 1999; Shapiro 2000) showed that asymmetric moist convection can intensify the axisymmetric primary circulation through momentum transports by vortex Rossby waves. However, Nolan and Grasso (2003) and Nolan et al. (2007) have recently demonstrated purely asymmetric heat sources cause vortex weakening. Moller and Shapiro (2005) points out that the small eddy kick created by the additional diabatic heating asymmetry leads to a substantially amplified long-term change in the azimuthally averaged vortex, with episodes of strong relative weakening and strengthening following at irregular interval.

Recently, Harnos and Nesbitt (2011) showed most of storms that go through RI bear a symmetric ring of convection. This indicates that symmetric contraction accounts for RI at a great extent. Then what is the role of asymmetric contraction? What are the physical mechanisms that make symmetric contraction favor RI? The threshold value for a storm to qualify RI is 1.75 hPa $hr^{-1}$ but the deepening rate can be

as large as 9 hPa $hr^{-1}$ in some cases. What determines the drastically different deepening rate?

No matter asymmetric contraction or symmetric contraction, the intensification of a storm has to take the form of a strengthening warm core. Previous studies (Zhang and Fritsch 1988; Hirschberg and Fritsch 1993) have pointed out that the same magnitude of warm anomaly will be more efficient in reducing surface pressure if it is imposed at higher altitude in the troposphere based on the hydrostatic approximation. This implies that the storm with an upper level warm core tends to experience RI. How does the upper level warm core form? Observational studies showed that convective bursts can induce significant warming at upper level and they are usually very active in genesis stage and pre-RI stage (Rodgers et al. 1998, 2000; Price et al. 2009; Guimond et al. 2010; Fierro et al. 2011). CB can also stretch vorticity at the low level exponentially and contribute to the spin up of the hurricane vortex. All these studies imply that convective bursts could be a critical process that is responsible for RI.

### *1.2 Objectives of this study*

In order to address the question raised in section 1.1, we select a very unique case, Hurricane Wilma (2005). Year 2005 is a very special one. There are 26 named storms, 4 of which reached category 5, including Hurricane Katrina, Rita and Wilma. Warm SST is one major reason that accounts for the usually active hurricane season in 2005. The unique features of Hurricane Wilma include: a record intensity in the Atlantic basin – 882 hPa, a record intensification rate – 9 hPa $hr^{-1}$ for 6 consecutive hours, and a record small eye size –5 km in diameter.

The objectives of this study are to (i) obtain a successful simulation of Hurricane Wilma (2005) with a cloud-resolving version of the WRF model at the high horizontal and vertical resolutions, particularly the RI and some important structural changes during its pre-RI and RI stages, as verified against all possible observations; and (ii) document the structures and evolution during the life cycle of the storm. Assuming that such a successful simulation can be obtained, the third objective is to diagnose the mechanisms whereby RI occurs, using the high-resolution, dynamically consistent four-dimensional model data. The fourth objective of this study is to examine some important processes leading to the RI of this storm through conducting sensitivity simulations by changing certain physical parameters in the control simulation.

Two main scientific issues regarding RI to be addressed in this study include (i) What dynamical and thermodynamical processes in the inner-core regions account for the RI of Hurricane Wilma (2005)? (ii) What is the relationship between the inner-core processes and the large-scale factors during the RI of the storm?

The next chapter presents a 72-h control prediction of Hurricane Wilma (2005) with the finest grid size of 1 km and the GFDL-then operational data. The model prediction will also be validated against available observations. Chapter 3 shows the relationship between an upper-level warm core, convective bursts (CBs), sea surface temperatures (SSTs) and surface pressure falls in relation with the RI of this storm by analyzing the high resolution model prediction. Chapter 4 demonstrates that a small symmetric eyewall is related to RI and shows how it forms in this case. A summary

and concluding remarks are given in the final chapter. Future work related to this case study will also be discussed.

# Chapter 2. Numerical prediction

## *2.1. Previous work*

The hurricane is one of the most dangerous natural hazards to human society and the environment. Thus, it is of great importance to accurately predict many hours in advance a hurricane's track, intensity, and rate of intensity change, as well as the associated torrential rainfall. Due to the complex nature of the physics involved in the development of hurricanes, our forecast capability depends highly on guidance provided by various numerical (dynamical and statistical) models. Although there have been continuing improvements in forecasting hurricane track and landfall location, very little progress has been seen in intensity forecasting during the past two decades (Marks et al. 1998; Rappaport et al. 2009).

Apparently, hurricane intensity change involves multiscale nonlinear interactions of different phenomena and variables (Marks et al. 1998; Shen et al. 2010). Such interactions include the SST, ocean heat content, vertical wind shear (VWS), environmental moisture, inner-core dynamics and thermodynamics, cloud microphysics, and air–sea interaction processes, which are not all well represented by today's hurricane models. Indeed, Rappaport et al. (2009) report that today's dynamical hurricane models have not reached the skill level of statistical intensity models in many cases. In particular, current hurricane models tend to underpredict very strong storms and overpredict very weak storms. Moreover, many inner-core structures, such as narrow spiral rainbands, small eye size, polygonal eyewalls, and eyewall replacement cycles (ERCs), cannot be captured by current operational

models. These inner core structures appear to be closely related to intensity changes and the final intensity of hurricanes.

It has long been recognized that our ability to understand and predict hurricane intensity changes is hampered partly by the lack of realistic four-dimensional high-resolution data, and partly by deficiencies in hurricane models, including the model initial conditions. Earlier observational studies, based on the flight-level and satellite data, could only examine hurricane vortex structures and precipitation characteristics (e.g., Parrish et al. 1982; Marks and Houze 1987). Use of Doppler radar data can reveal many inner-core features, such as eyewall replacement morphology, and low-level wind variations over coastal and inland regions (e.g., Willoughby et al. 1982; Marks and Houze 1984; Bluestein and Hazen 1989; Blackwell 2000; Black and Willoughby 1992). Nevertheless, the lack of high-resolution observations often precludes a detailed analysis and description of structural changes, and the cause and effect of the underlying physical processes taking place in intensifying hurricanes. These structural changes appear to be closely related to significant intensity fluctuations and redistributions of precipitation and rotational winds in hurricanes (e.g., Hogsett and Zhang 2009).

On the other hand, considerable progress has been made in cloud-permitting simulations of hurricanes during the past 15 years (see Liu et al. 1997, 1999; Davis and Bosart 2001; Braun 2002; Rogers et al. 2003; Zhu et al. 2004;Yang et al. 2008). These studies have provided novel insights into the inner-core structures and evolutionary patterns of some hurricanes that are closely related to hurricane intensity changes. Using hurricane models at cloud-permitting scales ($\Delta x$ = 2–6 km), it is now

possible to reproduce reasonably well the asymmetric structures of the eye, the eyewall, spiral rainbands, the radius of maximum winds (RMW), ERC scenarios, and other inner-core features. Zhu et al. (2004) show, using the finest grid size of 4 km, that the ERC of Bonnie (1998), accounting for its pronounced intensity changes, occurs as it moves from a strong to a weak VWS environment.

Despite the above-mentioned encouraging achievements, the previous studies also indicate that using cloud-permitting models and simply increasing the horizontal grid resolution do not always lead to a successful simulation of hurricanes (e.g., Davis et al. 2010). Numerical simulation of hurricanes depends on the model representation of various cloud microphysical processes (Zhu and Zhang 2006a; Li and Pu 2008; Davis and Bosart 2002), the planetary boundary layer (PBL) parameterizations (Braun and Tao 2000), vertical resolution (Zhang and Wang 2003; Kimball and Dougherty 2006), and the initial vortex structures (Zhu et al. 2002). Some physics parameterizations appear to depend on grid resolutions and coupling with other schemes. In addition, some real-data simulations have also shown complicated scale interactions involved in hurricane intensity changes (Liu et al. 1999; Hogsett and Zhang 2009).

While the predictability of hurricane intensity change is limited, it is even more challenging to predict the rapid intensification (RI) of hurricanes, where RI is defined as a deepening rate of greater than 1.5 hPa $h^{-1}$ in the minimum central pressure ($P_{MIN}$) or 15 m $s^{-1}$ per day in the surface maximum tangential wind ($V_{MAX}$) (Kaplan and DeMaria 2003). So far, the subject of RI has mostly been discussed from the perspective of environmental factors owing to the lack of high-resolution data in

the inner-core regions of these storms. Previous studies indicate that warm SST, high relative humidity, and lower VWS are the most favorable environmental factors for RI hurricanes. Kaplan and DeMaria (2003) suggest that a hurricane tends to have the greatest chance of undergoing RI when it is far from its maximum potential intensity (Emanuel 1986) in a favorable environment. Recently, Rogers (2010) demonstrated the ability of a cloud-permitting model to reproduce the RI (at a rate of about 0.8 hPa $h^{-1}$ and 15 m $s^{-1}$ $day^{-1}$) of Hurricane Dennis (2005) with the finest grid size of 1.667 km.

In contrast to RI, the ERC has received more attention during the past few decades. Since Fortner (1958) first described this phenomenon within Typhoon Sara (1956), a number of observational studies have shown that during the development of some intense hurricanes spiral rainbands may form a second eyewall surrounding an inner eyewall. As the outer eyewall contracts and consolidates, the inner one starts to dissipate. As a result, the hurricane stops intensifying and begins to weaken with rising $P_{MIN}$ and decreasing $V_{MAX}$. Some time later, the outer eyewall replaces the inner one and becomes the new primary eyewall. After an eyewall succession, the hurricane may resume intensification if conditions are still favorable. Nevertheless, the mechanism by which double eyewalls form still remains elusive due to the lack of high-resolution data, and predicting their occurrences in an operational setting is still a very challenging task.

Therefore, it is the intention of this study to fill in the gaps required to provide a better understanding and aid in the prediction of the RI and ERC processes through a 72-h (0000 UTC 18 October–0000 UTC 21 October 2005) numerical investigation

of Hurricane Wilma (2005), a storm that demonstrated record-breaking RI, maximum intensity, and small eye size. In particular, the Geophysical Fluid Dynamics Laboratory's (GFDL) then-operational model, and several other hurricane models, severely underestimated the peak intensity and RI rate of Wilma. To establish the credibility of the results of diagnostic and sensitivity simulations to be presented in subsequent parts of this series of papers, the purposes of Part I are to (i) document the life cycle of Hurricane Wilma from its genesis to final dissipation after passing the Florida Peninsula, and some inner-core structures during its RI stage; (ii) examine to what extent Wilma's RI could be predicted using the then-operational GFDL model's initial and lateral boundary conditions but different configurations with the Weather Research and Forecast Model (WRF); and (iii) demonstrate that some inner-core structures (e.g., small eye size, ERCs) in relation to the record-breaking RI and intensity changes could be predicted when a high-resolution cloud-permitting model is used.

The next section provides a brief overview of Hurricane Wilma (2005). Section 2.3 describes the model configurations used for the prediction of Wilma, as compared to the then-operational GFDL model configurations. Section 2.4 presents verification of the model-predicted storm structures against various observations. Section 2.5 shows some model-predicted inner-core structures and structural changes during Wilma's RI stage in order to facilitate the presentation of our model results in the subsequent parts of this series of papers. A summary and some concluding remarks are given in the final section in this chapter.

### *2.2. Case overview*

Hurricane Wilma (2005) was the most powerful hurricane ever recorded over the Atlantic basin, with a $P_{MIN}$ of 882 hPa and a $V_{MAX}$ that was larger than 80 m $s^{-1}$, as well as the record-breaking deepening rates of 9.0 hPa $h^{-1}$, or 54 hPa (6 h) $^{-1}$, or 83 hPa (12 h) $^{-1}$ during its 18-h RI phase. The National Centers for Environmental Prediction–National Center for Atmospheric Research (NCEP–NCAR) reanalysis and satellite imagery indicate that the formation of Wilma can be traced back to a broad monsoon like low-tropospheric trough in the northwestern Caribbean Sea as early as 0000 UTC 11 October. This trough was later split into two parts: the eastern portion moved northeastward and merged with an extratropical cyclone, while the southern portion stayed and grew into a tropical depression (TD) offshore of Jamaica by 1800UTC 15October when a concentrated area of deep convection developed on its southeastern side.

Figure 2.1 shows the representative large-scale environment in which this TD was embedded during the subsequent few days. That is, in the midtroposphere the TD area was sandwiched between a subtropical high to its northwest (hereafter referred to as the Mexican high) and the Atlantic high to its east. This produced a weak steering current, driving the TD slowly west- to west-southwestward for about a day and then southwest- to southward for another two days. During this period, convective clouds within the TD were slowly organized with the low-level southwesterly moisture supply from the intertropical convergence zone (ITCZ), but under the influence of a dry-air intrusion in the north-northeasterly flow, as indicated by a dry slot over the

Gulf of Mexico, and in the easterly flow (Fig. 2.2). Around 0600 UTC 17 October, the TD was upgraded to Tropical Storm (TS) Wilma as an intense convective burst

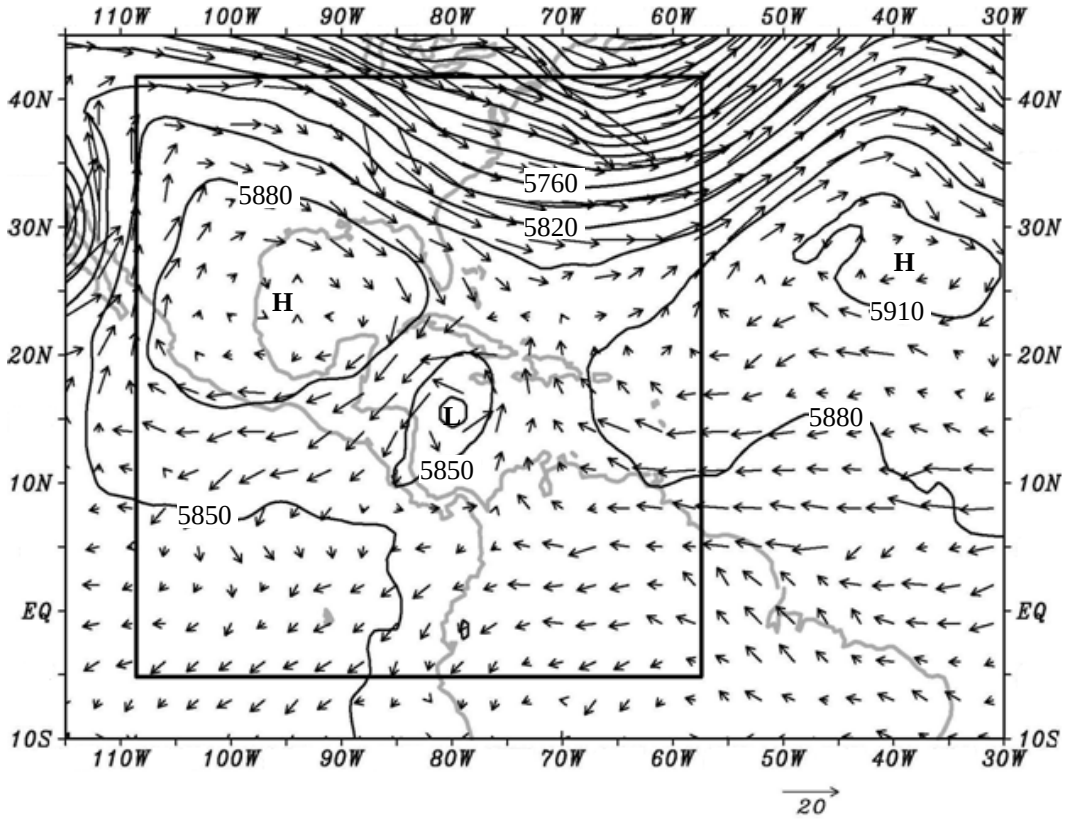


Figure 2.1: Horizontal distribution of geopotential height, at intervals of 30 m, superimposed with horizontal flow vectors at 500 hPa from the NCEP GFS analysis at 0000 UTC 18 October 2005. The inner frame shows the outermost model domain used for the present study.

occurred on the southern side of the cyclonic circulation where an ample moisture supply was present. It strengthened to hurricane intensity early on 18 October as it turned west-northwestward (Figs. 2.3 and 2.4).

Starting from 1800 UTC 18 October, an explosive deepening (RI) episode began when Wilma traversed an area of high ocean heat content. This RI period was sustained for 12 h until 0600 UTC 19 October, with a 29-hPa drop in the first 6 h and

a 54-hPa drop in the second 6 h (Fig. 2.4). Of interest is that corresponding to the respective 29 and 54 hPa $(6\ h)^{-1}$ drops in $P_{MIN}$ are a 10 m $s^{-1}$ increase in $V_{MAX}$ during the first 6 h but only a 5 m $s^{-1}$ increase during the second 6-h period. At first, this 54-hPa drop in $P_{MIN}$ does not appear to be consistent with its corresponding 5 m $s^{-1}$ increase in $_{VMAX}$, as compared to the pressure–wind relation during the first 6-h RI period. Recently, Kieu et al. (2010) developed a new pressure–wind relationship, based on the analytical model of Kieu and Zhang (2009), and then tested it using preliminary model-predicted data from Hurricane Wilma (2005). Their work indicates that $P_{MIN}$ drops at a rate much faster than the square of $V_{MAX}$. In particular, when the eye size becomes very small, a slight contraction of the RMW can lead to a large drop in $P_{MIN}$ but small increases in VMAX due to the presence of stronger frictional effects [see Eq. (8) in Kieu et al. (2010)]. Apparently, the pronounced increase of $V_{MAX}$ in the first 6 h could be attributed to the rapid eyewall contraction, based on the conservation of angular momentum, whereas the increased frictional effects or radial winds in the small-sized eyewall region could account for the relatively small increases in $V_{MAX}$ but the more dramatic $P_{MIN}$ drops during the second 6 h.

During the 12-h RI period, a U.S. Air Force reconnaissance flight indicated that the hurricane eye did contract to a very small size, that is, about 5 km in diameter, which is the smallest eye known to the staff of the National Hurricane Center (Pasch et al. 2006). The storm reached its peak intensity at 1200 UTC 19 October with an estimated $P_{MIN}$ of 882 hPa (Fig. 2.4), which broke the record of 888 hPa set by Hurricane Gilbert (1988) in the Atlantic basin. During the following 24 h, Wilma weakened from 882 to 910 hPa. Satellite imagery reveals that an ERC

accounts for this weakening, which replaces the original pinhole eye with a larger one of about 70 km in diameter. A second ERC occurred near the landfalls at Cozumel Island and the northern tip of the Yucatan Peninsula. As a result, Wilma weakened further from 910 to 960 hPa during this 60-h period. After meandering over the northern tip of the Yucatan Peninsula for about a day, Wilma turned north and emerged into the southern Gulf of Mexico around 0000 UTC 23 October, with a $V_{MAX}$ of 43 m $s^{-1}$. Later on, the storm reintensified over the southeastern Gulf of Mexico when it moved northeastward across a warm ring, and made a third landfall at southwestern Florida near Cape Romano around 1030 UTC 24 October. See Pasch et al. (2006) for more details.

In the present study, we will focus more on the predictability of the record-breaking RI and $P_{MIN}$, the formation of various inner-core structures in relation to the record-breaking intensity changes, the small-size eyewall, and an ERC that occurred during the period of 1800 UTC 18 October–0000 UTC 21 October. The then-operational GFDL model underpredicted the storm with negative mean errors of 9, 11, and 15 m $s^{-1}$ for 24-, 48-, and 72 h forecasts, respectively. Its two best forecasts, initialized at 1800 UTC 17 October and 0000 UTC 18 October, produced a peak intensity of 924 hPa with a peak deepening rate of 2.5 hPa $h^{-1}$. The abovementioned inner-core structures could not be generated due to the use of coarse (> 8 km) resolutions and parameterized convection. Blanton (2008) has attempted to simulate this storm with the finest grid size of 2 km, but produced a peak intensity of 922 hPa occurring 12 h later than observed, similar to the then-operational GFDL model's forecasts.

### *2.3. Model description*

In this study, Hurricane Wilma (2005) is explicitly predicted using a two-way interactive, movable, quadruply nested (27/9/3/1 km) grid, nonhydrostatic version of the Advanced Research core of the WRF (ARW, version 3.1.1) with the finest grid resolution of 1 km (see Skamarock et al. 2005). The WRF is initialized at 0000 UTC 18 October 2005, which is about 18 h before the onset of RI, and integrated for 72 h, covering the initial rapid spinup, the RI, and the subsequent weakening period associated with an ERC. The model initial and lateral boundary conditions are interpolated from then-operational GFDL model data, that is, from NCEP's Global Forecast System (GFS) analysis, including a bogus vortex based on Kurihara et al.'s (1993) vortex specification scheme. SST is interpolated from the National Oceanic and Atmospheric Administration's (NOAA) Advanced Very High Resolution Radiometer (AVHRR) SST data at 0.25° resolution at 0000 UTC 18 October, and it is held constant in time (see Fig. 2.3). The time-independent SST is used because of the small changes observed along the storm's track during the RI period. Of interest is that SST became warmer, rather than colder (Leipper 1967; Bender et al. 1993; Zhu and Zhang 2006b), to the right of the track after passing the peak intensity (see the SST differences contoured in Fig. 2.3). It is evident that the SST in the range of 29–30°C along the track provides favorable conditions, through the air–sea interaction, for the generation of such an intense hurricane.

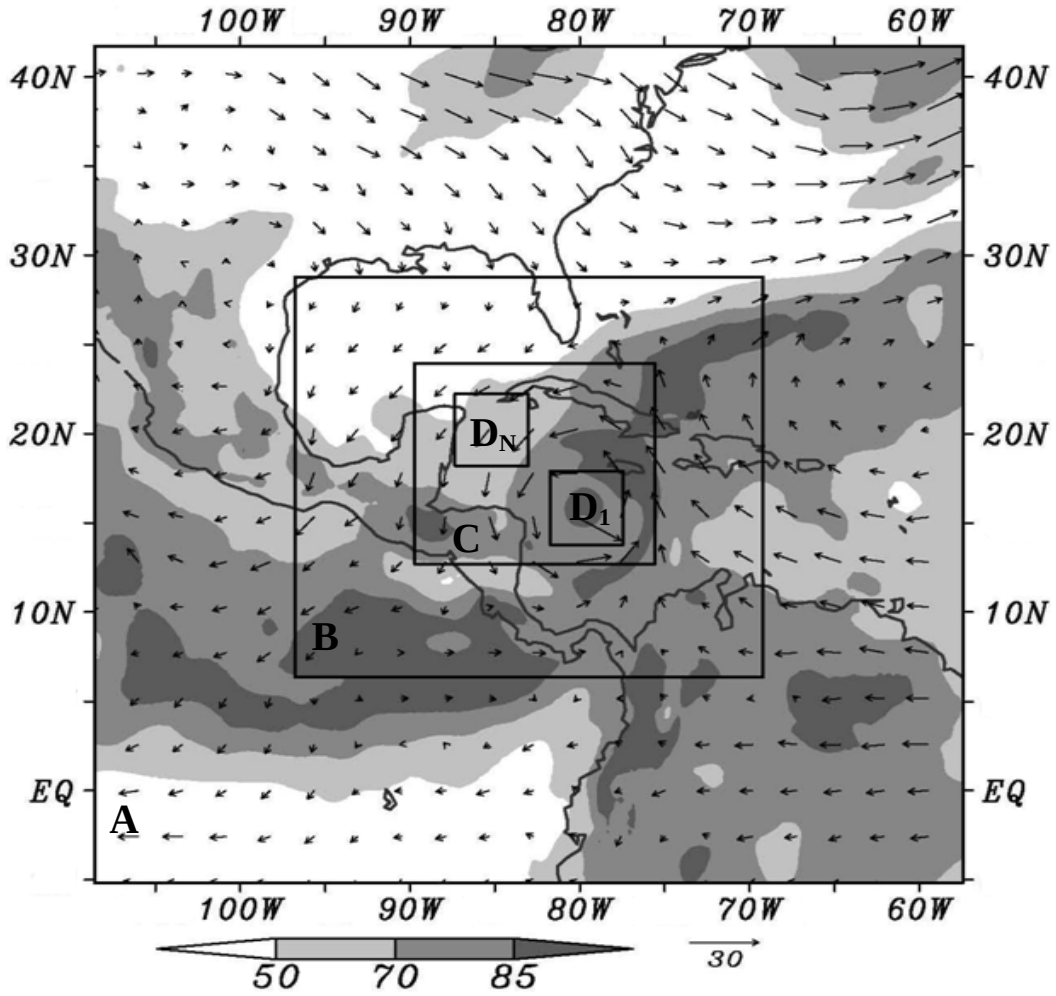


Figure 2.2: Model domain configurations, superimposed with surface wind vectors and 600 – 900 hPa layer-averaged relative humidity (shaded) at 0000 UTC 18 October 2005. Domains A, B, C, and D have the horizontal resolution of 27, 9, 3, and 1 km, respectively. Domain D is designed to follow the movement of the storm with $D_1$ and $D_N$ denoting its respective initial and final positions.

Figure 2.2 shows the quadruply nested WRF domains with Mercator's map projection. Three stationary outer domains—A, B, and C—have (x, y) dimensions of 200 × 200, 322 × 277, and 496 × 415 grid points with grid spacings of 27, 9, and 3 km, respectively, while a moving innermost domain D with (x, y) dimensions of 451 × 451 and 1-km grid length is used to follow the center of Wilma at 6-min intervals.

All of the four domains are activated at the same time: 0000 UTC 18 October. Note that the outermost domain, A, given in Figs. 2.1 and 2.2, is the largest domain size, with a Mercator map projection one can obtain from the GFDL data. It covers most of the Mexican high, the western portion of the Atlantic high, the ITCZ to the south, and a midlatitude trough to the north (Fig. 2.1). All of the domains use 55 σ—levels in the vertical, which are given by The 55 σ–levels are given as follows: 1, 0.997, 0.993998, 0.990703, 0.987069, 0.983042, 0.978562, 0.973559, 0.967947, 0.961631, 0.954496, 0.946408, 0.937207, 0.926704, 0.914673, 0.900841, 0.884878, 0.866379, 0.844843, 0.81964, 0.79164, 0.76114, 0.72904, 0.69584, 0.66224, 0.62844, 0.59464, 0.56084, 0.52704, 0.49324, 0.45944, 0.42564, 0.39184, 0.35804, 0.32424, 0.29064, 0.25744, 0.22534, 0.194840, 0.16684, 0.141638, 0.120102, 0.101603, 0.08564, 0.071808, 0.059777, 0.049274, 0.040073, 0.031985, 0.02485, 0.018534, 0.012922, 0.007918, 0.003439, 0. The model top is set at 30 hPa.

The model physics options used include (i) the Thompson et al. (2004) cloud microphysics scheme, which contains six classes of water substance (i.e., water vapor, cloud water, rain, snow, graupel, and cloud ice); (ii) the Yonsei University PBL parameterization with the Monin–Obukhov surface layer scheme (Hong et al. 2006); (iii) the Rapid Radiative Transfer Model (RRTM) for long waves with six molecular species(Mlawer et al. 1997) and the Dudhia (1989) shortwave radiation scheme; and (iv) the Betts–Miller–Janjic (Betts 1986; Betts and Miller 1986; Janjic´ 1994) cumulus parameterization scheme only for the outermost domain.

We found in our initial experimentation that the following model options are important for the reasonable prediction of the record-breaking intensity and RI rates

of Wilma as well as the associated inner-core structures: (i) the finest 1-km horizontal resolution; (ii) the high (55 level) vertical resolution, especially in both the lower and upper tropospheres; and (iii) a cloud-permitting microphysics scheme.

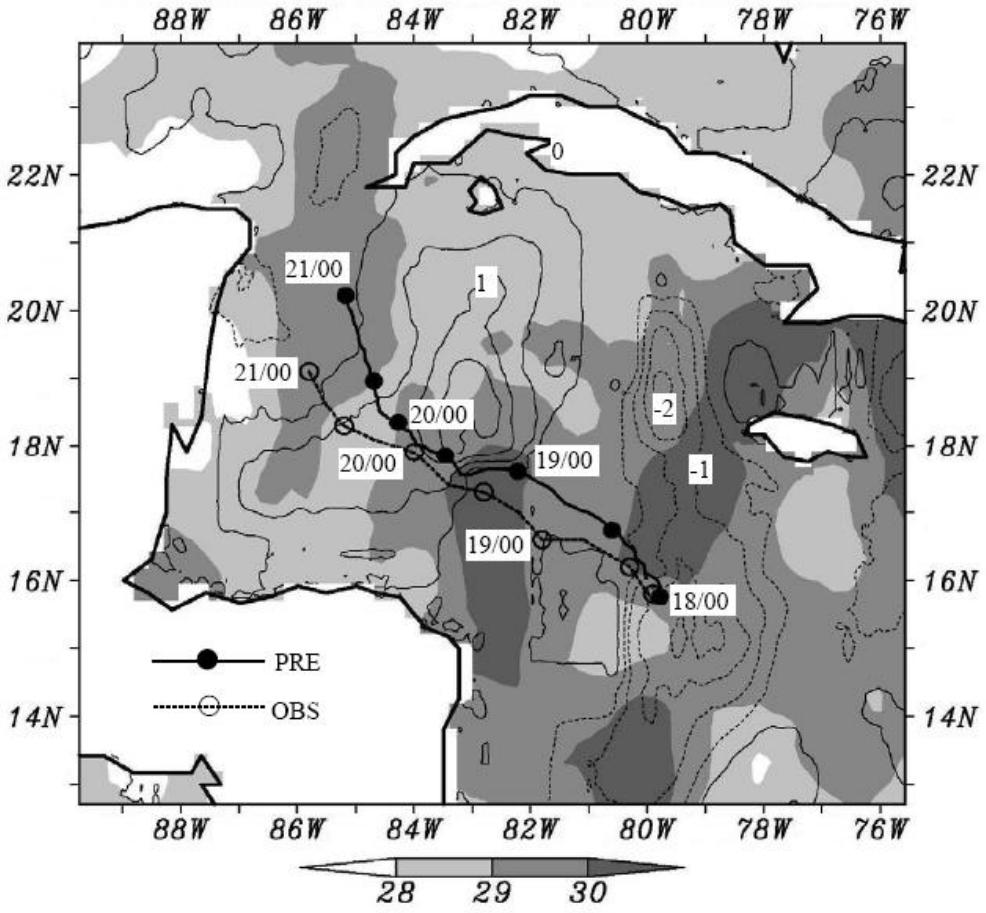


Figure 2.3: Comparison of the model-predicted (PRE, thick solid) track of Wilma to the observed track (OBS, thick dashed) over a subdomain during the 72-h period of 0000 UTC 18 – 0000 UTC 21 October 2005. Shadings shows SST at the model initial time with thin-solid (for positive values) and thin-dashed lines (for negative values) denoting the SST differences (at intervals of 0.5°C) (i.e., SST at 19/0000 minus SST at 18/0000).

### *2.4. Model verification*

In this section, we verify the 72-h prediction of Wilma against some selected observations in order to demonstrate the performance of the WRF in predicting the track, intensity, and inner-core structures of the storm using the then-operational data. For this purpose, we compare first the model-predicted track of Wilma to the best-track analysis (see Fig. 2.3). It is evident that the WRF reproduces the general northwestward movement, which is determined by the large-scale flows associated with the Atlantic high. However, the predicated storm tends to move too fast to the right of the observed during the initial 24 h, causing a final position error of about 120 km that is too far to the north-northeast of the best track. The initial fast movement appears to be attributable to the GFDL bogusing scheme in which a vortex circulation with a radius of greater than 500 km was readjusted (not shown), based on the procedures described by Kurihara et al. (1993). Thus, the mesoscale flow field was somewhat altered. In addition, we find that the model underpredicts the Mexican high to the west of the storm. This implies the generation of weaker northerly flows that accounts partly for the north-northeastward bias of the predicated track.

The time series of the predicted hurricane intensity in terms of $P_{MIN}$ and $V_{MAX}$ are compared to the observed in Fig. 2.4, showing that despite some differences in the detailed intensity changes the model predicts reasonably well the initial rapid spinup, followed by a period of 18–21-h RI and a subsequent weakening stage, with the final intensity (i.e., at 72 h into the integration, valid at 0000 UTC 21 October, hereafter 21/00-72) that is almost identical to the observed. Although the WRF starts the RI stage 3 h earlier, the predicted strongest intensities are 889 hPa and 72 m $s^{-1}$, which

are 7 hPa and 10 m $s^{-1}$ weaker than the observed $P_{MIN}$ and $V_{MAX}$, respectively. This yields a mean predicted RI rate of 4 hPa $h^{-1}$ (and 1.6 m $s^{-1}$ $h^{-1}$), as compared to the observed mean RI rate of 5.2 hPa $h^{-1}$ (and 2.4 m $s^{-1}$ $h^{-1}$) during the period of 18/18-18 to19/12-36; the peak hourly RI rates from the model prediction and best track are 7 and 9 hPa $h^{-1}$ near 19/06-30, respectively. As will be shown later,

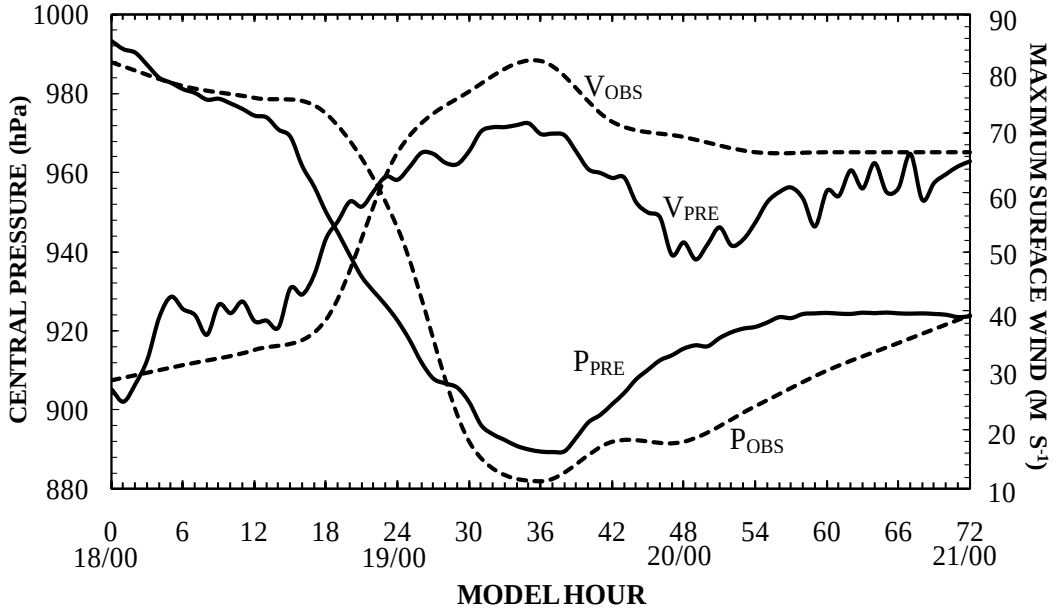


Figure 2.4: Time series of model-predicted (PRE, solid) and the observed (OBS, dashed) maximum surface wind ($V_{MAX}$, m $s^{-1}$) and minimum sea-level pressure ($P_{MIN}$, hPa) for during the period of 18/00-00 to 21/00-72.

weaker-than-observed storm appears to be caused by a temporal halt of RI between 19/03-27 and 19/05-29, which results from a seemingly fictitious eyewall-merging scenario, and the underpredicted $V_{MAX}$ could be attributed partly to a relatively larger storm size than is observed. Note, however, that Wilma's intensity at 1200 UTC 19 October was extrapolated in time from the dropwindsonde-observed $P_{MIN}$ of 892 hPa

and flight-level estimated $V_{MAX}$ of 75 m $s^{-1}$ near 0800 UTC, based on the observation that the storm's central pressure was still falling at this flight time (Pasch et al. 2006).

One may note that the predicted $V_{MAX}$ increases from 52 m $s^{-1}$ at 20/00-48 to 61 m $s^{-1}$ at 20/09-57, while the best track exhibits slow weakening of the storm after reaching its peak intensity. This scenario occurs during the period $V_{MAX}$ at the outer RMW begins to exceed that at the inner RMW, and its subsequent increase results from the contraction of the outer eyewall. Clearly, the two RMWs could not be resolved from dropwindsonde observations over Wilma's inner-core region. One may also note that the predicted $P_{MIN}$ increases at a rate larger than that in the best track after 19/18-42. We attribute this more rapid weakening partly to the time-independent SST used that is about 1 –1.5 ºC colder than the observed to the right of the storm track (i.e., north of 17.5ºN; see Fig. 2.3). In other words, the observed slow weakening of Hurricane Wilma (2005) during its ERC might be related to its movement over the warm-ring region.

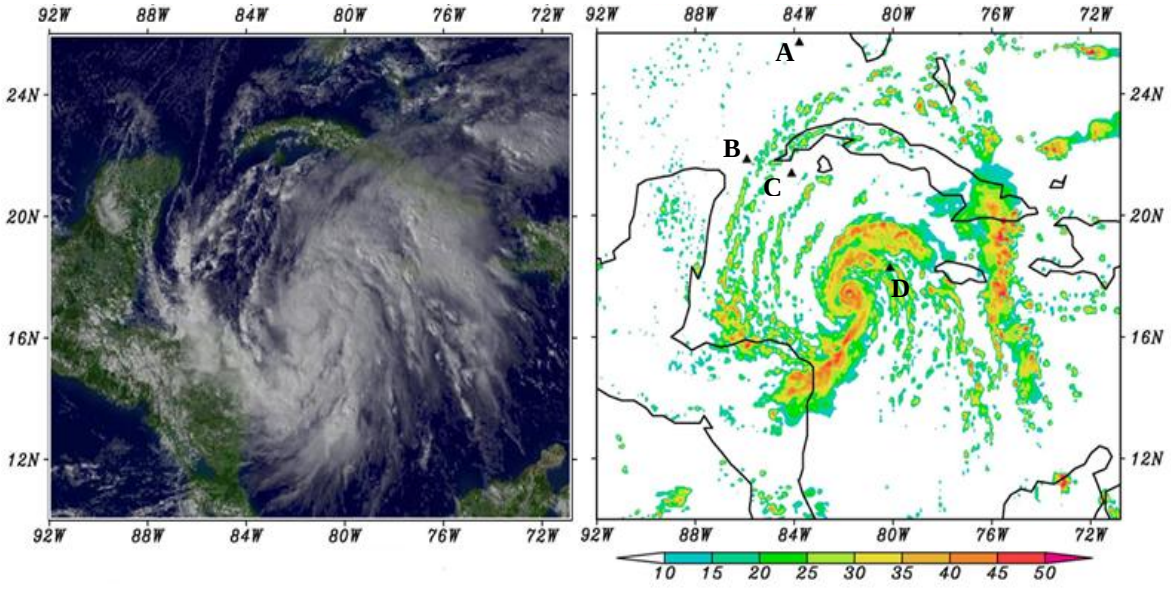

Figure 2.5: (a) Visible satellite imagery at 1900 UTC 18 October; and (b) model-predicted radar reflectivity at z = 1 km from the 18-h simulation, valid at 1800 UTC 18 October. Letters, “A”, “B”, “C”, and “D”, denote the locations of the soundings shown in Fig. 2.6.

Figures 2.5a and 2.5b compare the predicted radar reflectivity to a satellite visible image at 1900 UTC 18 October, when the storms just begin their RI stages. Although the two maps show different cloud microphysics variables (i.e., clouds versus precipitation), we can still see that the model reproduces two spiral rainbands to the immediate northeast of the storm, an extensive rainband that wraps around the eyewall starting from the Bahamas, and some scattered convective systems over southern Mexico. It is evident from Fig. 2.5b that Wilma has spun up to an intense hurricane with a small-sized eyewall, as indicated by a pinhole, which is surrounded by several spiral rainbands within a radius of over 600 km. The inner rainbands will be wrapped around to form an outer eyewall during the next 18 h.

Since the larger-scale flows play an important role in determining the track and intensity as well as the inner core structures of a hurricane, it is desirable to examine how well the model can reproduce the right prestorm environmental conditions. So, Fig. 2.6 compares four selected soundings near the onset of RI. They are all taken in the northwest quadrant of the storm (see Fig. 2.5b for their locations) where the dry air, which appears to affect the distribution of the spiral rainbands and the intensity of Wilma, is likely to have originated, based on satellite imagery (Fig. 2.5a) and the GFS analysis (see Fig. 2.2). Two soundings (i.e., A and B) are situated in the vicinity of the outer rainbands, and the other two are located close to the inner-core region (Fig. 2.5b). Indeed, both the observed and predicted soundings at site A

show the presence of an intense inversion layer between 850 and 900 hPa, with a deep dry layer above, due to the influence of the Mexican high. Note the development of a well-mixed, moist PBL in the lowest 100 hPa that represents an important

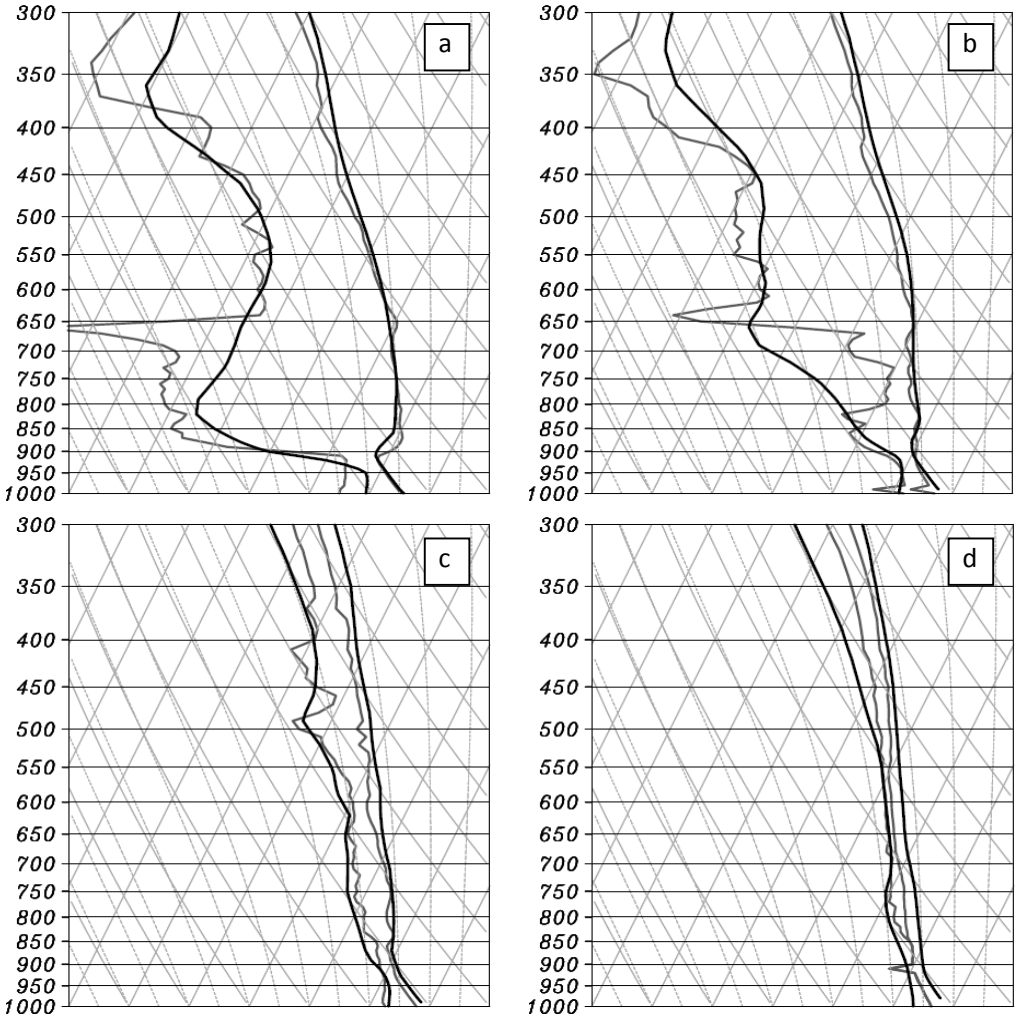


Figure 2.6: Comparison of Skew-T/Log P diagrams of soundings taken at points (a) A; (b) B; (c) C, and (d) D, as given in Fig. 5b, between the model prediction (dark black) and the observation (grey) near 1800 UTC 18 October.

moisture reservoir for storm development over the Gulf of Mexico (where Wilma will move into during the next few days). Comparing to site A, the influence of the Mexican high is much reduced toward site B, as indicated by a much weaker

inversion layer and possibly less subsidence-induced drying in the lower troposphere. The observed sounding shows a very moist area in the 800–700-hPa layer, suggesting that the dropwindsonde might have gone through a cloud layer in the outer region (see Fig. 5b).

In contrast, the two soundings taken close to the inner core regions exhibit moist columns with a near-moistadiabatic lapse rate up to 300 hPa. This is especially notable at site D, which is located near a major rainband to the north of the storm. Such moist vertical columns are present at most sites in the southern semicircle (not shown), which are closely related to the ITCZ (Fig. 2.2). Thus, Wilma developed in a rather moist environment with high SST, except for that over the Gulf of Mexico region. The WRF reproduces reasonably well these environmental conditions, as shown in Figs. 2.5 and 2.6.

After verifying the model-predicted larger-scale conditions, we next examine to what extent WRF could reproduce the observed inner core structures of Wilma. Because observed radar reflectivity maps are not available, we use the 85-GHz satellite images to validate the model-predicted reflectivity near the peak intensity time and at a later weakening stage (see Fig. 7). As we know, cirrus canopies covering TSs in visible and infrared images are transparent at 85 GHz, so these images may be treated as ‘‘the poor man’s radar’’ for the distribution of deep convection. However, such satellite images are of too-coarse resolution to resolve Wilma’s small pinhole eye (i.e., less than 5 km in diameter), and only a small area of intense convection near the center of two large spiral rainbands (A and B) could be seen, presumably as Wilma’s inner eyewall (Fig. 7a). Of importance is that the two

spiral rainbands are about to be merged to form an outer eyewall, with a wide moat annulus between the two eyewalls at this time. This coincides with the immediate weakening of Wilma after reaching its maximum intensity (cf. Figs. 7a and 4). Another rainband (C), extending from A outward and northeastward, persists throughout the 72-h period. This type of rainband is labeled by Willoughby et al. (1984) as the principal rainband serving as the interface between the inner-core region and the prestorm environment.

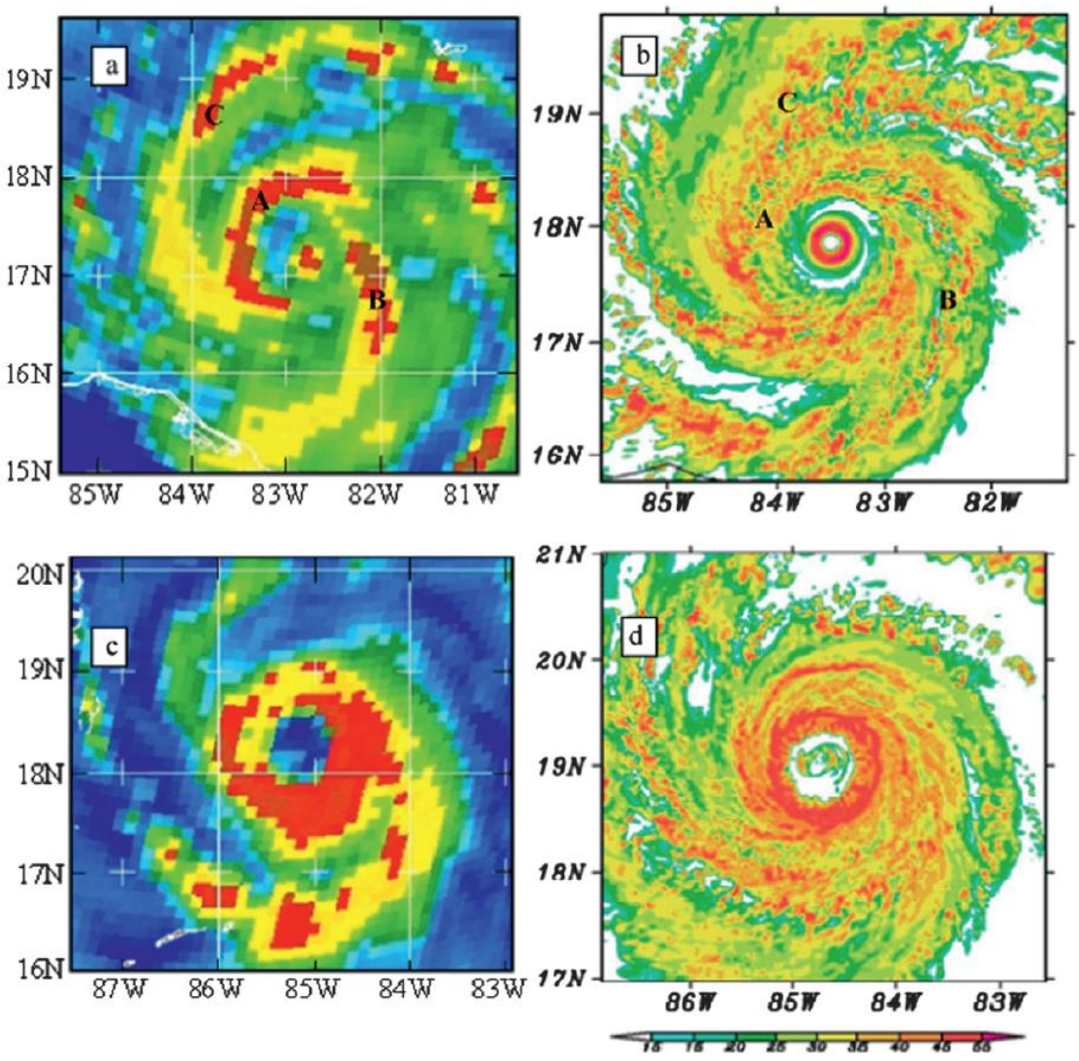


Figure 2.7: (a) SSM/I 85 GHz satellite image at 1214 UTC 19 October; (b) predicted radar reflectivity over an area of 400 km × 400 km at z = 1 km from the 36.25-

h forecast (valid at 1215 UTC 19 October); (c) and (d) as in (a) and (b), except at 1235 UTC 20 October, respectively.

A comparison of Figs. 7a and 7b indicates that WRF reproduces the axisymmetric inner eyewall, surrounded by three rainbands, although the predicted inner eyewall size is larger than the observed and the outer eyewall has formed from rainbands A and B. The model reproduces the wide coverage of banded convective rainfall in the southern and northern quadrants. Of importance is that the model captures the timing of the outer eyewall formation, which coincides with the weakening of Wilma after reaching its peak intensity. A detailed analysis of the model-predicted radar reflectivity reveals that rainbands B and C form in the inner-core region. As they propagate cyclonically outward, convective cells tend to diminish in their tails because of dry-air intrusion, but are replenished by those outward-propagating cells. Various hypotheses for the propagation of the spiral rainbands and the formation of the outer eyewall have been proposed, such as internal gravity waves (Yamamoto 1963; Kurihara 1976; Elsberry et al. 1987), vortex Rossby waves (MacDonald 1968; Guinn and Schubert 1993; Montgomery and Kallenbach 1997), and recently the mixed vortex-Rossby–inertia/gravity waves (Zhong et al. 2009). These hypotheses will be examined in a future study using the high-resolution model data.

Figures 7c and 7d compare the rainfall structures near 1235 UTC 20 October, which is close to the end of the ERC, as indicated by an eye size of more than 60 km in diameter. The eyewall, newly formed from the closure of the parts of rainbands A and B, was significantly larger in radius and width than the earlier example (cf. Figs.

7c,d and 7a,b). Spiral rainbands were still extended in the northern and southern quadrants during the RI period, except for their varying intensities. That is, the northern (southern) rainband has weakened (intensified), due likely to the dry (moist) environment in which it was embedded. In general, the model captures the ERC, the more (less) extensive convective rainfall to the south (north), as well as the size and shape of the newly formed eyewall (cf. Figs. 7c and 7d). Note that the satellite data could not resolve the remnants of the inner eyewall as modeled, and appear to have aliased the wide annulus of deep convection outside the outer eyewall as a wide eyewall due to its contamination in sensing rainfall in the lower troposphere.

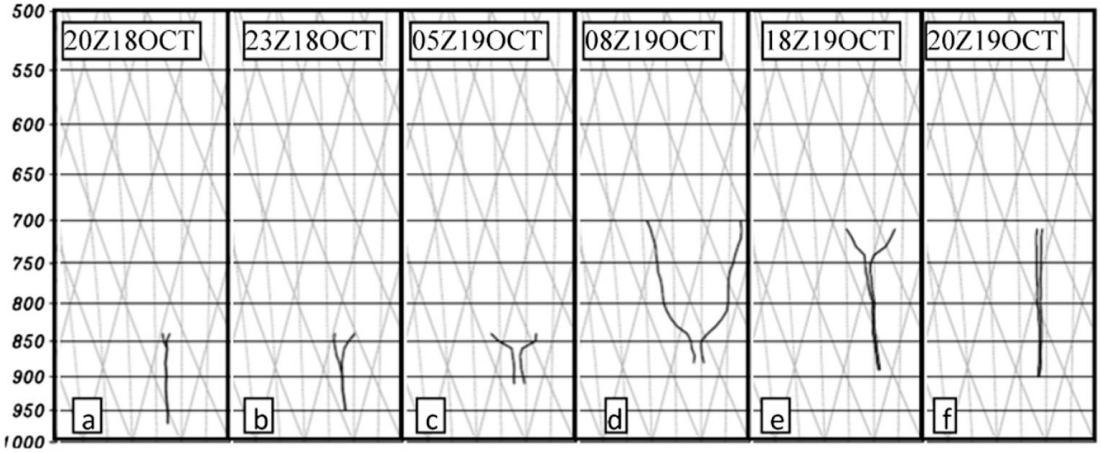


Figure 2.8: Skew-T/Log P diagrams of the soundings taken near the eye center by the US Air Force and NOAA 49 during different stages of the storm.

Figure 2.8 shows a series of dropwindsondes taken near the eye center by the reconnaissance flight at an altitude of 850 hPa initially (Figs. 2.8a–c) and later at 700 hPa (Figs. 2.8d–g). First, we see the PBL depth in the eye decreased from about 150 to 50 hPa during RI, with an intensifying inversion above. According to Zhang and Kieu (2006) the PBL depth in the eye is determined by upward sensible and latent heat fluxes, Ekman pumping, and the compensating subsidence above. In the present

case, its upward growth appears to be suppressed by an increase in the subsidence warming and drying from above that was indicative of the RI. This subsidence appears to account for the transformation of an initial saturated to an unsaturated PBL at the later stage of RI (e.g., at 0500 UTC 19 October), with a shallow (~10 hPa) but intense inversion layer below 850 hPa (Fig. 2.8c). This inversion layer was thickened to about 40 hPa just 3 h later (i.e., 0800 UTC 19 October; see Fig. 2.8d), namely, shortly after entering a relatively slower RI stage (see Fig. 2.4). Subsequently, as the storm weakened, the eye PBL grew rapidly from an estimated depth of less than 50 hPa at 0800 UTC 19 October to about 150 hPa at 1800 UTC 19 October (cf. Figs. 2.8d and 2.8e) as a result of Ekman pumping overpowering the subsidence drying/warming. Willoughby (1998) has documented a similar scenario in Hurricane Olivia (1994) in which the base of the inversion layer was elevated from 830 to 740 hPa as its $P_{MIN}$ rose from 930 to 937 hPa in 2.7 h.

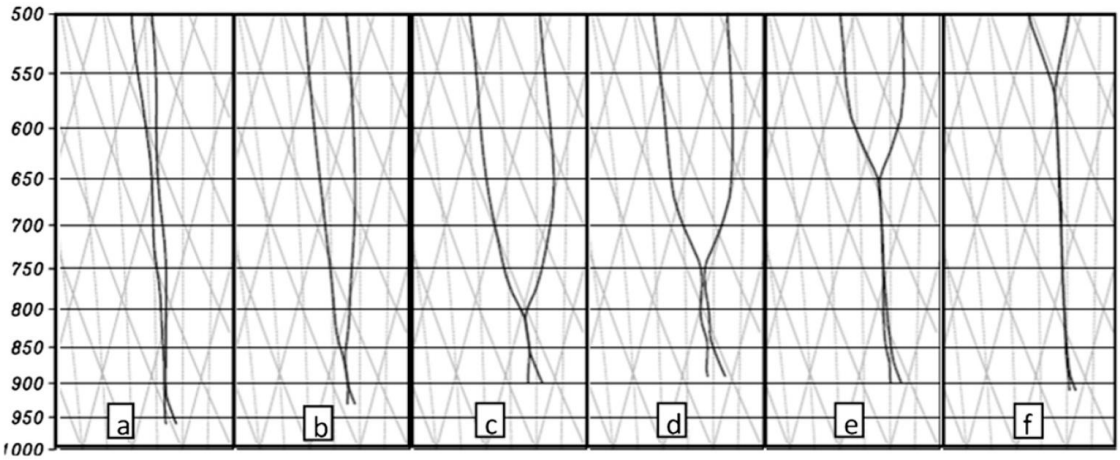


Figure 2.9: As in Fig. 8, except from the model prediction.

It is apparent by comparing Figs. 2.8 and 2.9 that the model-predicted eye soundings compare favorably to the observed up to 18/23–23. Of interest is that the

model predicts three different layers in the eye: a well-mixed but unsaturated layer with the dry-adiabatic lapse rate in the lowest 50 hPa, a saturated layer with the moist-adiabatic lapse rate (but little condensation occurring) above, and a dry and warm air layer with a thermal inversion aloft (Fig. 2.9). Willoughby (1998) has shown the existence of such a shallow, well-mixed PBL in Hurricane Olivia (1994), although it is not evident in the observed soundings given in Fig. 8. Of primary concern is that the model appears to overpredict the growth of the saturated layer and underpredict the inversion intensity above, especially during the RI period (cf. Figs. 2.9c,d and 2.8c,d). This indicates that the predicted dry subsidence warming and drying in the eye may be too weak to compensate for the upward transport of sensible and moisture fluxes by Ekman pumping (see Zhang et al. 2002; Zhang and Kieu 2006). In addition, numerical horizontal diffusion, calculated at constant pressure surfaces, could account for a significant portion of the moistening in the layer (Zhang et al. 2002), when considering the relatively small eye being modeled. As a result, the model overpredicts the depth of the moist layer at 19/20–44 (cf. Figs. 2.8f and 2.9f).

Figure 2.10a shows the radial profiles of tangential winds observed at the flight level. At 2130 UTC 18 October, when Wilma was in its early RI stage, we see a maximum wind of 40 m $s^{-1}$ located at r = 20 km, with a relatively flat radial profile beyond r = 50 km. In the next available flight-level profile (i.e., by 1800 UTC 19 October), the maximum wind speed had doubled and the RMW had contracted to about 8 km, with a much sharper radial profile than that 20 h earlier. Note that another local wind maximum developed near r = 60 km, which was indicative of the development of the outer eyewall. Subsequently, this outer RMW was contracting

while the associated peak wind continued to increase. Meanwhile, the inner wind maximum weakened from 80 to 70 m $s^{-1}$ during the period of 1800 UTC 19 October–2140 UTC 19 October. The inner and outer wind maxima reached a comparable

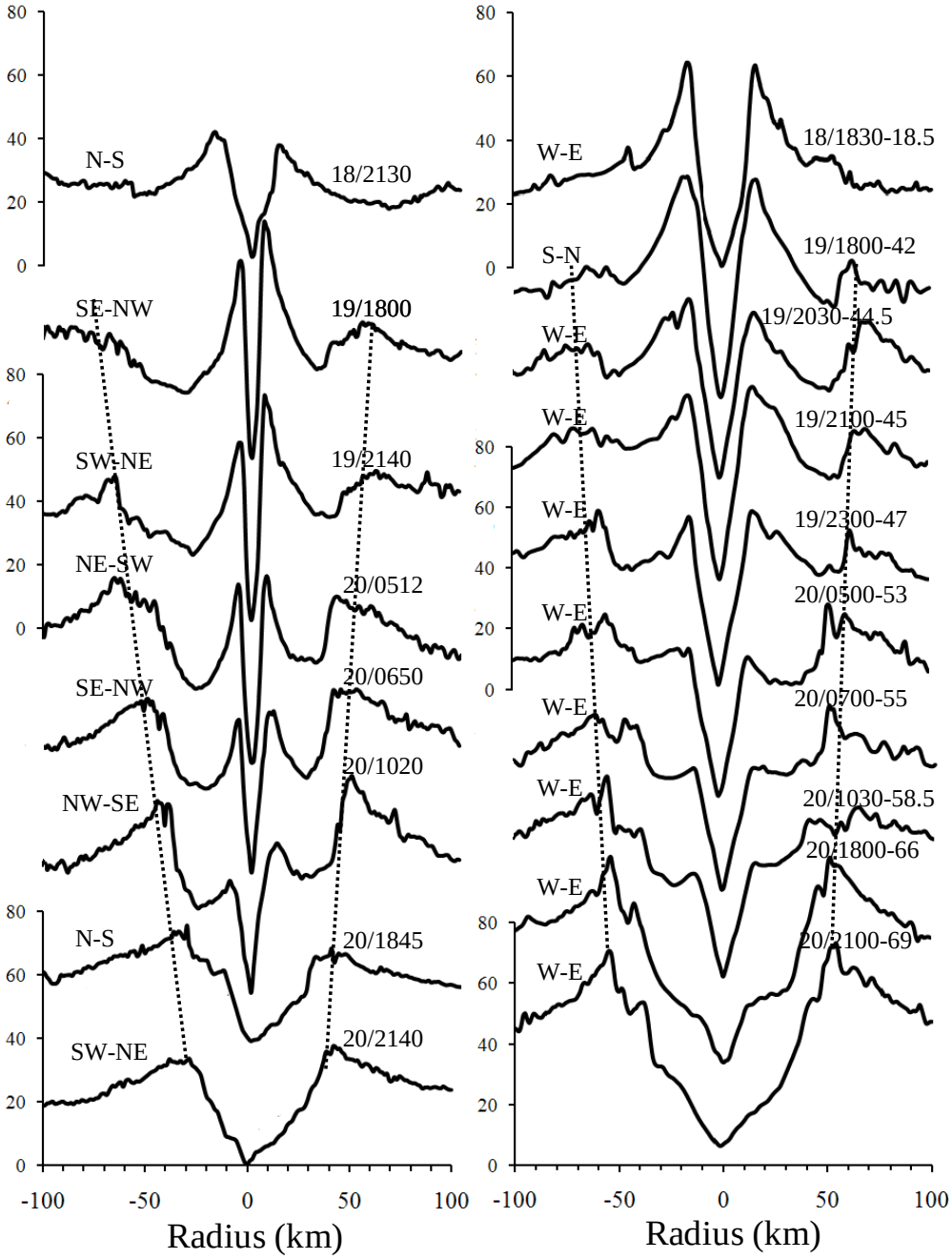

Figure 2.10: Comparison of radial profiles of flight-level tangential winds spanning a diameter of 200 km within Wilma. (a) Observations, and (b) model prediction. Dashed lines indicate the evolution of the RMW.

strength at 0500 UTC 20 October, with the deepest saddle wind profile and the most pronounced moat area between. Because the contracting outer eyewall choked off the inward energy supply, the inner eyewall dissipated with time. As a result, the inner eyewall/wind maximum disappeared by 2140 UTC 20 October, with the previous pinhole eye and RMW of 8 km replaced by a large eye with an RMW of about 35 km. The increased RMW implies that the efficiency of diabatic heating in intensifying the storm was significantly reduced after the ERC, according to Hack and Schubert (1986).

It is evident that the model predicts reasonably well the formation of an outer RMW/eyewall near the end of RI, the subsequent dissipation (growth) of the inner (outer) eyewall, and the 18–24-h duration of the ERC (cf. Figs. 2.10a and 2.10b). However, the inner RMW is predicted to be about twice as large as observed, with a slower-than-observed contraction rate occurring during the RI period (e.g., from 18/1830-18.5 to 19/18-42). It appears that both the larger RMW and the slower contraction could be attributed to the development of an artificial outer eyewall during the period of 19/00–24 to 19/06–30 (see Fig. 2.11). Similarly, the predicted outer eyewall also contracts more slowly than does the observed, although the model reproduces reasonably well the outer RMW size near the end of RI. We may attribute this to the above-mentioned too large inner eyewall predicted, with less-than-observed radial gradients in tangential wind outward from the inner RMW. As pointed out by Willoughby (1988), the contraction rate is determined by the ratio of

the tangential wind increase to its radial gradient evaluated on the inward side of the RMW. In other words, the predicted radial wind profile tends to transport less absolute angular momentum inward than the observed for the amplification of rotation at the outer RMW, causing relatively weaker rotational winds in the outer region.

In summary, the model predicts reasonably well the track and intensity of Hurricane Wilma (2005), including its RI, the eye's thermal structures, double eyewalls, and the moat area between as well as the ERC. In spite of some discrepancies in the detailed structures, the general agreement between the model prediction and the observations will allow us to use the model results in the next section to examine various inner-core structures associated with the RI and intensity changes of Wilma.

### *2.5. Model-predicted structural changes*

It has been recently realized that the RI and intensity changes are often associated with the rapid eyewall contraction, the ERC, and some inner-core structural changes (e.g.,Willoughby et al. 1982; Zhu et al. 2004; Lee and Bell 2007; Rogers 2010). For this purpose, Fig. 2.11 shows the radius–time cross section of tangential winds and radar reflectivity (at z = 3 km) during the 72-h integration period. At the model initial time, deep convection is highly asymmetrically distributed in Wilma's eyewall due to the presence of moderate VWS (not shown), and the hurricane vortex has an RMW of about 70–80 km. The RMW decreases rapidly to 30 km during the initial 12-h rapid spinup (cf. Figs. 2.11 and 2.4). Such a rapid decrease in RMW has also been observed in the other RI storms, for example,

Elena of 1985 (see Corbosiero et al. 2005) and Gabrielle of 2001 (Molinari and Vollaro 2010). This rapid contraction may result from the development of convective bursts, which has been the subject of numerous observational and model studies (e.g., Heymsfield et al. 2001; Kelley et al. 2004; Squires and Businger 2008; Reasor et al. 2009; Guimond et al. 2010; Rogers 2010).

The model-predicted radar reflectivity shows the closure of the eyewall near 18/15-15, coinciding with the onset of Wilma's RI, although the convective asymmetry is still evident, with an irregular eyewall (see Fig. 2.12a). The RMW and eyewall continue to contract and become more axisymmetric and robust, reaching the smallest RMW of 12 km (at z = 1 km) at 19/03-27, which is consistent with the continuous RI (cf. Figs. 2.4 and 2.12e). Meanwhile, three to four spiral rainbands within a radial interval of 20–30 km begin to merge and form a secondary eyewall at 18/21-21 (Fig. 2.12c), and this eyewall contracts at a rate much faster than the inner eyewall shortly after. Because of the different contracting rates, the two eyewalls merge between 19/03-27 and 19/5-29 and form a wide eyewall, shifting both the updraft core and RMW slightly outward (cf. Figs. 2.12e,f and 2.11). As a result, Wilma's RI is temporally halted during this 2-h period (see Fig. 2.4). Note that the inner eyewall exhibits little evidence of dissipation while the secondary eyewall contracts (cf. Figs. 11 and 12c–e). In this regard, the merging process differs from the ERC. Although this merging scenario is not supported by the observed intensity changes in Wilma, it may appear in other hurricanes when an outer eyewall is formed close to an inner eyewall (i.e., with a narrow moat area). In the present case, we attribute the merged eyewall to the use of Thompson et al.'s (2004) cloud

microphysics scheme, because it is absent when the other microphysics schemes are used.

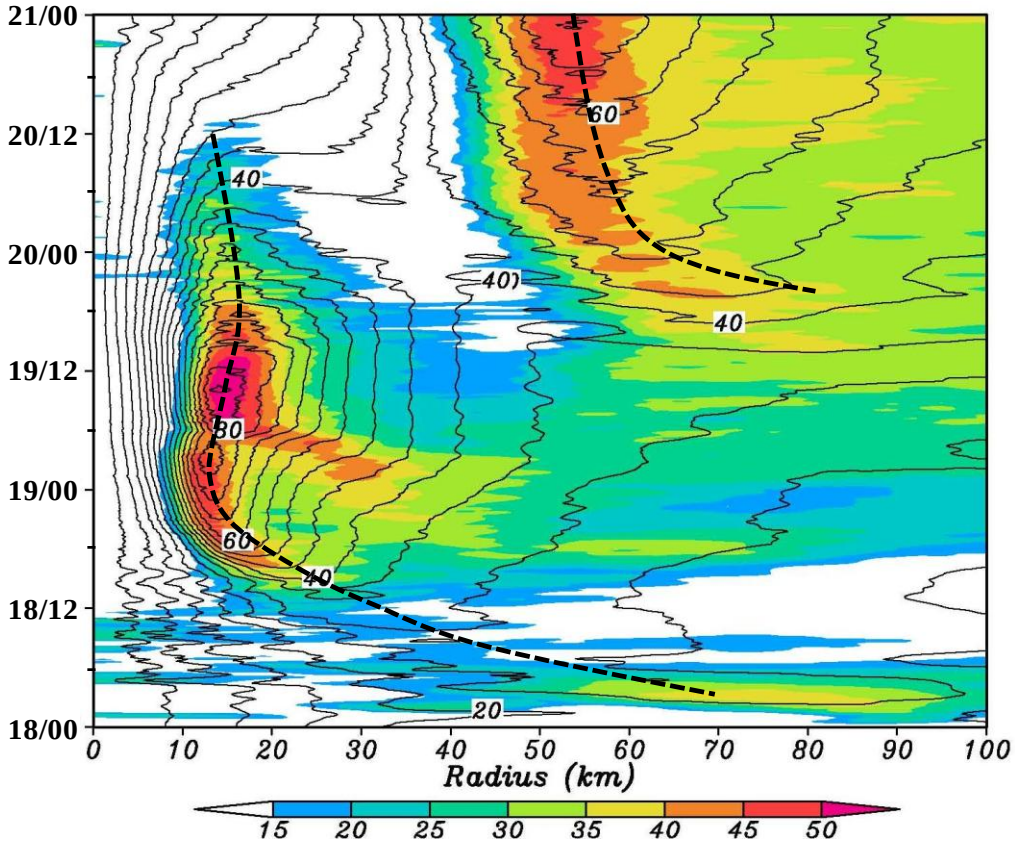


Figure 2.11: Tangential winds as a function of time and radial distance (every 5 m s-1), superimposed with the radar reflectivity (dBZ), at z = 3 km from the 72-h model integration between 18/00-00 and 21/00-72. Dashed lines denote the RMW.

The modeled storm resumes its RI after 19/05-29 with the peak RI rate of about 7 hPa $h^{-1}$ from 19/06-30 to 19/07-31, and reaches its peak intensity near 19/12-36 as observed (Fig. 2.4). However, the RMW and eyewall do not contract during the final 6-h RI stage (Fig. 2.11). The storm begins to weaken as another eyewall forms near the radius of 65 km and the inner eyewall dissipates (Fig. 13). This scenario fits well the typical ERC as described in section 1. Of significance is that unlike those

short-lived [e.g.,Andrew of 1992 (Liu et al. 1997); Bonnie of 1998 (Rogers et al. 2003; Zhu et al. 2004)], this ERC lasts for as long as 24 h from both the model and

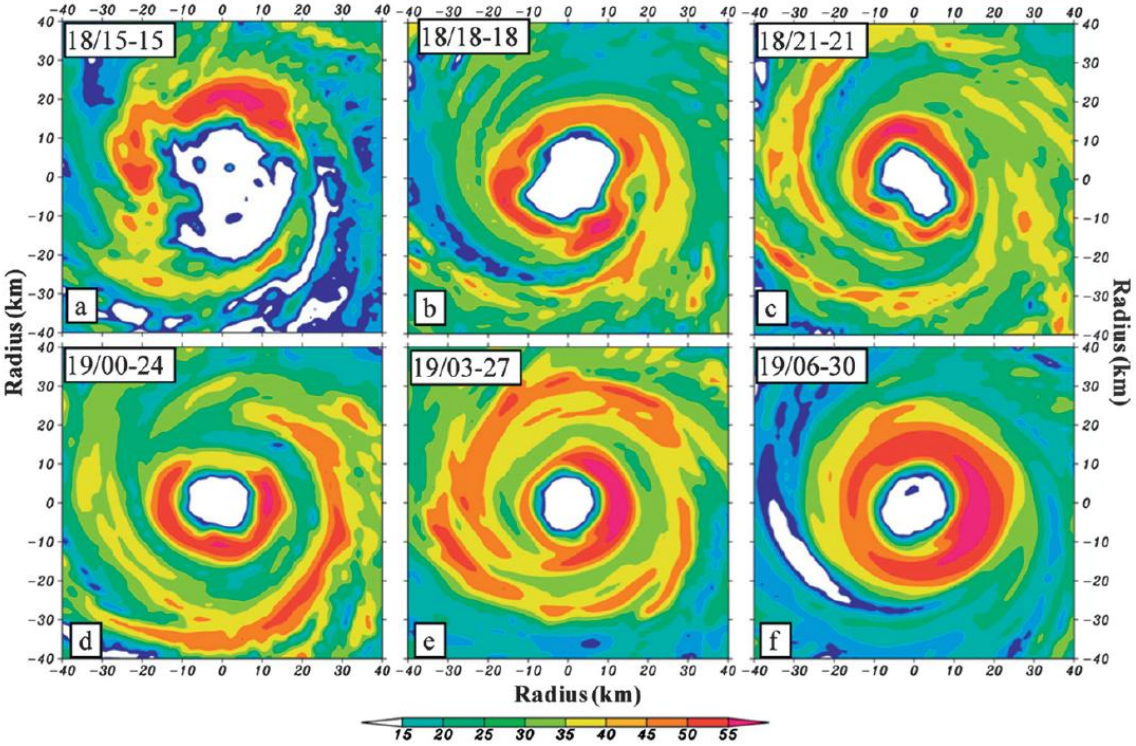


Figure 2.12: Predicted radar reflectivity (dBZ) at 3 hourly intervals at z = 1 km over a subdomain of 80 km × 80 km from the 15 to 30 h model integration between 18/15-15 and 19/06-30.

observations (see Figs. 2.13 and 2.10). Such a long ERC could be attributed to the development of the large outer RMW with a wide moat area between the inner and outer eyewalls (see Figs. 2.13 and 2.14). Specifically, based on the balanced dynamics of Kieu and Zhang (2010), the outer eyewall tends to generate inside itself a deep layer of anticyclonic flow to offset the cyclonic rotation of the inner eyewall. It also generates an outward convergent flow in the PBL to block the energy supply to deep convection in the inner eyewall, and subsidence between the two eyewalls to suppress convective development in the inner eyewall. Because of the inertial

stability of the inner vortex, these negative effects tend to occur closer to the outer eyewall, as can be seen from the buildup of large radial gradients of the tangential winds near the outer RMW (see Figs. 2.10 and 2.11). It appears that warm SST over the region also helps maintain deep convection in the inner eyewall, as indicated by small decreases in equivalent potential temperature ($\theta_e$) in the eye PBL (see Fig. 2.14). Clearly, the greater the moat area, the longer is the ERC.

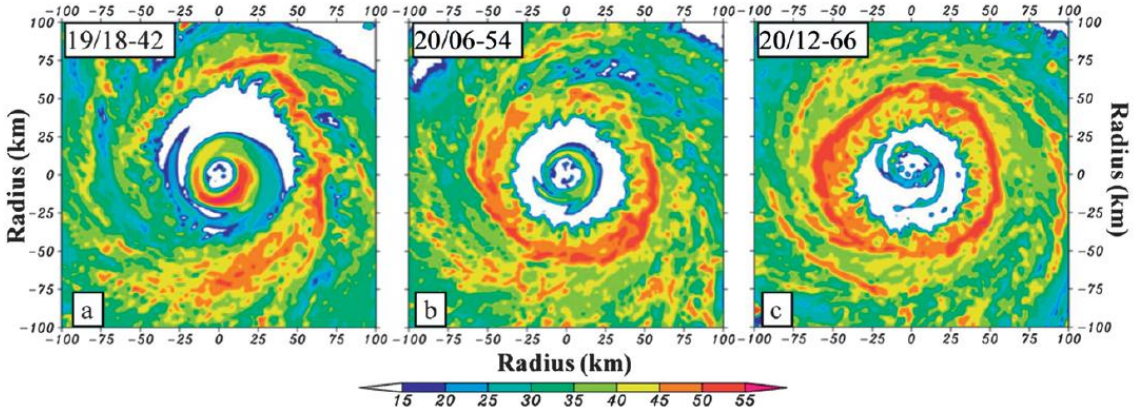


Figure 2.13: Predicted radar reflectivity (dBZ) at z = 1 km in a subdomain of 200 km × 200 km at (a)19/18-42; (b) 20/06-54; and (c) 20/18-66.

Figure 2.14 also shows the vertical cross-sectional evolution of the ERC in terms of $\theta_e$ and vertical circulations. During the early ERC stage, we see strong radial gradients of $\theta_e$ in the inner eyewall with a $\theta_e$ minimum in the eye and another one between the inner and outer eyewalls (Fig. 2.14a). The latter one is consistent with the presence of the minimum $\theta_e$ at z = 3 km in the environment, and is clearly isolated by deep convection transporting high- $\theta_e$ air upward in the outer eyewall. By 20/06-54, the inner eyewall has weakened substantially, with decreasing $\theta_e$ gradients, while the outer eyewall has fully developed, with a well-defined cloud-free moat area between (Fig. 14b). Some evaporatively driven moist downdrafts can be seen,

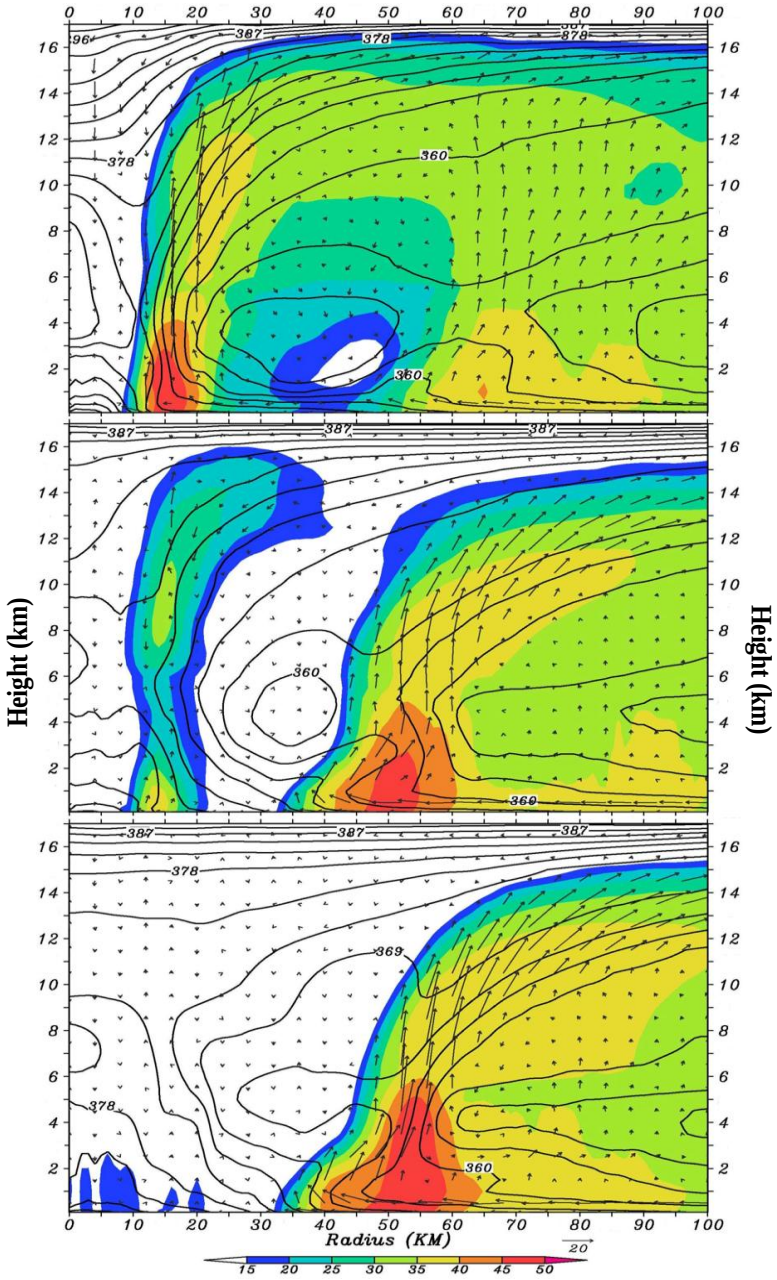


Figure 2.14: Azimuthally averaged equivalent potential temperature ($\theta_e$) as a function of radius and height at intervals of 3 K and radar reflectivity (dBZ, shaded), superimposed with in-plane flow vectors, at (a) 19/18-42; (b) 20/06-54; and (c) 20/18-66.

initially at the outer edge of the inner eyewall, as it is surrounded by dry subsidence. These moist downdrafts must play an important role in speeding up the collapse of

the inner eyewall. Near the end of the ERC, a large-sized eye is developed with little evidence of clouds associated with the inner eyewall. However, the $\theta_e$ structures still exhibit the footprint of the inner eyewall, even long after the complete dissipation of the inner eyewall convection. Higher- $\theta_e$ air may be expected in the eye resulting from a mixture of the air masses in the original eye, inner eyewall, and moat area. Thus, the ERC can alter significantly the thermodynamical properties in the inner-core region of a hurricane.

### *2.6. Chapter summary*

In this study, we present a 72-h numerical prediction of the record-breaking development of Hurricane Wilma (2005) using a two-way interactive, movable, multinested grid (27/9/3/1 km), cloud-permitting version of the WRF ARW using the initial and boundary conditions that would be available in an operational setting. It is demonstrated that the WRF reproduces reasonably well the track, initial rapid spinup, RI, peak intensity, and subsequent weakening of the storm, as verified against various observations. In particular, the model captures the timing of the occurrence of RI, the peak intensity, and subsequent weakening of Wilma. Specifically, the model predicts a peak intensity of 889 hPa in $P_{MIN}$ and 72 m $s^{-1}$ in $V_{MAX}$, and a mean deepening rate of more than 4 hPa $h^{-1}$ during an 18-h RI period, as compared to the observed 882 hPa and 82 m $s^{-1}$, and 5.2 hPa $h^{-1}$ mean RI rates. The model also predicts the peak deepening rate of 7–8 hPa $h^{-1}$, albeit for about 1 h, near the end of Wilma's final RI stage. However, the onset of RI is predicted 2–3 h earlier than the observed and the model-predicted track is about 120 km too far to the north-northeast of the best track at the end of the 72-h prediction.

Of particular importance is that the model reproduces the basic distribution of spiral rainbands, the timing and duration of the ERC, and the size of the outer eyewall. The model also reproduces reasonably well the suppression of PBL development in the eye with an intense warming and drying above during the RI period, and the rapid growth of the eye PBL with a moist-adiabatic lapse rate during Wilma's weakening stage. In addition, the model-predicted flow fields compare favorably to the flight-level observations, except for the inner RMW, which is twice as large as observed.

It is found through a series of sensitivity simulations that the above-mentioned intensity and structural changes can be more or less predicted with the peak intensity of at least less than 900 hPa when different cloud microphysics and PBL schemes are used in the WRF. This implies that large-scale environmental conditions, including warm SST, play an important role in determining the quality of the model-predicted intensity and structural changes of the storm. Based on these results, we may state that it is possible to improve the forecasts of hurricane intensity and intensity changes, and especially RI, if the inner-core structural changes and right storm size can be reasonably predicted in an operational setting with high-resolution cloud-permitting models, realistic initial conditions, and model physical parameterizations. In the subsequent parts of this series of papers, we will use the model results to help us understand the inner core dynamics of the RI, ERC, and multiscale interactions involved in the development of Hurricane Wilma. In addition, the sensitivity simulations will be analyzed to gain insights into the relative importance of various

parameters in affecting the inner-core structures and patterns of evolution of the storm and in obtaining the reasonable prediction of the features presented herein.

# Chapter 3. Importance of convective bursts and the upper level warm core

## *3.1. Statement of the problem*

Although there have been some improvements in tropical cyclone (TC) intensity forecasts in recent years (Rappaport et al. 2009), our ability to understand and predict the rapid intensification (RI) of TCs, where RI is defined as a deepening rate of greater than 42 hPa $day^{-1}$(or 1.75 hPa $hr^{-1}$) in the minimum central pressure ($P_{MIN}$) (Holliday and Thompson 1979) or 15 m $s^{-1}$ per day in the surface maximum tangential wind ($V_{MAX}$) (Kaplan and DeMaria 2003), is very limited due to the lack of high-resolution data. Previous studies have focused mostly on the roles of environmental factors in RI, such as sea-surface temperature (SST), vertical wind shear (VWS) and relative humidity in the lower troposphere. Obviously, these factors are not much different from those favoring tropical cyclogenesis or normal TC intensification. Thus, it is highly desirable to identify the storm characteristics, particulary processes within the inner core, that distinguish periods of RI from those occurring in the more-frequently observed non-RI periods.

Gray (1998) finds that even when all favorable environmental factors are present, TCs would not intensify without outbreaks of organized deep convection. His study singles out the important roles of convective-scale process in spinning up a preexisting TC vortex from a large-scale disturbance, such as an African easterly wave or a monsoon trough. The outbreaks of deep convection have been given great attention with different terms since the work of Gentry et al. (1970), who identified them from cold brightness temperatures in satellite images and recognized their

significance in TC intensification. They were termed as "circular exhaust clouds" by Gentry et al. (1970), extreme convection by Gray (1998) and convective bursts (CBs) or "hot towers" by many other studies (e.g.,Steranka et al. 1986; Rodgers et al. 1998; Heymsfieldet al. 2001; Guimond et al. 2010). In this study, we will use the more common term, i.e., a CB, which is defined herein as a deep, intense convective system consisting of one or more updrafts of at least 15 m $s^{-1}$ in the upper troposphere (i.e., typically above z = 11 km) that are resolvable by the model-finest grid size. These individual intense updrafts, hereafter referred to as CB-elements, are not resolvable by satellite images but may be inferred from lightning data since more lightning occurs in extremely tall convective towers (Kelly et al. 2004). Observations show the development of CBs preceding RI or coinciding with the onset of RI (Rodgers et al. 1998, 2000; Price et al. 2009; Guimond et al. 2010; Fierro et al. 2011), and few occurrences of CBs when TCs reach a quasi-steady state or start weakening (Molinari et al. 1999).

Several hypotheses have been put forward on the roles of CBs in the RI of TCs. Nolan (2007) and Montgomery et al. (2006) propose that the roles of CBs are to moisten the midtroposphere such that deep convection can occur symmetrically in the eyewall, leading to the more rapid contraction of TCs. Reasor et al. (2009) find that the upper-level updrafts and reflectivity wrap around the eye into a more axisymmetric pattern as each CB intensifies and rotates into the upshear quadrants during the RI of Hurricane Guillermo (1997). Some earlier studies have documented significant subsidence warming flanking intense updrafts that penetrate into high altitudes (Velden and Smith 1983; Foley 1998; Holland et al. 1984; Rogers et al.

2002). Heymsfield et al. (2001) show the generation of an eye 6 h after some CBs overshoot into the lower stratosphere, and their results suggest that the associated compensating subsidence contributes to the formation of a warm core and the intensification of Hurricane Bonnie (1998). By analyzing an episode of CBs preceding the RI of Hurricane Dennis (2005), Guimond et al. (2010) conclude that the accumulative effects of intense updrafts of 10–12 m $s^{-1}$ flanking CBs with the maximum value of 20 m $s^{-1}$ at 12–14 km height account for the increased warm core intensity. Clearly, the warmer the core is, the greater will be the surface pressure falls induced hydrostatically.

It is well known from the hydrostatic equation that a higher-level warm core will cause a greater surface pressure fall than a lower-level one due to the more amplifying effects of the upper-level warming (Malkus and Riehl 1960; Zhang and Fritsch 1988; Hirschberg and Fritsch 1993; Holland 1997). However, previous observational and modeling studies have shown the formation of the warm core at different heights, varying from 600 to 200 hPa (LaSeur and Hawkins 1963; Hawkins and Rubsam 1968; Hawkins and Imbembo1976; Liu et al. 1997). Thus, the reason why the warm core develops at different heights and what processes determines the height remains elusive. In particular, we even have not obtained a well-accepted theory to explain the eye subsidence generating the warm core (see the related discussion in Zhang et al. 2000, and Zhang and Kieu 2006).

In chapter 2, we have successfully obtained a 72-h (i.e., 0000 UTC 18 – 0000 UTC 21 October 2005) quadruply nested-grid (27/9/3/1 km), cloud-permitting prediction of Hurricane Wilma using a Weather Research Forecast (WRF) model

with the finest grid length of 1 km and the model top of 30hPa (or at z = 24 km). The 72-h period covers an initial 15-h spin up (referred to as pre-RI), a 21-h RI and a 36-h weakening (post-RI) stage (Figure 3.1b). Results show that (i) the record-breaking RI of Wilma occurs in the presence of high SSTs (in the range of 29°–30°C) and weak VWS (< 5 m $s^{-1}$ between 850 and 200 hPa) during RI; and (ii) the WRF model predicts about a 28 m $s^{-1}$ increase in $V_{MAX}$ and an 80hPa drop in $P_{MIN}$ during the 21-h RI period, with peak $V_{MAX}$ = 72 m $s^{-1}$ and $P_{MIN}$ = 889hPa.

In this chapter, we delve deeply into both external and internal processes leading to the RI of Hurricane Wilma (2005) in terms of surface pressure falls. This will be done mostly using the 72-h model prediction data, as presented chapter 2, unless otherwise mentioned. The objectives of this chapter are to examine (i) the spatial distribution and evolution of CBs and their roles in the formation of the upper-level warm core; (ii) the importance of the upper-level warm core in the RI of Wilma; and (iii) the dependence of CB activity, the upper-level warm core and RI on the warmth of SST. The next section presents discussion of the vertical structures and evolution of the warm core, in relation to the upper-level flow, and its importance in causing the RI of Wilma. Section 3.3 presents the statistical characteristics of CBs and their structural variations during the early stages of Wilma. Section 3.4 portrays the relationship between CBs and the upper-level warm core. Section 3.5 shows how CBs and RI depend critically on the warmth of SSTs by analyzing triply nested (18/6/2 km) grid sensitivity simulations. The conclusion is given is section 3.6.

### *3.2. Importance of the upper-level warm core*

Figure 3.1 shows the time-height cross section of perturbation temperatures [$T'(z, t)$] in relation to the time series of $P_{MIN}$ drops ($P'$) with respect to the mean vertical temperature profile [$\overline{T}(z)$] and $P_{MIN}$ at the model initial time (i.e., t = 0), respectively, superimposed with storm-relative flows, at the eye center. We see that the hurricane vortex initially has a warm core of 4-5°C centered near $z$ = 7 km. Because of the influence of moderate VWS (i.e., 5 – 7 m $s^{-1}$) and midlevel dry intrusion, Wilma exhibits a southeastward-tilted partial eyewall pattern during the early pre-RI stage as shown in chapter 2. Thus, we see two warming centers during the 6-12 h integrations: one is located at z = 4 km, and the other at z = 12 km. After the initial 6-12 h spin-up, a shallow upper warming layer of 6-8°C appears above a deep warming column in the eye. For the sake of convenience in relating the results shown in Figs. 3.1a and 3.1b, we use the word "warming" to imply a positive temperature change(s) with respect to $\overline{T}(z)$ at t = 0 in the storm-relative framework, although the environmental temperature changes during the 72-h prediction are small. Of importance is that this warming occurs in the stratosphere, as indicated by larger vertical potential temperature (θ) gradient above z = 16 km. Since the model top is set at 30 hPa, with a mean altitude of about z = 24 km, this warming is little affected by the top boundary conditions. Of further importance is that the isentropic surfaces in the upper warming layer (e.g., θ = 370 – 400 K) begin to displace downward at the onset of RI (cf. Figs. 3.1a and 3.1b). At the same time, the upper boundary of the

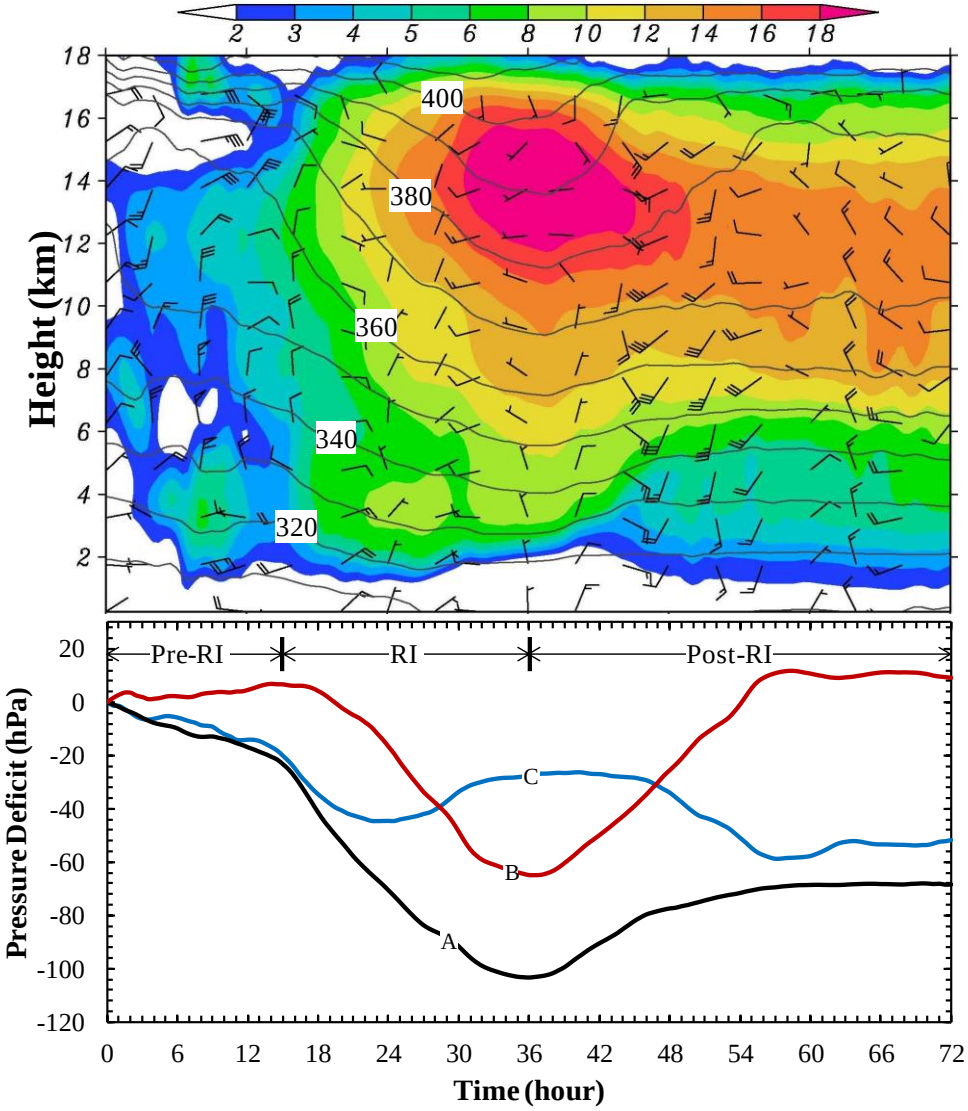


Figure 3.1. (a) Time-height cross section of temperature changes ($T'$, shaded), superposed with potential temperature ($\theta$, contoured at intervals of 10 K) and storm-relative flows (a full barb is 2.5 m $s^{-1}$), at the eye center from the 72-h prediction of Hurricane Wilma (2005) at the 3-km resolution and 30-min intervals, where $T'$ are defined with respect to the (1000 km × 1000 km) area-averaged temperatures at the model initial time ($\overline{T}$). (b) Time series of $P_{MIN}$ drops ($P'$) reproduced from the 72-h prediction (curve A), $P'$ estimated from the warm column above the θ = 380-K surface (curve B), and from the warm column beneath the θ = 380-K surface (curve C), where $P'$ is defined with respect to $P_{MIN}$ at the model initial time.

upper level warm core climbs rapidly from 14 km to 18 km and the warming above 14-km altitude develops drastically, which shifts the center of upper level warm core from 12 km in pre-RI stage to 14 km in RI stage. Since the motion in hurricane eye, especially in the upper level, is adiabatic and frictionless, the air parcel has to move following isentropic surfaces. By examining the evolution of isentropic surfaces, the origin of warm air in the upper level warm core can be identified. Fig. 3.1 shows the warm air is originally located in the stratosphere in pre-RI stage and descends to the troposphere in RI, reaching the lowest altitudes with the peak warm core occurring at the time of the peak storm intensity (i.e., t = 36 h). During this 21-h RI, the air at the tropopause, as indicated by $\theta$ = 370 K, descends from $z$ = 16 to 9 km, leading to a strong warming column of stratospheric origin with the peak amplitude of more than 18°C near $z$ = 14 km. This peak warming core is similar in magnitude to but about 2 km higher than that found in early observational studies of LaSeur and Hawkins (1963), Hawkins and Rubsam (1968), and Hawkins and Imbembo (1976).

The isentropic surfaces begin to climb back after reaching the peak intensity while the warming core weakens and shifts downward during post-RI, corresponding to the rise in $P_{MIN}$ of Wilma. As shown in chapter 2, this timing is consistent with an eyewall replacement cycle (ERC) beginning near 36:00, during which the original eyewall is replaced by an outer eyewall with doubled radii of maximum wind (RMW). The warming core descends to 12 km at 48:00, i.e., at a level close to that occurring during pre-RI. It remains at that level until the end of the 72-h integration, which is consistent with the near-steady state of $P_{MIN}$ (cf. Figs. 3.1a and 3.1b). The above results reveal that the upper-level warming, the inner-core structural changes

and the storm intensity are all closely related. In particular, the RI, rapid weakening, and peak intensity of Wilma coincide well with the steep downward and upward sloping, and the lowest elevation of isentropic surfaces, respectively.

Note the pronounced changes in static stability in the column above the $\theta$ = 370-K surface due to the dry adiabatic rearrangement of isentropic surfaces. Of interest is that the evolution of this isentropic surface resembles in trend the time series of $P_{MIN}$ (cf. Figs. 3.1a and 3.1b), implying that the $P_{MIN}$ falls are closely related to the upper-level warming of stratospheric origin.

Since RI is examined herein in terms of surface pressure falls (i.e., *P'*), we wish to show, through the simple use of the hydrostatic equation, that it is the warming core of stratospheric origin that causes RI of Wilma. Of particular relevance is that under hydrostatic balance warming at lower temperatures aloft can produce much greater impact on surface pressure falls than lower-level warming because of the more exponential effects of the upper-level warming (Malkus and Riehl 1960; Zhang and Fritsch 1988; Hirschberg and Fritsch 1993; Holland 1997). In addition, the subsidence warming of stratospheric air tends to be greater in magnitude than that of tropospheric air, as shown in Fig. 3.1a. Thus, the upper-level warming, especially with stratospheric origin, is more effective than the lower-level warming in reducing $P_{MIN}$. Figure 3.1b, in which the $\theta$ = 380-K surface is used to separate contributions of the warming from stratospheric and tropospheric origins to the time series of P', demonstrates this point. The three curves, labeled as "A", "B", and "C", in Figure 3.1b are obtained as follows: (i) the time series of the model output $P_{MIN}$, as shown in Fig. 2.4, is reproduced as P' with respect to $P_{MIN}$ at t = 0 (curve A) by integrating the

hydrostatic equation from the model top downward with the total temperatures [i.e., T = $\overline{T}$(z) + T'(z, t)] in order to ensure the absence of significant errors; (ii) repeat step (i) except by setting $T'(z, t) = 0$ in the layers below the θ = 380-K surface (curve B); and (iii) repeat step (i) except by setting $T'(z, t) = 0$ in the layers above the θ = 380-K surface (curve C). Since the $\theta$ = 380-K surface originates from the lower stratosphere (Figure 1a), the results so obtained tend to underestimate contributions of the upper-level warm core.

It is apparent from Figure 3.1b that curve B, representing contributions from the upper-level warming core, resembles in shape curve A including total contributions, and exhibits a 72-hPa fall in $P_{MIN}$ during the 21-h RI, followed by a 76-hPa rise during the 21-h weakening stage. It should be noted that such large variations are also highly dependent on the warm column depth used in the calculations because of the pronounced changes in the elevation of the $\theta$ = 380-K surface during and after the RI stage (Figure 3.1a). If only the peak intensity at t = 36 h is considered, the warming columns above and below the $\theta$ = 380-K surface (located at $z \approx 11$ km) account for a drop in $P_{MIN}$ of 64 hPa (curve B) and 24 hPa (curve C), respectively, from the initial intensity. This indicates that the warming core of stratospheric origin could contribute more than twice as much as the lower-level warming column to the RI of Wilma. Note that the sum of contributions from the warming columns above and below the $\theta$ = 380-K surface does not equal the total $P_{MIN}$ deficit because of the exponential dependence of $P_{MIN}$ on temperature changes in the vertical. In the present case, the exponential dependence for the vertical column below the $\theta$ = 380-K surface more than doubles the pressure difference obtained between steps (ii) and (iii) at $z \approx$

11 km (i.e., 19 hPa compared to 40 hPa at $z$ = 0). Nevertheless, the warming column below the $\theta$ = 380-K surface accounts mostly for the initial spin-up of Wilma (cf. curves C and A). Without the upper-level warming, the storm may cease deepening after 22-24 h into the prediction, and fail to achieve the RI rate.

To gain insight into the relationship between the thermal and flow fields in the core region, Figs. 3.2a, b show their axisymmetric vertical structures at two time levels during the RI and post-RI period, respectively. The in-plan flow vectors exhibit the typical in- up- and outward secondary circulation of a mature TC, which influences the general warming pattern. This is especially true at later stages in the upper outflow layer where the warming spreads more laterally outward (Fig. 3.2b). Of particular relevance is that the peak warming core is located in the same layer as the upper-level outflow in the outer region, e.g., the 13 – 15 km layer during RI (Fig. 3.2a) and the 11-13 km layer during post-RI (Fig. 3.2b). It is obvious that the development of strong divergent outflow tends to protect the warming core from ventilation by environmental flows (cf. Figs. 3.2 and 3.1). An analysis of the time series of vertical wind profiles in the eye, as given in Fig. 3.1a, reveals that the upper-level warming magnitudes are indeed correlated with those of the upper-level SRFs. That is, the SRFs in the eye are about 10 - 20 m $s^{-1}$ in a deep layer (i.e., $z$ = 2 - 18 km) during the pre-RI stage, which is consistent with the high cloud asymmetries under the influence of moderate VWS. Clearly, such intense SRFs tend to prevent the accumulation of warming air in the eye by ventilating it into the environment. Of

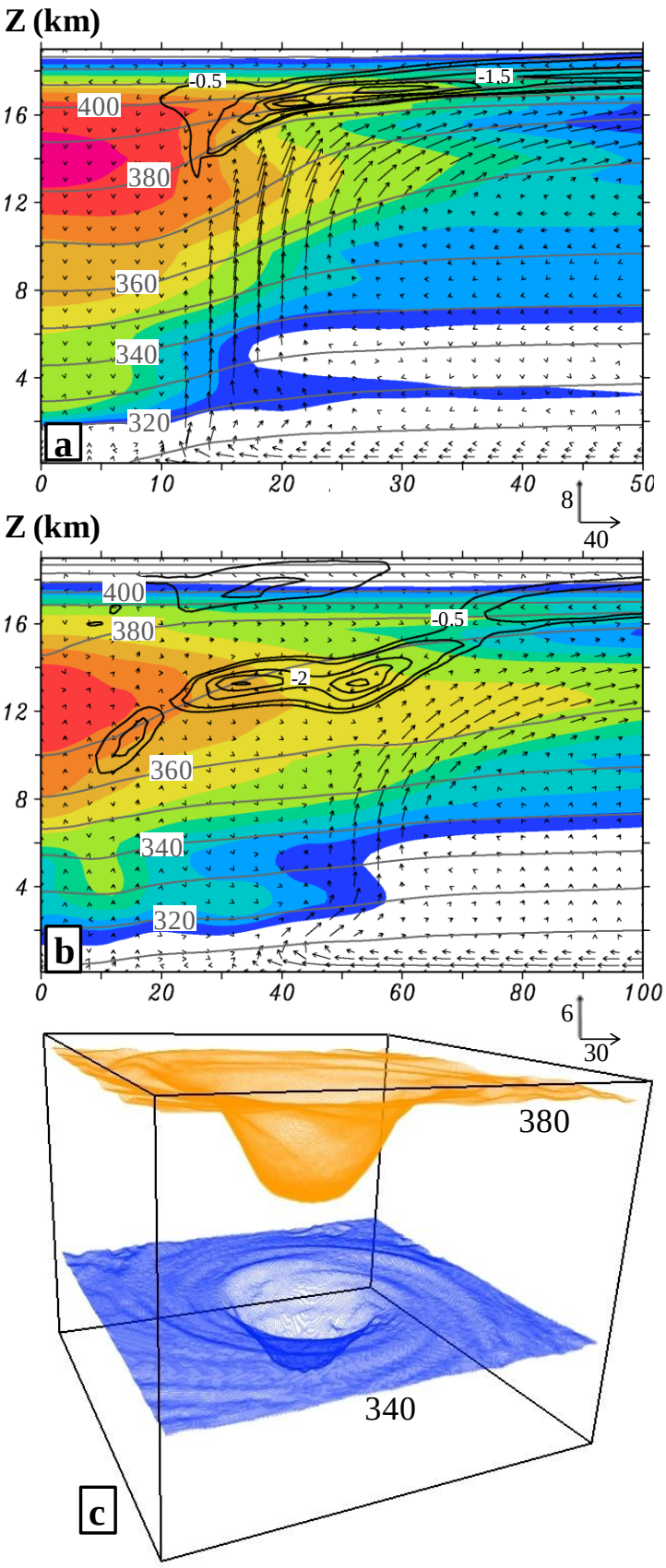
Z (km)
-0.5
-1.5
400
380
360
340
320
a
16
12
8
4
0
10
20
30
40
50
8
40
Z (km)
400
380
-0.5
-2
360
340
320
b
16
12
8
4
0
20
40
60
80
100
6
30
380
340
c

Figure 3.2. Radius-height cross section of temperature deviations [$T'$(z,t), shaded] with respect to the (1000 km × 1000 km) area-averaged temperatures [$\overline{T}$(z)] at the model initial time, superposed with potential temperature ($\theta$, contoured at intervals of 10 K), in-plane flow vectors (vertical motions are multiplied by 5), and the upper-level radial inflows (contoured at 0.5 m $s^{-1}$) from (a) the 30-h; and (b) the 54-h prediction of Hurricane Wilma (2005). Different horizontal and vertical motion scales (m $s^{-1}$) are given beneath each frame. (c) A three-dimensional view of the 380- and 340-K isentropic surfaces in a 100 km × 100 km × 13.5 km (i.e., z = 3.5-17 km) box from the 36-h prediction.

equal importance is that according to geostrophic adjustment theory (Blueman 1972), most of the convectively generated mass perturbations tend to be propagated away (more vertically) by high-frequency internal gravity waves at the earlier stages, especially in the lower stratosphere where static stability is high (Fovell et al. 1992). This will be further discussed in section 3.4. The upper-level SRFs decrease rapidly to less than 5 m $s^{-1}$ at the onset of RI, and achieve a nearly calm condition at the time of the peak intensity, confirming the important roles of the outflow in protecting the warm core from ventilation by the environmental flows. The SRFs above 14-km altitude become re-intensified after the ERC, which coincides with the weakening of the upper-level warming. Meanwhile, the warming core shifts to a lower layer as does the upper outflow.

Note the presence of an inflow layer of about 2 - 3 m $s^{-1}$ originating in the lower stratosphere above the upper outflow layer. It begins to emerge with little rotation at the time of the eye formation, and at the later stages it exhibits more pronounced cyclonic rotation, as will be shown next, especially near the eye, as a

result of absolute momentum conservation. The inflow air could descend isentropically, e.g., following roughly the $\theta$ = 370 K surface, toward the warm core from the outer region at the radius of more than 100 km (Fig. 3.2b). Although this has not been documented in any of previous observations, numerous model simulations have shown its existence (e.g., Rotunno and Emanuel 1987; Liu et al. 1999), even in a dry hurricane-like vortex (Mrowiec et al. 2011), but with little attention to the significance of this inflow layer. Early theoretic study did shed light on the generation of this thin layer of inflow. Shapiro and Willoughby (1982) showed that a momentum source at upper level will induce an outflow layer sandwiched by inflow layers above and below, which is the result of mass continuity.

While the upper-level warming accounts for most of Wilma's deepening, it is essentially the high elevation of the upper outflow layer that to a certain extent makes it a record-breaking storm. Specifically, the elevation of the outflow layer is about 1-2 km higher than that of several intense hurricanes shown by the previous studies, such as Andrew of 1992 (Liu et al. 1999), Dennis of 2005 (Rogers 2010), and Opal of 1995 (Bosart et al. 2000). In the present case, the high outflow elevation benefits from the presence of a high tropopause (at about 100-130 hPa or 16 km), and intense latent heat release associated with CBs being tied to warm SSTs (of 29 – 30°C). In particular, the maximum potential intensity theory (MPI) of Emanuel (1986, 1988) indicates that a higher-altitude outflow layer tends to boost the thermodynamic efficiency of Carnot's engine that converts sensible and latent heat energy extracted from the underlying warm ocean and ultimately given up in the upper outflow, thereby increasing the storm intensity. In this regard, the eye thermodynamics

presented herein is consistent with the eyewall thermodynamics of MPI theory. Moreover, a higher altitude of an inflow layer, residing above the upper outflow layer, can effectively carry the higher-θ air from the far environment all the way into the hurricane eye where it descends adiabatically to enhance the warm core due to the presence of little inertial stability (Fig. 3.2b).

Figure 3.2c provides a three-dimensional view of the isentropic surfaces of 380 K and 340 K at the time of the peak intensity, i.e., 36:00. Both surfaces are funnel-shaped in the inner core region with their bottoms at 5 and 3 km lower than their peripheries for the $\theta$ =380-K and $\theta$ = 340-K surface, respectively. The different downward displacements of the two surfaces are attributable to locally different static stabilities in the eye. Because the $\theta$ = 380-K surface is located above the upper outflow layer with little diabatic processes occurring, the upper-level inflow of stratospheric air must follow closely this isentropic surface, causing strong descending motion and the generation of an intense warming core. In the outer region, the $\theta$ = 380- and 340-K surfaces are almost flat with some wavy patterns, and they are associated with gravity waves and spiral rainbands, respectively.

### *3.3. Statistical characteristics of convective bursts*

Before discussing how CBs contribute to the formation of the upper-level warming core, let us examine first some statistical characteristics of CBs. Fig. 3.3 shows the horizontal distribution of CB-elements at a few selected times during the pre-RI and RI stages. Because of the large spatial and temporal variabilities of updrafts and their interactions, including merging and splitting, it is often not possible to trace the evolution of individual CBs, except for a few well-defined cases as will

be shown later. Thus, CB-elements, rather than CBs per se, are statistically examined. We see from Fig. 3.3 that most CB-elements at 6:00 are distributed along a spiral rainband in the southeast quadrant, which corresponds more or less to the north-northwesterly VWS of about 5 m $s^{-1}$. Although this VWS is relatively weak, it accounts for the asymmetric structures of eyewall convection and CBs at the early stage. The CB band tends to be displaced cyclonically as the storm size shrinks and the eyewall becomes better defined. It moves into the northeastern quadrant 3 h later (Fig. 3.3b). Starting from 12:00, more CB-elements begin to develop in the eyewall (cf. Figs. 3.3c-e) where the high equivalent potential temperature ($\theta_e$) air and strong convergence are typically located (Liu et al. 1999). By 15:00, almost all CBs take place in the eyewall as it becomes more symmetric (Fig. 3.3d). Of interest is that the area coverage of CBs in the inner-core region decreases rapidly as the storm intensifies. This rapid decrease could be attributed partly to the increased stiffness in the eyewall that tends to force moist convection to behave more in a slantwise fashion (Jorgensen 1989; Liu et al. 1997, 1999), and partly to the rapid decrease in convective areas as the eyewall contracts. The increased stabilizing effects of the upper-level warming may also help weaken updraft intensity. Some CBs could still occur in the outer rainbands due to the presence of large convective available potential energy (CAPE) associated with warm SSTs (e.g., Fig. 3.3c).

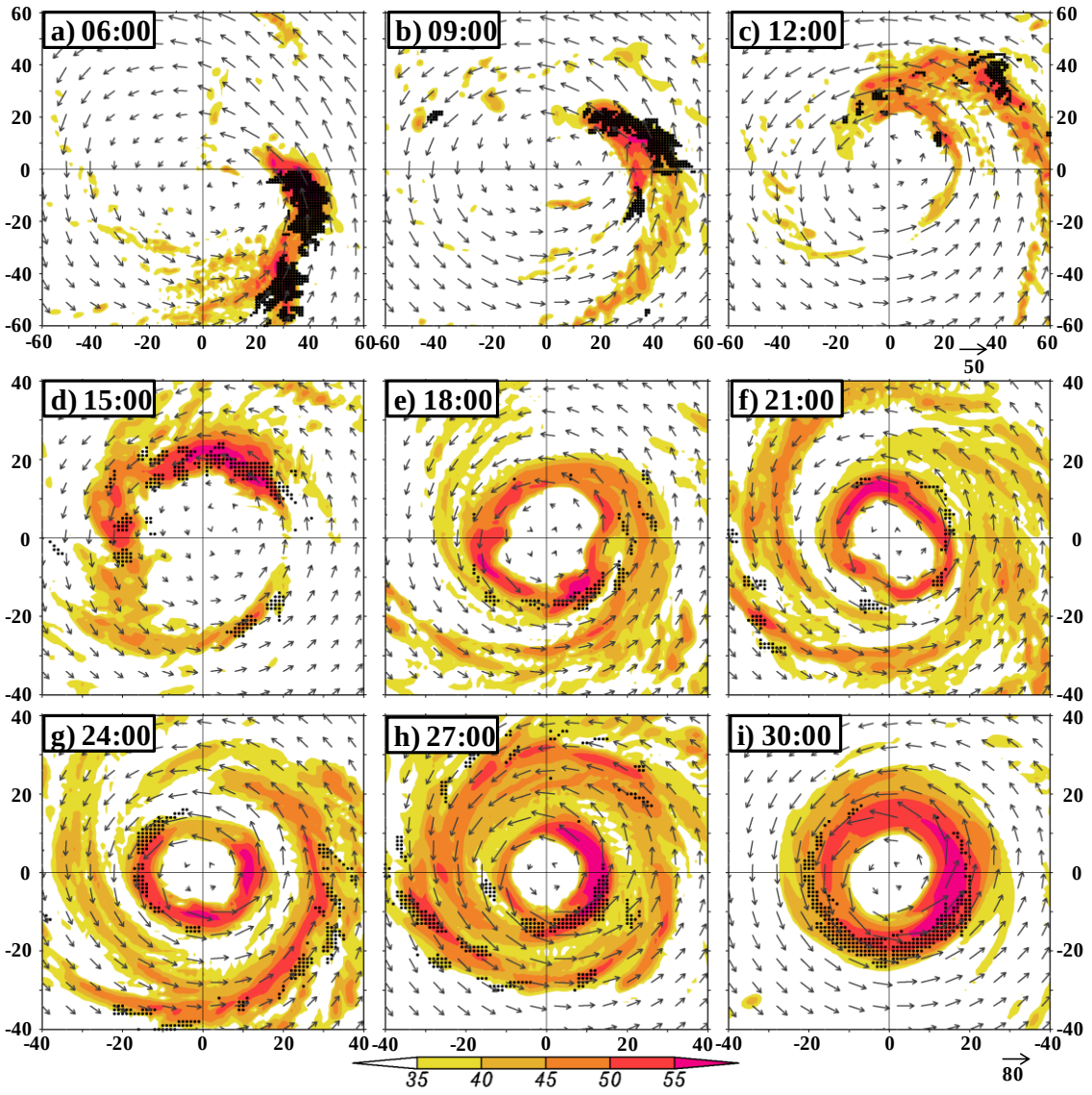


Figure 3.3. Horizontal maps of the predicted radar reflectivity (shaded) and storm-relative flow vectors at z = 1 km, and convective bursts (dotted) that are obtained for three time levels at ± 5 min intervals. They are plotted at 3-h intervals during the period of 6:00 – 30:00. Note that different subdomain sizes of 120 km × 120 km and 80 km × 80 km, centered at $P_{MIN}$, with different flow vector scales (m $s^{-1}$), are used for (a) – (c), and (d) – (i), respectively.

The area coverage of CBs experiences another cycle of rapid decreases just shortly after the onset of RI (cf. Figs. 3.3d and 3.3e). This occurs as an outer eyewall forms near R = 30 km during the 18:00 – 27:00 period (cf. Figs. 3.3e-3.3h), reducing

the supply of high-$\theta_e$ air to the inner eyewall. Despite the formation of the outer eyewall, the inner eyewall could still keep contracting with significant CB activity, thus causing little changes in the rate of RI (Fig. 3.1b). Note that because of the presence of weak VWS (i.e., < 5 m $s^{-1}$), cyclonically travelling CBs appear in the different quadrants of the inner and outer eyewalls during RI. The RI is only halted briefly as the two eyewalls merge shortly after 27:00 (Figs. 3.3h,i and 3.1b), which is referred as a fictitious eyewall-merging scenario forming an annular eyewall in chapter 2. The CB area coverage increases substantially, covering more than a semicircle, after the annular eyewall is formed (Fig. 3.3i). This appears to account for the resumption of RI until reaching the storm's peak intensity at 36:00 (cf. Figs. 3.3i and 3.1b). As will be seen in section 3.5, the storm could continue its RI, even during the double eyewalls stage, because of the continuous development of CBs in the inner eyewall (Figs. 3.3f-3.3i) that is in turn determined by the underlying warm SSTs.

Figure 3.4a shows the temporal evolution of CB activity in terms of the number of total grid columns containing updrafts that are at least 15 m $s^{-1}$ above z = 11 km. The initial CB activity is determined by large CAPE in the bogussed vortex, and it is peaked after 02:00 with slightly over 1000 CB-elements or an equivalent area coverage of over 1000 $km^2$ at 1-km horizontal grid spacing. The CB activity decreases rapidly after the first 6-h model adjustment, during which rapid contraction occurs, as also shown in Fig. 3.3. The CB activity maintains at a stable level from the onset of RI to 24:00, followed by an increased CB area coverage during the formation of the annular eyewall (cf. Figs. 3.3d-i and 3.4a).

The CB activity regains its coverage a couple hours after Wilma reaches its peak intensity, i.e., during the ERC, but it occurs mostly in the outer eyewall. Of interest is that the pronounced increases in CB activity produce little changes in $P_{MIN}$ (cf. Figs. 4a and 1b). This can be explained by the low efficiency of diabatic heating in the large-sized eyewall (Hack and Schubert 1986). Subsequently, the CB activity remains at a dormant state with occasional spikes between 42:00 and 62:00, corresponding to the weakening stage of the storm (cf. Figs. 4a and 1b). The CB activity is completely absent during the final 10-h (i.e., 62:00 – 72:00) when the storm enters a steady state. Overall, the evolution of the CB activity over the 72-h period corroborates qualitatively the previous findings that CBs are active preceding and during RI and they rarely occur when a TC reaches its quasi-steady state or starts weakening. Here we add that (i) fewer CBs occur during RI than those during pre-RI; and (ii) if the weakening of TCs results from an ERC, then CBs tend to occur in the outer eyewall. Of course, fewer CBs during RI do not mean smaller contributions to the RI of Wilma. In contrary, the contributions of CBs to the RI through the upper-level warm core are much greater than those at the earlier stages due to the generation of a balanced cyclonic circulation in the core, as will be further discussed in the next section.

Figure 3.4a also shows the mean radius where CB-elements take place with respect to the RMWs at z = 1 and 11 km. Wilma's eyewall is nearly upright, with only 3-5 km outward tilt up to z = 11 km during pre-RI and RI, but large outwardly tilted (i.e., about 30 km) after the ERC. Except for the first 1- 2 h vortex adjustment, all the three radii contract rapidly during the subsequent 12-14 h pre-RI period, and

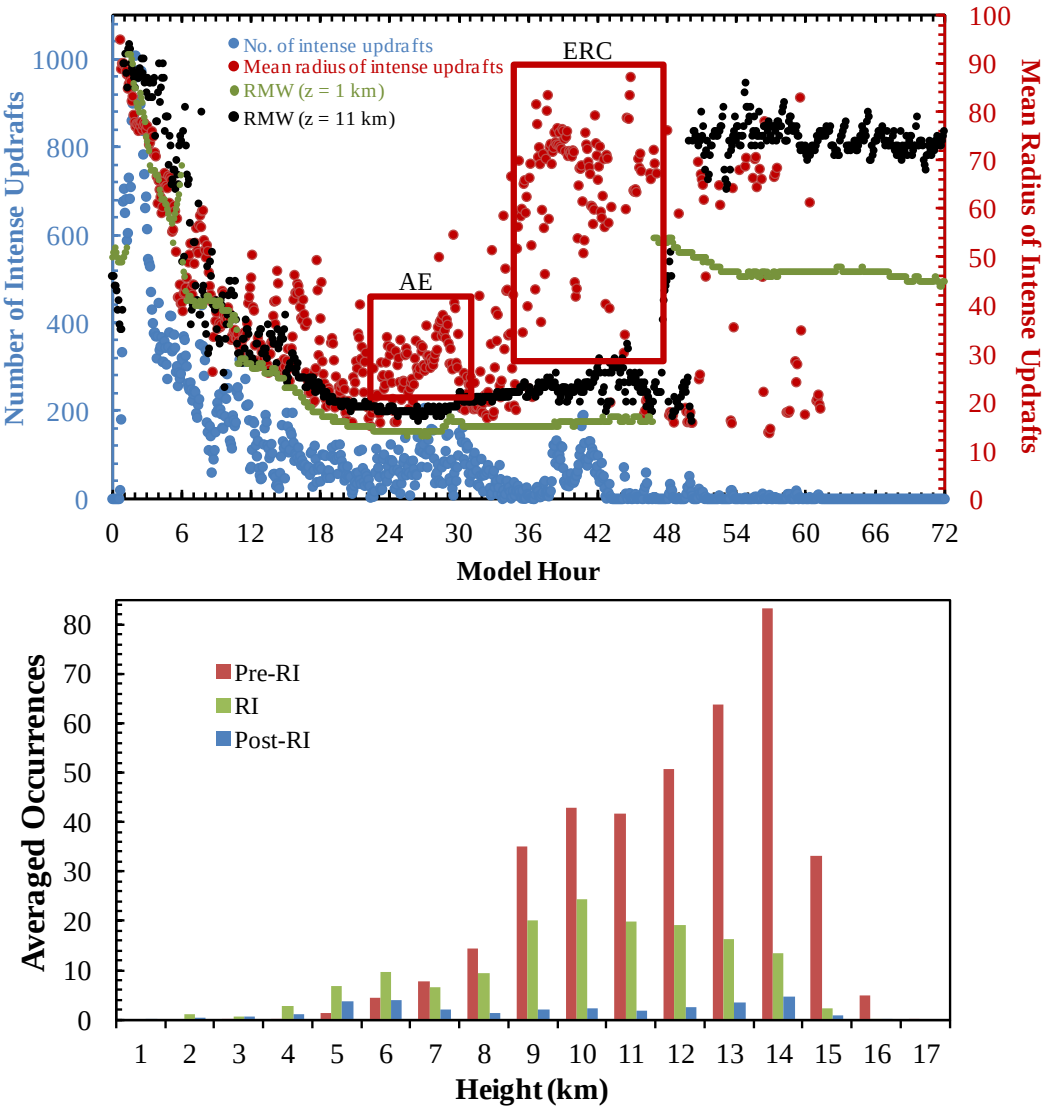


Figure 3.4. (a) Time series of the convective burst activity in terms of the number of total grid columns containing CB-elements above 11-km height, the mean radius of the CB-element occurrences, the RMW at 1-km and 11-km altitude. Symbols, "AE" and "ERC", denote the annulus eyewall and eyewall replacement cycle, respectively. (b) The height distribution of the peak updraft altitudes for the number of their occurrences averaged during the pre-RI, RI, and post-RI stages. In both maps, CB-elements are taken within the radius of 100 km from the center from the 72-h prediction of Hurricane Wilma (2005) at the 5-min resolution.

the occurrences of CB-elements straddle the RMWs. Note that the CB activity becomes scattered with more located outside the RMW during the 10:00 – 32:00 period. This scattered CB activity could be attributed partly to its development in spiral rainbands (i.e., for those occurring more than 10 km outward from the RMW), and partly to the outward tilt of CB-elements above z = 11 km as they overshoot slantwise outward into the lower stratosphere. Again, the formation of the annular eyewall accounts for the sharp fluctuations in the radius of CB-elements around 27:00. Note also that the RMW at z = 11 km increases slightly after 30:00 while the RMW at z = 1 km remains constant, implying the more slantwise nature of CB-elements and the eyewall. This is consistent with the rapid decrease in CB activity in the inner-core region during the final 6-h RI period. During and after the ERC, a majority of CB-elements occur in the outer eyewall, mostly near the RMW at z = 11 km, indicating that they slope outward in the same manner as the eyewall.

To examine the likely upward penetration of CBs and their detrainment in the inner-core region, Fig. 3.4b shows the height distribution of the peak updraft altitudes for the number of their averaged occurrences during the pre-RI, RI and post-RI stages. Note that they are not necessarily all associated with CBs, since the criterion for the peak updrafts of greater than 15 m $s^{-1}$ is not limited to the levels above z = 11 km. Despite this relaxed criterion, we still see that the peak updrafts take place mostly in the upper troposphere during pre-RI, with their most preferred altitude occurring at z = 14 km in coincidence with the warming core level. This preferred altitude shifts to 10 km during RI, with another preferred altitude at 6 km where the melting level is roughly located. Nevertheless, a sizeable portion of peak updrafts still occur at z = 14

km and above. Two preferred peak updraft levels appears during post-RI: one at 6 km, and the other at 14 km; the latter is more associated with CBs in the outer eyewall. Since the peak updraft level denotes roughly the equilibrium level, above which the rising air in an updraft begins to detrain, a higher peak updraft level implies the more likely penetration (with detrainment) of deep convection into the lower stratosphere. Thus, the above result confirms further that the warming core at z = 14 km results mostly, if not all, from the compensating subsidence of the stratospheric air due to the development of intense CBs during the pre-RI and RI stages.

### *3.4. Convective bursts and the upper-level warm core*

After seeing the statistical characteristics of CBs, we can explore the roles of CBs in the formation of the eye and upper-level warm core. This will be done by examining the upper-level flows and clouds near the onset of RI when a well-defined warm core and eye begin to form and during RI stage.

#### *3.4.1. Formation of the eye*

Figure 3.5 traces the evolution of four CBs, labeled as "A," "B," "C," and "D," in the inner-core region during the period of 14:35 – 15:45 through snapshots of the model-predicted outgoing long wave radiation (OLR), superposed with vertical motion at z = 15 km. The OLR is calculated using the model-predicted cloud top temperature, which can be considered as a surrogate for satellite images showing brightness temperature. Note that (i) at 15-km altitude, most updrafts that are weaker than 5 m $s^{-1}$ are filtered; and (ii) CBs in the eyewall with significant updrafts can be well resolved by many CB-elements. At 14:35, which is 25 min earlier than the map

shown in Fig. 3.3d, two CBs, A and B, are evident around the 1-km altitude RMW (Fig. 3.5a). CB A, located to the west and slightly outside the RMW, consists of a few

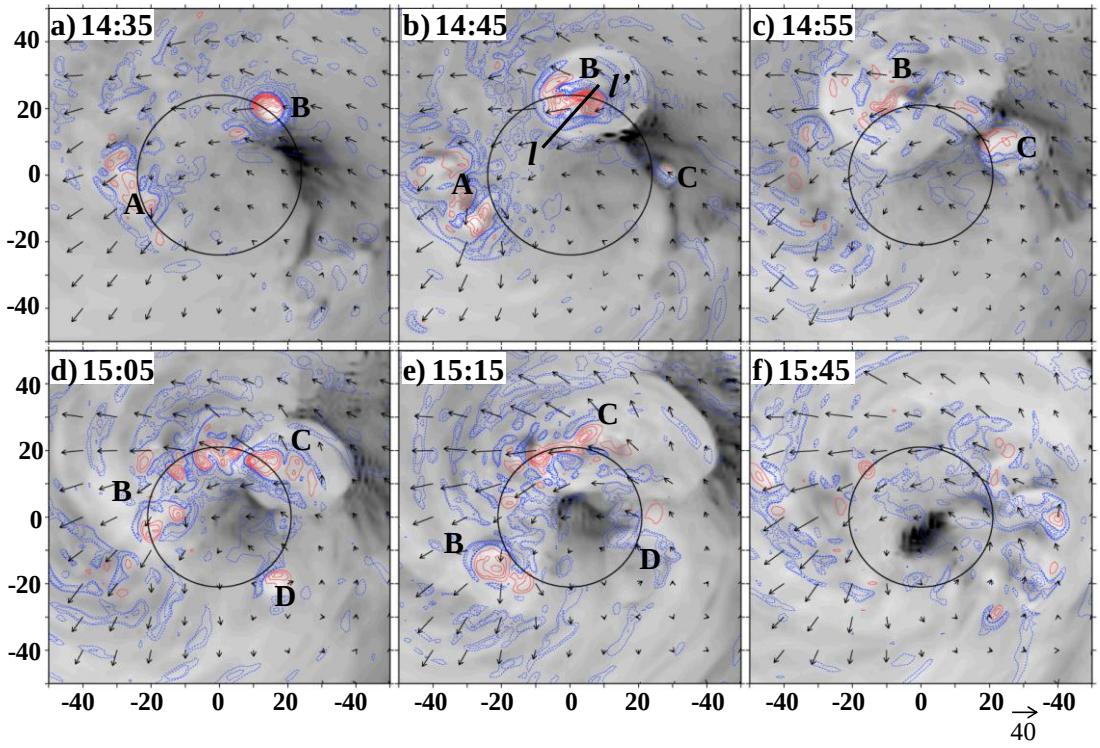


Figure 3.5. Horizontal maps of the predicted outward long-wave radiation (OLR), superimposed with storm-relative flow vectors [see the scale beneath the frame (f)] and vertical motion (upward/red-contoured at intervals of 5 m $s^{-1}$, downward/blue-contoured at -0.5, -1, -2, -4, -6, -8, and -10 m $s^{-1}$) over the subdomains of 100 km × 100 km, centered at $P_{MIN}$, that are taken at intervals of 10 minutes, except for (f) and (g) between which a 30-minute interval is used, during the period of (a) 14:00 to (g) 15:45 (i.e., onset of RI). The mean RMW at z = 1 km is also plotted. Letters, "A" – "D", are used to trace the evolution of four different convective bursts (see text). Line ***l l'*** in (b) denotes the location of a vertical cross section used in Fig. 3.6.

scattered updrafts flanked by compensating subsidence, so it has an azimuthal scale of 20-25 km and a width of about 10 km. CB A reaches its maximum coverage near 14:45 and then weakens, leaving its footprints as outward emitting (subsidence/cloud-

free) wave-like bands. Thus, most of the subsidence warming outside the RMW, where both the SRFs and static stability are large, may be viewed as being dispersed away by both SRFs and high-frequency gravity waves (Figs. 3.5b-d).

In contrast, CB B displays as a bright spot centered at the RMW with a horizontal scale of about 10 km to the northeast (Fig. 3.5a). To the southeast of B is an extensive cloud-free region that is caused by compensating subsidence from previous CBs, and it will be covered soon by convective clouds from the subsequent CB development. A distinct eye will not form until the onset of RI, i.e., 1 h later, when the RMW contracts further (Figs. 3.5b-f). Collocated with B is an intense upward motion as strong as 35 m $s^{-1}$ (see Fig. 3.6). The size and intensity of this CB are similar to those observed, e.g., by Houze et al. (2009), Guimond et al. (2011), and Heymsfield et al. (2001). A further examination of the vertical motion field reveals that this strong updraft results from the merging of 2-3 updrafts at the lower levels. A similar scenario is also observed by Guimond et al. (2010) in Hurricane Dennis (2005), in which two updrafts merge into a wide one (~ 5-6 km) with the maximum intensity reaching 20 m $s^{-1}$. Surrounding B is a ring of compensating subsidence with the magnitudes as strong as 10 m $s^{-1}$ (Fig. 3.6)

Ten minutes later, the cloud top associated with CB B expands into a blob of some 30 km in diameter as it slowly moves cyclonically along the RMW (Fig. 3.5b). Its updraft region is now distorted into a bow shape with two local maxima, and it is surrounded by subsidence with stronger descent occurring inside the RMW. Its cloud top expands rapidly outward to 50 – 60 km in radius with increased divergence as the peak updraft of B decreases in the next 30 minutes (Figs. 3.5b-e). Of interest is that

three localized updrafts of more than 15 m $s^{-1}$ are spawned along the RMW from the expanding clouds of B at 15:05. They are found to grow upward from the lower layers during the previous 30 minutes, as mentioned in the preceding paragraph.

Another CB, i.e., "C", is initiated in the cloud-free region to the southeast of B at 14:45 (Fig. 3.5b). At this time, its peak updraft is only 14 m $s^{-1}$ at z = 13 km and 8 m $s^{-1}$ at z = 15 km, so it does not meet the minimum updraft intensity threshold for a CB until 14:55. Because of its weak intensity, C's updraft tilts more outward with height than B, as indicated by their central locations with respect to the 1-km height RMW (Fig. 3.3b). Nevertheless, CB C could produce 30-dBZ radar reflectivity at 15-km altitude at its most intense stage at 15:05 (not shown). The continuous expansion and cyclonic propagation of the CBs, together with the growth of C following the evolution of B allow the upper-level clouds to wrap around with time, and then a cloud-free eye becomes more evident inside the RMW (Figs. 3.5c-e). That is, despite the fact that most of the subsidence warming outside the RMW is ventilated away by the strong divergent outflow and high-frequency gravity waves, more subsidence bands begin to take place as lower-frequency propagating gravity waves inside the RMW where static stability is significantly reduced (see Liu et al. 1999, and Fig. 2 herein). This is especially true at 15:05 and 15:15 when the eye starts forming. Clearly, both B and C make more significant contributions than the other convective elements in the eyewall to the formation of the eye, at least during this early stage of the eye formation.

The fourth discernable intense CB, i.e., "D," during the 1-h mapping period is initiated near 15:05 in the southeast quadrant of the eyewall (Fig. 3.5d). CB D is the

weakest and shortest lived (a traceable period of less than 20 minutes) among the four CBs, whereas CB B is the strongest with a traceable period of more than 40 minutes. Fig. 5f shows a more symmetric cloud pattern with a small but clear eye at the vortex center, corresponding closely to the onset of RI. Unlike the earlier cloud-free region (e.g., at 14:35), the eye remains cloud-free with nearly calm winds at the center throughout the rest of the 72-h integration. The evolution of clouds from an asymmetric to a symmetric pattern and the subsequent eye formation as a result of CB episodes have also been documented by Guimond et al. (2010) in the observational analysis of Hurricane Dennis (2005).

As an example, Fig. 3.6 shows the vertical structures of CB B at 14:45. This CB has a radial scale of about 10 km, with the peak updraft of 35 m $s^{-1}$ at z = 15 km, the radar reflectivity of greater than 35 dBZ at z = 16 km, and the cloud top reaching 17.5-km height into the lower stratosphere. In addition, its updraft core takes place slightly inside the local RMW where the highest-$\theta_e$ air is located. Of relevance is that this upper-level massive updraft is flanked by divergent outflows or cloud detrainment, as indicated by both SRF vectors and reflectivity "anvils," with the inward branch descending from 17-km altitude into the eye. The subsidence could extend radially to the eye center and down to about 10-km altitude, which are consistent with the collectively generated warming (and drying) shown in Figs. 1 and 2. In this context, CBs after 15:00 must play an important role in generating an intense upper-level warm core for the RI of Wilma, especially when considering the continuous contraction of the eyewall (see Figs. 3.1, 3.3, and 3.9). Note that this subsidence tends to propagate cyclonically downstream in the eye, as shown by Liu et

al. (1999). This is why the vertical cross section used in Figure 3.6 is not radially taken.

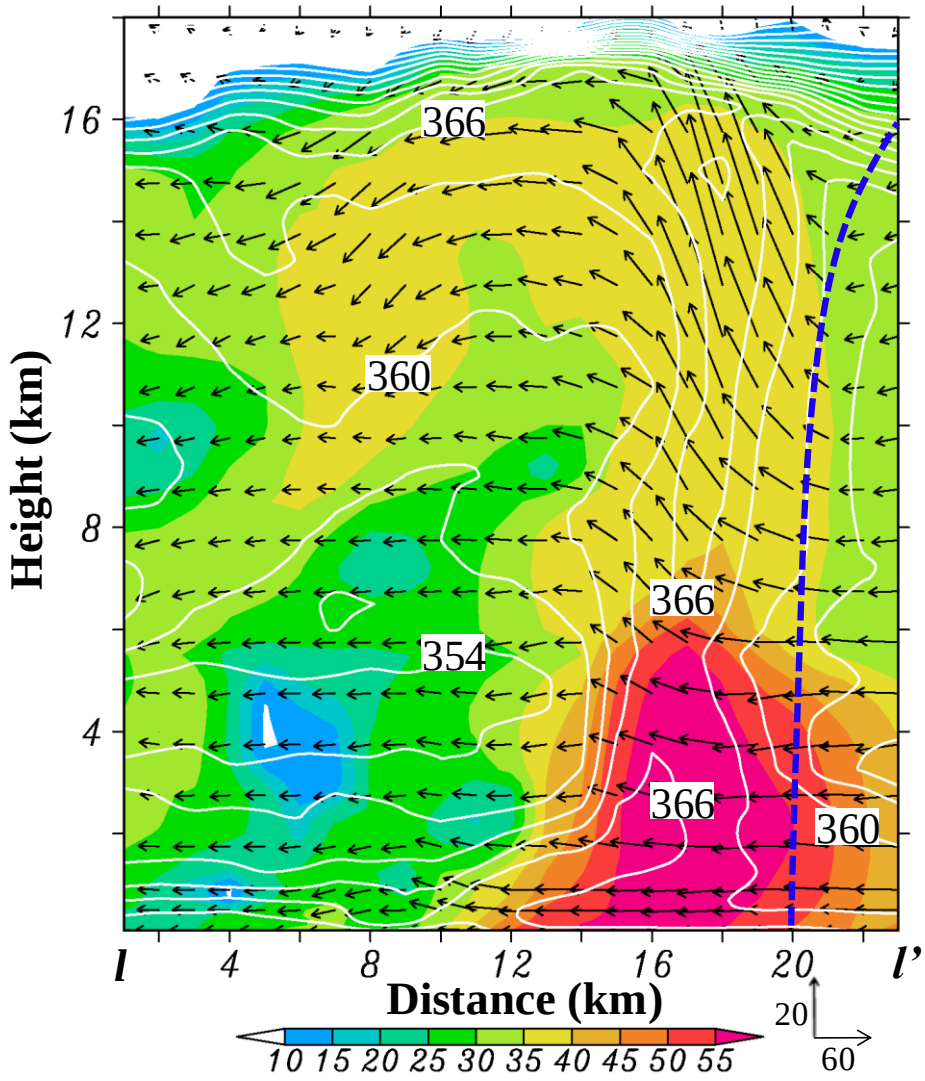


Figure 3.6. Vertical cross section of radar reflectivity (shaded), the equivalent potential temperature (white solid lines at intervals of 3 K), superimposed with in-plane storm-relative flow vectors, that is taken at 14:45 along line ***l l'*** in Fig. 3.5b. Thick dashed lines denote the vertical distribution of the local RMW.

*3.4.2 Evidence of detrainment warming*

Fig. 3.4 shows the convective bursts are much less active in RI stage with the lower altitude where maximum vertical motion is located. Does the less activity can contribute to the substantial warming in the eye? In this section, we will show the evidence of contribution from detrainment warming in the rapid development of the upper level warm core.

Figure 7 shows the distribution of horizontal perturbation wind vectors in the upper inflow layer (i.e., at $z$ = 17.5 km), i.e., after removing a subdomain-averaged east-southeasterly flow of 6 m $s^{-1}$. In contrast to divergent outflows in the layers below, the perturbation winds show a cyclonic inflow with weak winds in the (lower pressure) core region (roughly within a radius of 30 km from the eye center), although they are influenced by propagating gravity waves (Liu et al. 1999). Associated with the cyclonic inflow component is the distribution of spirally minimum temperature in the cloudy region at this level is 197 K, which is clearly in a stratospheric layer. These stratospheric cloud hydrometeors must be produced by overshooting CBs, which are defined herein as the updrafts of at least 15 m $s^{-1}$ in the upper troposphere (i.e., above z = 11 km). Houze et al. [2009] also analyzed such deep, intense convective updrafts in Hurricane Ophelia (2005) from Doppler radar data. One can see that the CBs, taken at the two times at a 5-minute interval, develop in the vicinity of the radius of maximum wind (RMW), where the highest equivalent potential temperature in the eyewall is typically present [see Figure 3 in Liu et al. 1999]. These CBs decrease in intensity as they overshoot slantwise outward into the

lower stratosphere, leaving their footprints as the spiral cloud bands aloft. Thus, the more pronounced converging inflows within the inner-core region enclosed by spiral cloud bands are indicative of the collective mass detrainment into the eye from the CBs in the eyewall. It is this horizontal convergence or inflow that causes the eye subsidence accounting for the formation of a warm core within the upper outflow layer (cf. Figs. 3.2 and 3.3).

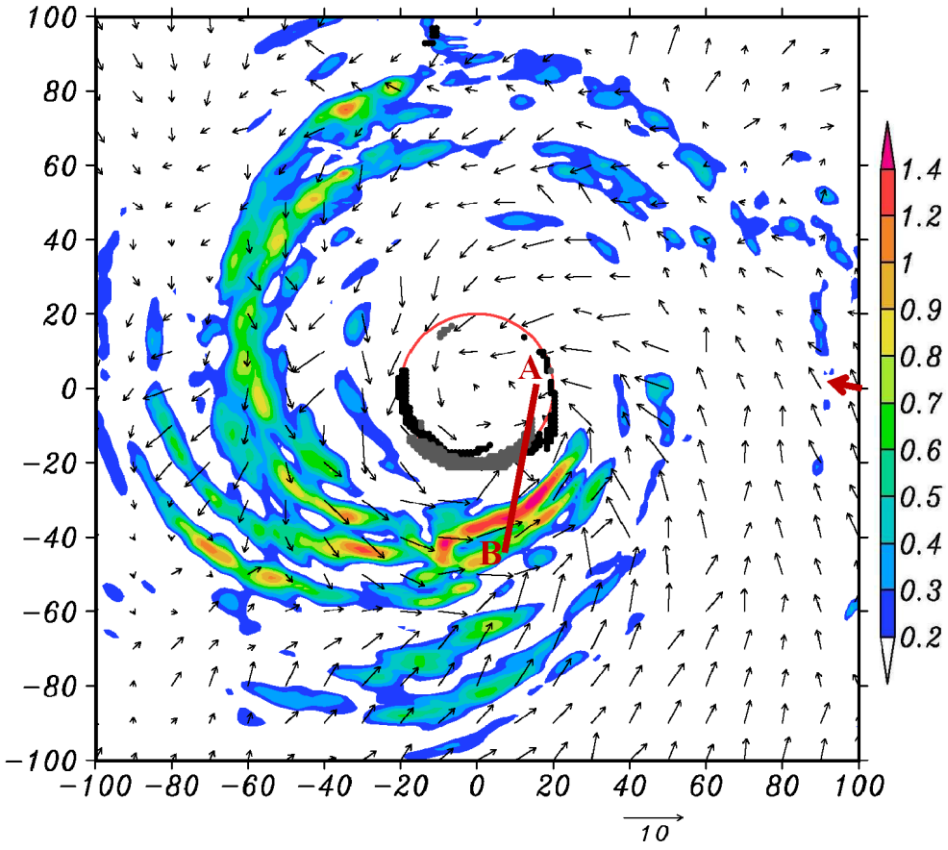


Figure 3.7. Distribution of cloud (ice and snow) hydrometeors (shaded, $10^{-3}$ g $kg^{-1}$), superposed with perturbation horizontal wind vectors, i.e., after removing the subdomain-averaged mean flow of 6 m $s^{-1}$ (denoted by a red arrow) at $z$ =17.5 km from the 30-h prediction. A red circle denotes the radius of maximum wind (RMW) at $z$ = 11 km, and black and grey dots near the RMW indicate the distribution of convective bursts at 30 h, and 30 h 5 min, respectively. Line AB denotes the location of vertical cross section used in Fig. 3.8.

The vertical circulation characteristics of a single CB are given in Figure 3.8, which shows a deep layer of an intense updraft with a width of 10 km, and a peak magnitude of more than 18 m $s^{-1}$ near $z$ = 11 km; its cloud top reaches an altitude of about 18 km. The life time of the CB, traced at $z$ = 11 km from its initiation to dissipation at a nearly vanishing intensity, is about 30 minutes (not shown). Of particular interest is that the CB-induced compensating subsidence, characterized by its peak amplitude of more than 5 m $s^{-1}$ and a depth of more than 10 km is mostly inward, accounting for the downward tilt of isentropic surfaces in the core region. More intense subsidence occurs in the cloud region, suggesting the possible enhanced effects of sublimative cooling of cloud hydrometeors and (long-wave) radiation-cloud interaction, as shown in Liu et al. [1999]; this can also be seen from the general converging flows in the vicinity of the spiral cloud bands. Nevertheless, the CB-induced subsidence in the cloud-free region can be as strong as 2-3 m $s^{-1}$ and extend to z = 19 km. Note also that the CBs occur mostly on the upshear quadrant of the eyewall, even though the VWS is weak (cf. Figures 3 and 1a); these CBs propagate cyclonically in the eyewall at the rates slower with the mean flow. This is consistent with the observational findings of Reasor et al. [2009] for Hurricane Guillermo (1997).

*3.4.3. Development of the upper-level warm core*

Figure 3.9 shows the horizontal distribution of potential temperature ($\theta$, shaded), superposed with the vertical motion and SRF, at 15-minute intervals near the onset of RI, and it is taken at z = 14 km where the upper outflow layer is located. In general, we see a warm core secured inside the RMW, where weak rotational flows

are present, and divergent outflows spreading warmer air outward into the outer region, especially after a more symmetric cyclonic circulation is developed (cf. Figs. 3.9d and 3.3d). Of importance is that more significant warm anomalies associated with CBs appear inside the RMW, with little influence from environmental flow. This

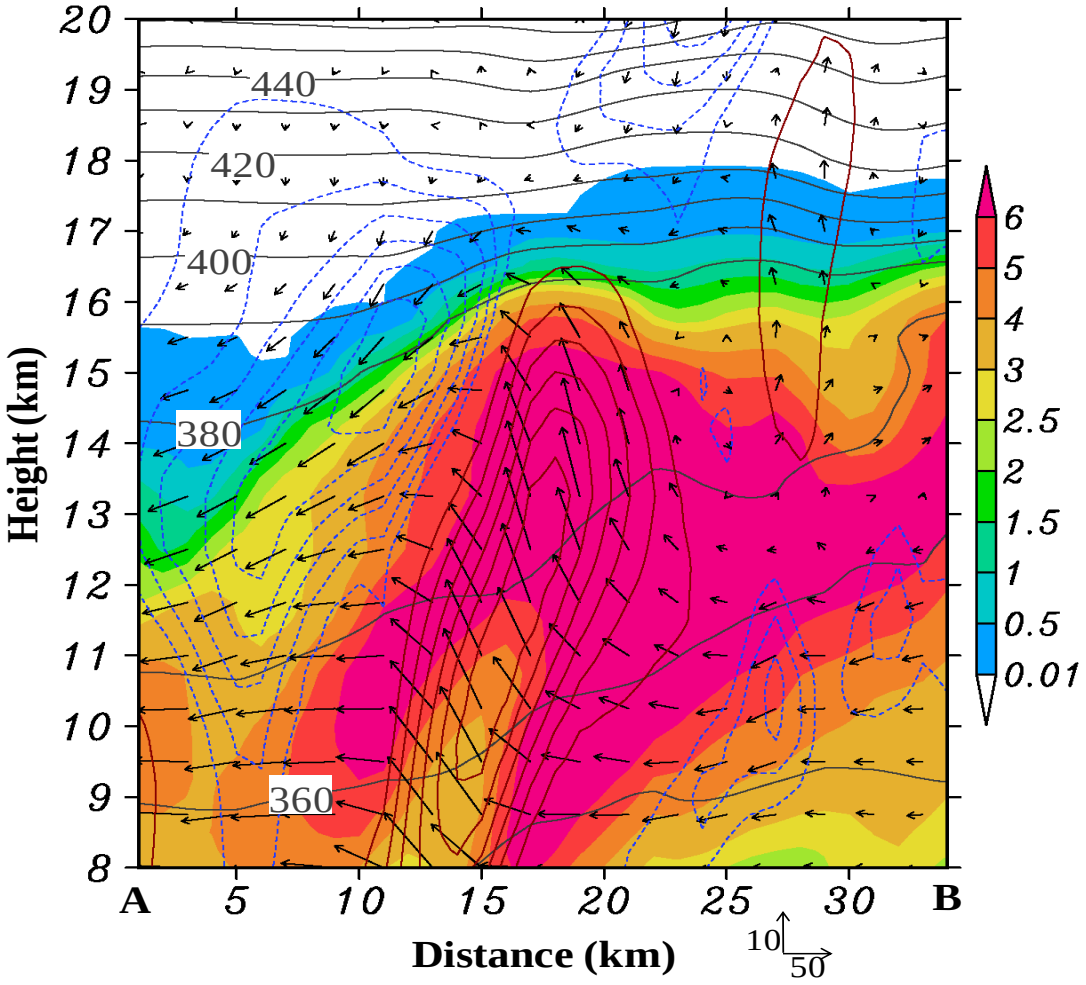


Figure 3.8. Vertical cross section of cloud (ice, snow and graupel) hydrometeors (shaded, g $kg^{-1}$), superposed with in-plane storm-relative flow vectors (see the speed scales at the bottom right, m $s^{-1}$) and vertical motion (downward motion by dashed lines in blue at intervals of 1 m $s^{-1}$ and upward motion by solid lines in red at intervals of 3 m $s^{-1}$) along line AB given in Figure 3. The null vertical motion contour is omitted.

confirms further the important roles of the upper outflow in protecting the warm core from ventilation by environmental flows. At this stage, energy dispersion by gravity waves is much smaller in the core region than that in the outer region and higher up due to large contrasts in static stability (see Figs. 3.1a and 3.2). With little environmental ventilation and energy dispersion, the intensification of the warming core accelerates, e.g., from 4°C near the onset of RI to 20°C at the peak storm intensity, so does the RI of the storm (Fig. 3.1a). We also see from Fig. 3.9 that the compensating subsidence of CBs in the eyewall could produce 6 – 8°C warm anomalies in the eye, which are then cyclonically "advected" downstream by weak rotational flows and low-frequency gravity waves. Figs. 3.9a-d show an example of the evolution of a warm anomaly, denoted by "W," associated with CB C (cf. Figs. 3.9a and 3.5e). It can be traced for a period of 45 minutes, and it is eventually "trapped" in the central calm-flow region of the eye where the mass and wind fields are balanced. Numerical diffusion also appears to help smooth the warm anomalies.

It is of interest to note that some warm anomalies are co-located with CBs in the eyewall (see Figs. 3.9a,b), suggesting that the high-$\theta$ air acts as buoyancy facilitating the upward acceleration of air parcels in the CBs, and it accounts for the generation of some upward motion peaks higher up. Such warm anomalies are relatively short-lived, as they tend to be quickly compensated by adiabatic cooling in the CBs. This can be seen from Figs. 3.9b, c showing that the $\theta \geq 364$ K mass in the eyewall disappears in 15 minutes after the weakening of the associated CBs.

Given the pronounced CB activity and subsidence warming at the early pre-RI stage, why could the upper-level warm core not form until the onset of RI, i.e., 15:00?

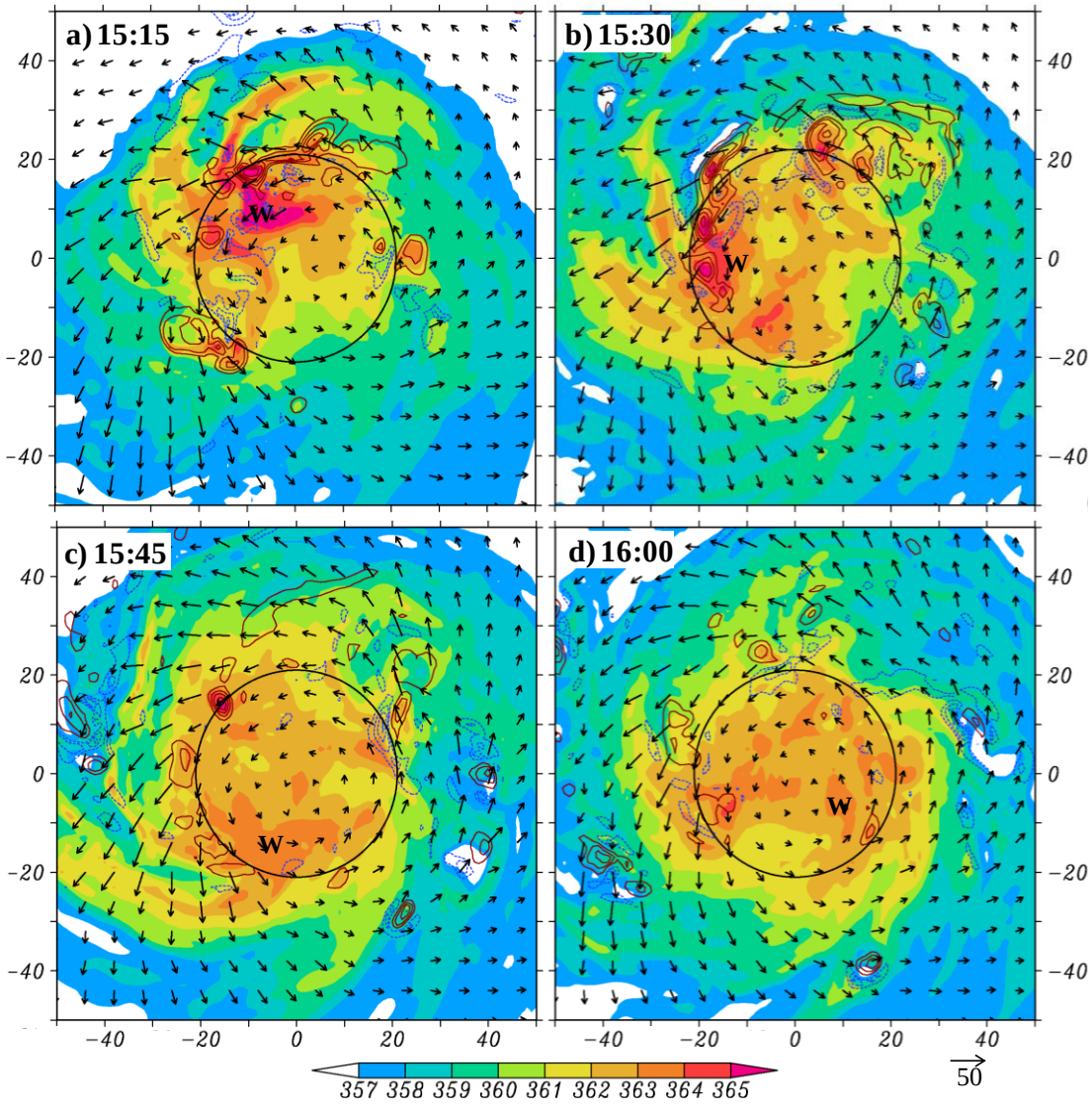


Figure 3.9. Horizontal distribution of potential temperature (shaded) and vertical motion (upward/white solid-contoured at intervals of 5 m $s^{-1}$, downward/black dashed -contoured at intervals of -2 m $s^{-1}$), superposed with storm-relative flow vectors [see the scale beneath the frame (d)], over the subdomains of 80 km × 80 km, centered at $P_{MIN}$, that are taken at 15-minute intervals at z = 14 km during the period of (a) 15:15 to (d) 16:00 (i.e., pre-RI). The mean RMW at z = 1 km is also plotted.

Although we have used Fig. 3.1a to indicate the ventilation effect of environmental flows, Fig. 3.10 reveals that this could be attributed to (i) the absence of a symmetric

outflow layer aloft and (ii) the presence of more pronounced gravity wave activity during pre-RI. Specifically, Fig. 3.10 shows strong divergent outflows emanating from CBs with little cyclonic flows. Most of the subsidence warming produced by the CBs will be advected away into the outer region and dispersed vertically by gravity waves as shown by Fovell et al. (1992). For example, the warm air generated by the CBs in the northern semicircle at 11:25 is advected outward, except in the southeastern quadrant, and dispersed vertically by gravity waves. Thus, only a small amount of the warming, occurring in the eye where static stability becomes small, could contribute to a balanced wind field (cf. Figs. 8a,b). This is in significant contrast to the warming scenario associated with the organized cyclonic flow in the eye after the onset of RI (cf. Figs. 9 and 10). Of course, this by no means implies that the CB-induced warming during pre-RI does not contribute to the subsequent RI of Wilma, but indicates that an increase in the upper-level warm core also requires the generation of a corresponding cyclonic flows, based on the thermal wind relation. Without the establishment of such a balanced flow aloft, most warming air could not be "trapped" in the core region even in the absence of strong VWS or SRFs.

*3.4.4 Detrainment warming vs. balanced warming*

The warm core is a characteristic of mature hurricane, which is determined by the thermal wind balance relationship based on the gradient wind approximation. By examining the basic dynamic and thermodynamic equations, Smith (1980) showed that subsidence is driven by an adverse axial gradient of perturbation pressure which is associated principally with the decay and/or radial spread of the tangential wind field with height at those levels of the cyclone where the tangential winds are

approximately in gradient wind balance. This hypothesis was later corroborated by Emanuel (1995) and Zhang (2000). Using a simple, balanced, axisymmetric model,

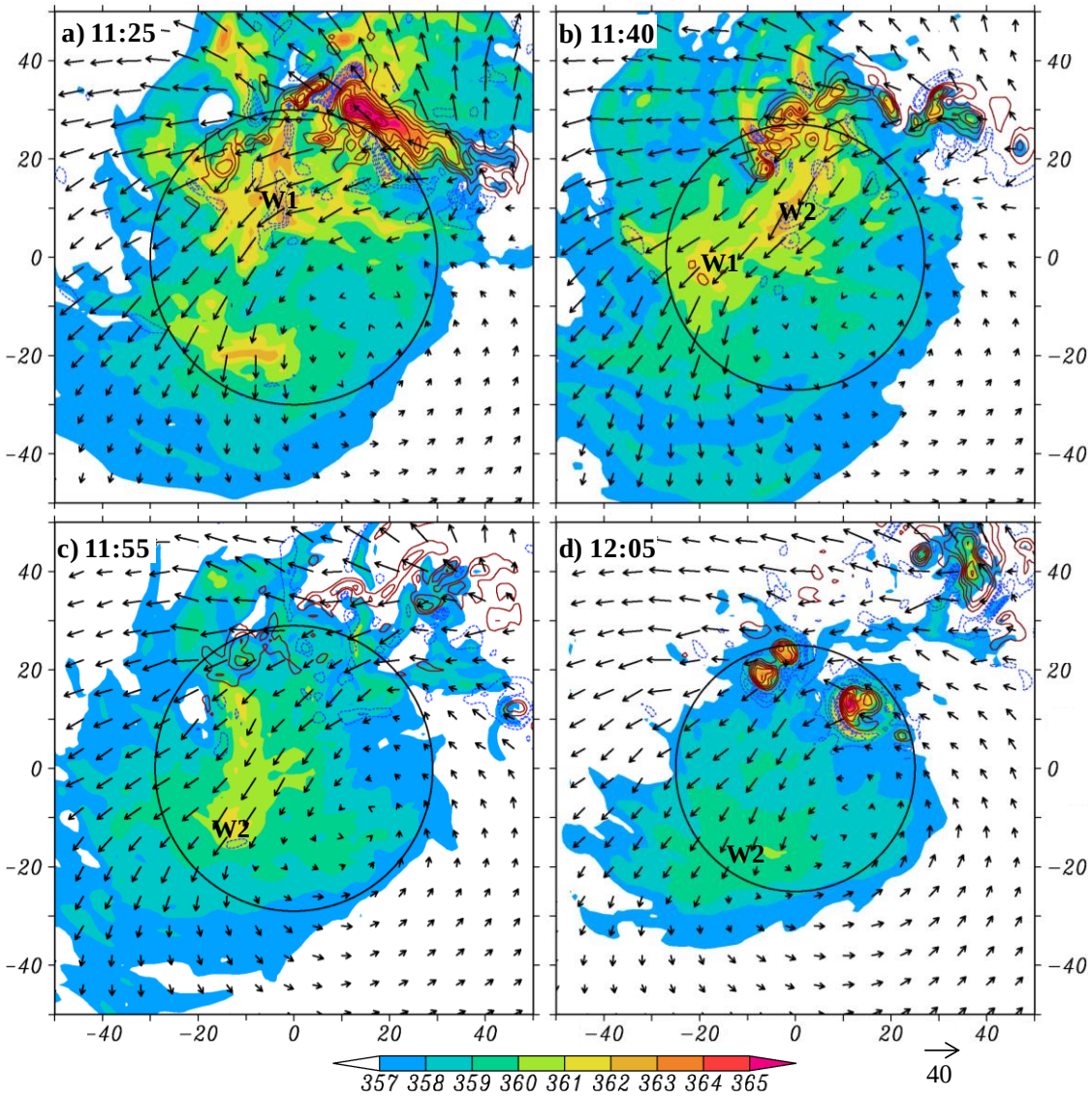


Figure 3.10. As in Fig. 3.9, except for the model integration at (a) 11:25; (b) 11:40; (c) 11:55; and (d) 12:05.

Emanuel(1995) showed that given the swirling velocity of the eyewall, the stead-state eye structure is largely determined. In this sense, the warming has to be in balance with the vertical shear of tangential wind or in another word, the warming is

determined by the vertical structure of tangential wind. But the detrainment warming due to the detrainment of stratospheric air in the wake of convective bursts can't be considered as balanced warming. Therefore, we divide the total warming in the eye into two parts: detrainment warming and balanced warming. Then how much of the upper level warm core is due to the balance warming and how much due to detrainment warming from CBs?

To address this question, let's review Fig. 3.1.We noticed the center of the upper level warm core is located at 12 km in pre-RI stage and post RI stage and at 14 km in RI stage. The substantial detrainment warming in pre-RI stage can't accumulate in the hurricane eye because of strong advection across the eye and high frequency of gravity waves that dissipate the warming, as mentioned in section 3.3.3. In the post-RI stage the convective bursts are almost absent and therefore will not contribute to the warming in the eye. The warming in these two stages has to come from the balanced warming. In contrast, the detrainment warming due to convective bursts in RI stage makes a great contribution to the surface pressure fall and this drastic detrainment warming is accompanied by the rapid climbing of the upper boundary of the upper level warm core from 14 km to 18 km. It's this 4-km layer of detrainment warming above 14-km altitude that accounts for the record RI of Hurricane Wilma and hence the convective bursts play a critical role in determining the RI rate. Is the convective bursts activity in pre-RI stage more important than that in RI stage? If we only look at the detrainment warming, it certainly is. However, the convective bursts play an important role in bring the storm structure from asymmetric to axisymmetric by stretching the vorticity exponentially at low level that the

detrainment warming in RI stage at upper level can accumulate and contribute to the surface pressure fall. Although we part the warming into detrainment warming and balanced warming, these two warming interact nonlinearly. For a given balanced vortex with a warm core, the detrainment warming that's added at upper level will induce surface pressure instantaneously. The winds have to increase to adjust to the new surface pressure that's caused by both warming. The increased winds and strengthened upper level warm core can impact the convective bursts both in positive and negative ways. In one hand, the equivalent potential temperature will increase because of increased sea-to-air moisture flux due to the increased winds and favor the convective bursts reaching high altitudes and produce detrainment warming at higher level. On the other hand, the upper level warming will increase the convective stability and suppress the convection. Apparently, there is a nonlinear interaction between the detrainment warming, balanced warming, and intensity and is a very complicated issue. In this study, we are not trying to quantify the separate contribution of these two warming but just emphasize the great importance of detrainment warming due to convective bursts in determined the record RI rate.

### *3.6. Convective bursts and sea-surface temperature*

As mentioned in section 3.1, previous studies have found that the RI of TCs is associated with warm SSTs and active CBs. However, little has been discussed in the literature about their relationship. In this section, we will show that CB activity depends critically on the warmth of SSTs, thereby determining the RI rate of Wilma. To this end, a sensitivity simulation is conducted (hereafter SST-1), in which SSTs in a control simulation are reduced by 1°C at every ocean point. This control simulation

is defined herein as the one in which a triply-nested (18/6/2 km) grid configuration with 38 vertical levels is adopted (hereafter CTL), while all the other parameters are held identical to the 72-h prediction presented in Chen et al. (2011) (hereafter HRES). Despite this reduction, SSTs in the area of interest are still in the range of 28 - 29°C. We adopt this coarser grid configuration, because of the limited computing power for numerous sensitivity simulations to be conducted, in addition to SSTs. Thus, we need to compare first the CTL to the HRES results before discussing the sensitivity of the modeled RI and CBs to SSTs.

The CTL-simulated time-height cross section of perturbation temperatures ($T'$), θ, and time series of $P_{MIN}$ are given in Figs. 9a and 9c, showing that the time evolution and structures of these variables are generally similar to those shown in Figs. 1a,b from the 1-km resolution run, except for their amplitudes. That is, as expected, the use of the finest grid size of 2 km produces a deepening rate of 3.5 hPa $hr^{-1}$ during the period of 16 – 35 h with $P_{MIN}$ = 906 hPa. The final 72-h intensity is only about 5 hPa weaker than the HRES storm. The modeled track of the CTL storm, as well as the SST-1 storm, is also close to the HRES-predicted (not shown). Although the peak intensity of the CTL storm is 17 hPa weaker than the HRES storm, its deepening rate still doubles the minimum threshold for an RI storm. In particular, the CTL simulation reproduces reasonably well the timing of the onset, and of reaching the peak intensity and weakening stages as well as the ERC of the HRES storm. In addition, the CTL simulation reproduces the maximum warming of 16°C at z = 14 km near 36:00, with the pronounced downward displacement of isentropic surfaces during RI, and the subsequent lower elevation of the warming core. All these

indicate that the 2-km resolution CTL simulation can be used to examine the sensitivity of the modeled storm intensity to various physical processes.

Figures 3.11a-c compare the time-height distribution of the warming core and the time series of $P_{MIN}$ between the SST-1 and the CTL runs. We see only slight variations in $P_{MIN}$, and warming-core intensity and structures during the first 18 h, but large differences during the second 18 h and the remaining period between the two runs. The SST-1 storm exhibits a deepening rate of 1.9 hPa $hr^{-1}$ during the period of 18 – 38 h, with $P_{MIN}$ = 936 hPa at 38:00. Although this deepening rate still qualifies it as an RI storm, its peak intensity is 30 hPa weaker than the CTL storm. More significantly, the SST-1 storm does not exhibit a period of sharp weakening, like that shown in CTL and HRES, after reaching the peak intensity. Of particular relevance is that the upper-level peak warming core is about 6°C weaker, and located 1-2 km lower than that of the CTL storm (cf. Figs. 3.11a,b). Both the weaker warm core intensity and the lower elevation are consistent with the much less descent of the stratospheric air (and weaker $P_{MIN}$ as well).

Clearly, the above results are not surprising, based on the wind-induced surface heat exchange (WISHE) theory that was first discussed by Ooyama (1969), and later clarified by Emanuel (1986, 1991), and Rotunno and Emanuel (1987). However, the WISHE theory does not relate the roles of SSTs in RI to the efficiency of the upper-level warm core. Fig. 3.12, comparing the statistical characteristics of CB-elements

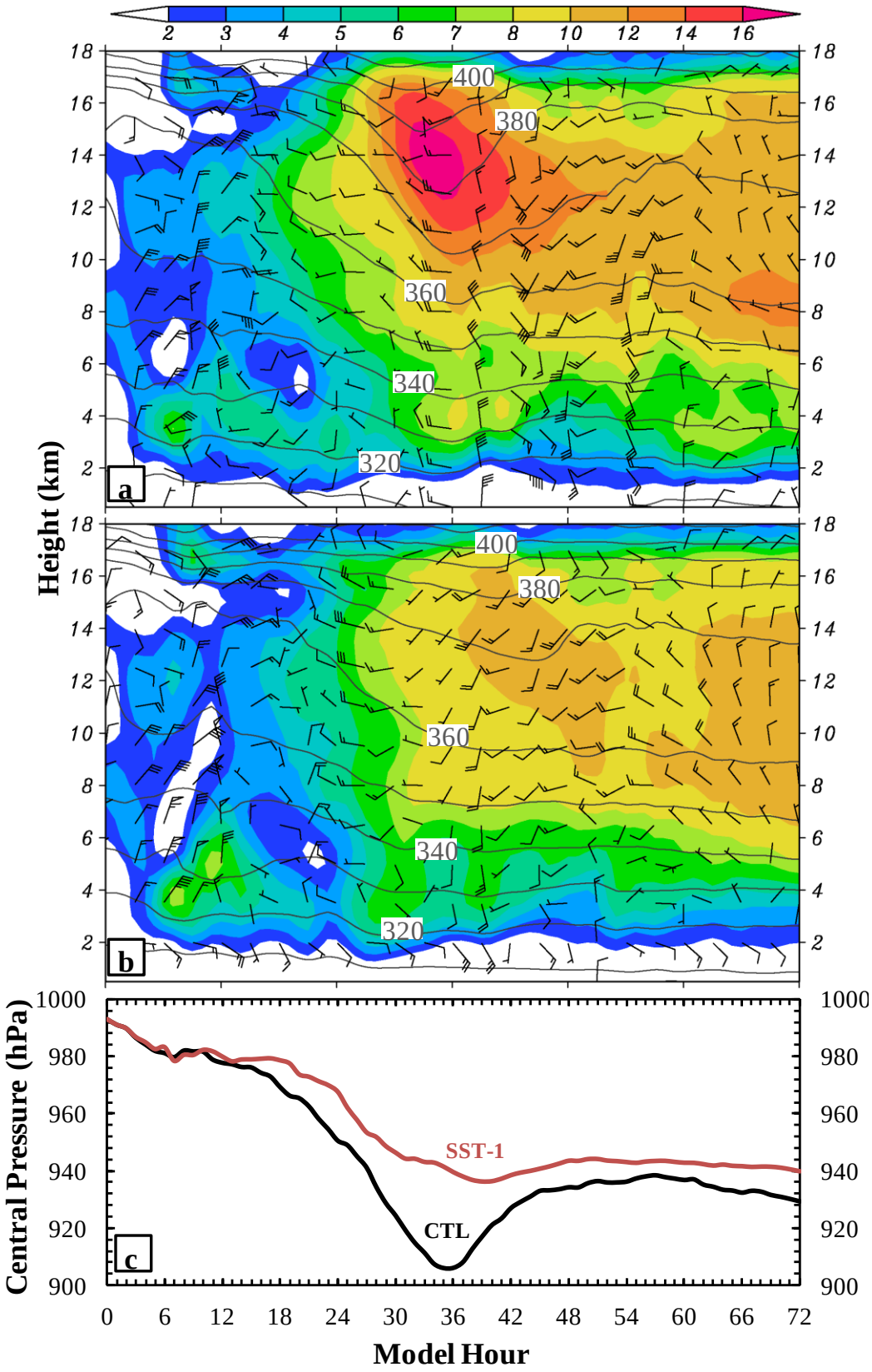
2 3 4 5 6 7 8 10 12 14 16
Height (km)
400
380
360
340
320
a
b
Central Pressure (hPa)
SST-1
CTL
c
Model Hour

Figure 3.11. As in Fig. 3.1a, except from the 72-h triply nested (18/6/2 km) grid simulation with the finest 2-km horizontal resolution and 38 vertical levels, which is associated with (a) the control (CTL) run; and (b) the 1°C colder SSTs (SST-1) run. (c) As in Fig. 3.1b, except for the CTL (solid) and SST-1 (dashed) runs.

between CTL and SST-1, shows the importance of CBs in relating SSTs to the upper-level warm core and RI of Wilma. Specifically, on average, there are 20 – 25 gridcolumns (or an equivalence of 80 – 100 $km^2$) of CB-elements occurring during the 24-36 h RI stage in the CTL run; its area coverage is about 20% less than that in the HRES run (cf. Figs. 3.12a and 3.4a). However, with the colder SSTs specified, there are much fewer CB-elements or merely a couple of CB-elements at most times developed during the RI stage, and no CB activity occurs afterwards (Fig. 3.12b). The isentropic surfaces in the lower stratosphere descend little downward, in contrast to those in the upper troposphere (e.g., the $\theta$ = 380 K vs. $\theta$ = 360 K surface). This conforms to the generation of a weak upper-level warming core (Fig. 3.11b). It follows that colder SSTs tend to reduce convective instability and CAPE, allowing less deep convection to penetrate into the lower stratosphere.

One may note, however, that like those in the CTL, there are still many CB-elements occurring in the SST-1 run during pre-RI (cf. Figs. 3.12a and 3.12b). This is apparently caused by the preexistence of high CAPE in the model initial conditions, especially in the bogussed vortex, as mentioned before, so the impact of the specified colder SSTs is delayed for about 20 h. Ideally, the SST-1 run should be initialized 24 h earlier, i.e., at 0000 UTC 17 October, which would allow the model atmosphere to

be reasonably adjusted for the specified colder SSTs. We may speculate that this procedure would result in a further weakened storm. Nevertheless, this result confirms our earlier findings that most CB-induced warming at the earlier stages tends to be propagated away from the inner-core region by high-frequency gravity waves, in addition to the ventilation effects of SRFs. In this regard, the CB-induced subsidence warming in the CTL and HRES storms appears to contribute more efficiently to the upper-level warm core after a balanced upper cyclonic circulation is established near the onset of RI.

### *3.7. Chapter summary*

In this study, the importance of the upper-level warming core and flow structures, CBs, and warm SSTs in the RI of TCs is examined using a 72-h nested-grid, cloud-permitting prediction of Hurricane Wilma (2005) with the finest grid sizes of 1-2 km. Results show that an upper-level warming core forms, in coincidence with the onset of RI, as a result of the descent of stratospheric air in the presence of weak SRFs aloft. An isentropic analysis of the eye air reveals more than 7-km descent of the stratospheric air, producing a warming core of more than 20°C at the peak storm intensity that is located in the same layer as the upper outflow. It is found that the descent of stratospheric air results from the upper-level detrainment of CBs occurring inside the low-level RMW where higher-$\theta_e$ air is located. The associated subsidence warming does not become effective until an organized upper-level outflow is established with a weak cyclonic circulation in the eye. Because of mass continuity, a thin cyclonic radial inflow layer, located above the upper-level outflow layer, is induced by the mass sink and lower pressure in the eye. This inflow air can be

isentropically traced to the peak warming core inside the upper-level outflow layer. These results confirm our hypothesis that a strong divergent outflow in the outer region helps protect the warm core from ventilation by environmental flows. The higher altitude the upper-level warming core is located, the more hydrostatically efficient it is to sea-level pressure falls. The importance of the upper-level warming core in RI is consistent with the eyewall thermodynamics of MPI. In the present

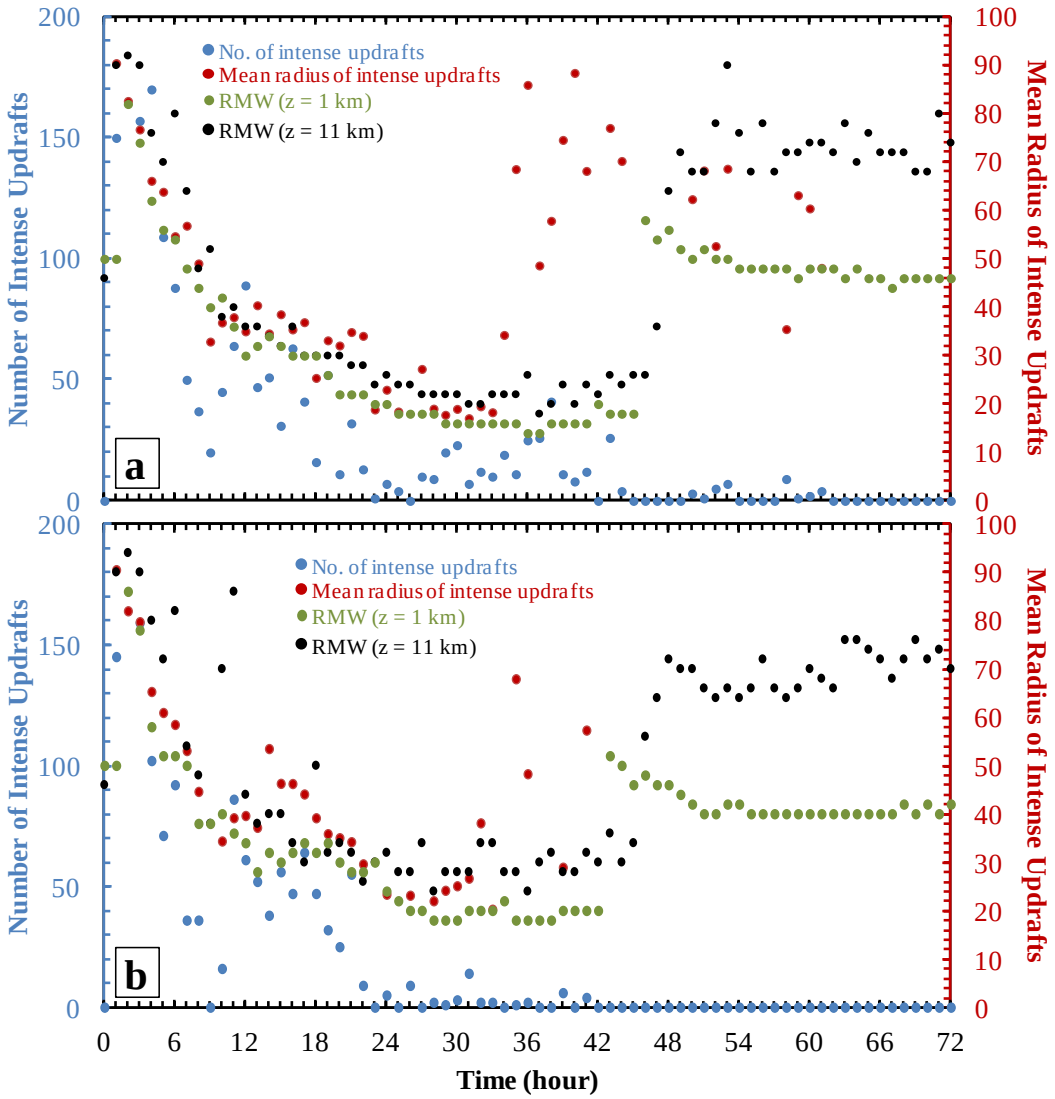


Figure 3.12. As in Fig. 4a, except for (a) the control (CTL) run; and (b) the 1°C colder SSTs (SST-1) run at the 60-min resolution.

case the high altitude of the warming core also benefits from the presence of a high tropopause.

It is shown that CBs, characterized with a radial scale of about 10 km and an azimuthal scale of 10-20 km, have peak updrafts and rainfall contents reaching as high as 11-15 km altitude that are typically flanked by intense subsidence and divergent outflows aloft. It is found that more CBs take place in the inner-core regions prior to the onset of RI, and that their area coverage decreases rapidly as the storm contracts, and reaches a stable level during RI. Results indicate that most of the CB-induced subsidence warming during pre-RI tends to be propagated away by large SRFs and higher-frequency gravity waves, and that it appears to contribute more efficiently to the upper-level warm core after a balanced upper cyclonic circulation is established near the onset of RI. The intensification of the warm core accelerates, leading to the RI of the storm. It is also shown that considerable CB activity could still occur in the outer eyewall as the storm weakens rapidly as a result of the ERC, suggesting that CBs also play an important role in the contraction of the outer eyewall and the subsequent intensification of the storm through the generation of another upper-level warming core.

The relationship between the development of CBs and the warmth of SSTs is examined through the sensitivity simulations of reduced SSTs. Results show that the use of 1°C colder SSTs as the bottom boundary condition results in the development of much fewer CBs during RI, and the generation of a lower-elevated and much weaker warming core, with little descent of the stratospheric air. As a result, the model produces a storm that is more than 30 hPa weaker than the control storm. This

result suggests that the RI of TCs is determined by SSTs (and other favorable environmental conditions) through the WISHE process and the active development of CBs in the inner-core region that can penetrate into high altitudes. Thus, we may conclude that significant CB activity in the inner-core region is an important ingredient in generating an intense upper-level warm core that is hydrostatically more efficient to the RI of TCs, given all the other favorable environmental conditions. Based on the above results, we recommend that more attention should be paid to the upper tropospheric flows, rather than just VWS in the typical 850-200 hPa layer, in order to reasonably predict the RI of TCs.

# Chapter 4. Eyewall contraction and a small eye size

## *4.1 Introduction*

The intensification of hurricanes has been observed to be always accompanied by eyewall contraction, which can be categorized into two different processes: asymmetric contraction and symmetric contraction. In these two processes, the symmetric contraction has been relatively well addressed in the literature.

Shaprio and Willoughby (1982) applied Eliassen's (1951) model of forced secondary circulation to tropical cyclones and concluded that the height of standard isobaric surfaces fell rapidly inside the radius of maximum wind (RMW) and much more slowly outside it in response to a heat or a momentum source near an RMW, leading to the contraction of the RMW and the eyewall.

In contrast, asymmetric contraction remains an open issue. Some studies (Montgomery and Kallenbach 1997; Moller and Montgomery 1999; Shapiro 2000) showed that asymmetric moist convection can intensify the axisymmetric primary circulation through momentum transports by vortex Rossby waves. However, Nolan and Grasso (2003) and Nolan et al. (2007) have recently demonstrated purely asymmetric heat sources cause vortex weakening. Moller and Shapiro (2005) points out that the small eddy kick created by the additional diabatic heating asymmetry leads to a substantially amplified long-term change in the azimuthally averaged vortex, with episodes of strong relative weakening and strengthening following at irregular interval.

Kossin and Schubert (2001), hereafter KS2001, showed that the hurricane vortex may experience drastic pressure falls when the mesovortex migrates into the

eye by examining the two-dimensional barotropic evolution of thin annular rings of enhanced vorticity embedded in nearly irrotational flow. The sudden pressure drop due to this process has also been observed in our sensitivity tests, where 8 hP $hr^{-1}$ drop is produced. However, the sudden pressure drop by the mesovortex is not sustainable since it requires the constant inward migration of mesovortices to maintain this deepening rate. The inertial stability in the hurricane eye is very large, which prevents the radial displacement of any kind. The inward migration of mesovortices is considered as a chaotic behavior in KS2001 and they did not explain when and why it happens.

Recently, Harnos and Nesbitt (2011) showed majority of the RI cases bear a symmetric eyewall prior to the RI onset by analyzing the microwave remote sensing of tropical cyclones undergoing RI. This indicates that symmetric contraction accounts for RI at a great extent. Then, what is the role of asymmetric contraction? What is the physical mechanisms by which symmetric contraction is favorable for RI? The threshold value for a storm to qualify RI is 1.75 hPa $hr^{-1}$ but the deepening rate can be as large as 9 hPa $hr^{-1}$ for 6 consecutive hours, such as Hurricane Wilma (2005). What determines the drastically different deepening rate?

Some of the questions have been addressed in chapter 3. As mentioned therein, the subsidence warming cannot be retained in the eye until the storm-relative wind at the eye center in the outflow layer reaches very small value. A further examination reveals that the timing of weak storm-relative flow coincides with a vertically coherent storm structure and horizontal symmetric pattern with a fully closed circular eyewall, before which most of subsidence-induced warming is

propagated away by internal gravity waves and advected away by strong storm-relative flow in the eye. The eyewall closure corresponds to the time when storm-relative flows in the eye become weak and the upper level becomes more balanced and hence internal gravity wave activity is less. This prompts a hypothesis that a horizontally symmetric eyewall and a vertically coherent structure, which are linked internally, could account for the trigger of the RI process. The vertically coherent structure favoring RI can be understood purely from the hydrostatic point of view. The surface pressure measures the weight of air mass throughout a vertical column. Any displacement from a vertically coherent structure will weaken the surface pressure. Weak vertical wind shear is one factor that prevents the storm from being ventilated. Many studies showed the evolution from tilting to vertically coherent structure serves as a trigger for the genesis and intensification. The numerical simulation of Typhoon Chanchu (Hogsett and Zhang 2010) showed that the genesis starts when the middle level vortex and low-level vortex becomes collocated and a vertically coherent warm core develops.

Although many storms bear a horizontally symmetric eyewall and vertically coherent structure but Wilma set the record intensity of 882 hPa in the Atlantic basin and intensification rate of 9 hPa $hr^{-1}$ for 6 hours. Apparently these two factors we mentioned will not be the only reason that accounts for RI. Then, what kind of structures distinguishes Hurricane Wilma from the other storms that also underwent RI but at less intensification rate?

Gary (1986) pointed out that the area-averaged precipitation of hurricanes does not differ much from those of other tropical disturbances but the horizontal

distribution of hurricanes can distinguish themselves from the other less organized tropical weather systems. Early studies (Schubert and Hack 1982, Hack and Schubert 1986) showed that the diabatic heating is more efficient in spinning up a tropical storm if the RMW is smaller. The numerical results from Hack and Schubert (1986) (Fig. 1 and Fig. 2) indicate a nonlinear relationship between the contraction of the RMW and the storm intensification, that is, the storm intensifies much faster for a given contraction speed when the RMW is smaller. This early study pinpoints another factor that accounts for the record intensification rate of Wilma: the small size. Namely, the 5—km diameter eye of Hurricane Wilma is the smallest one ever known to HRD staff (Pasch et al. 2006). Hurricane Charley (2004), which also has a very small eye, experienced 33 hPa drop in central pressure in three hours but weakened quickly after landfall. Kieu et al. (2010) studied the pressure and wind relationship associated with Wilma, and their study indicates the importance of including the size of the RMW in estimating TC intensity changes. Combining the two factors — the small eye size and a symmetric eyewall, a more complete picture about the RI of Hurricane Wilma can be painted: the onset of RI corresponds to a formation of a full eyewall whose size is very small and this is indeed what we observed from the model results.

How does the small eye surrounded by a symmetric eyewall form in this case? What does the storm structure look like? Fig. 2.11 shows the component of symmetric contraction in 72-h prediction from the perspective of azimuthally averaged radar reflectivity and tangential wind. Results reveal a substantially faster contraction speed in pre-RI stage, especially in the first 6 hours. In contrast, the

eyewall contraction is much slower during the RI stage. As mentioned in chapters 2 and 3, the eyewall is asymmetric in the pre-RI stage and becomes closed at the onset of RI. This means that the asymmetric contraction processes produce much faster contraction compared to symmetric contraction processes.

In this chapter, we will address the eyewall contraction and the associated storm structure. Section 4.2 describes the spin-up process in the first 6 hours which accounts for 50-km contraction. Section 4.3 shows how the asymmetric contraction takes place. Section 4.4 shows the evolution of thermally indirect circulation in the eye associated with the eyewall contraction. Section 4.5 explains the importance of small eye size in determining intensification rate. Section 4.6 shows the byproduct of asymmetric eyewall contraction — trochoidal oscillation. The chapter conclusion is given in the final section.

### *4.2 Spin up of a bogus vortex*

Figure 4.1 shows that the radius of maximum wind is located around 45 km while the maximum inflow is located around 110 km at the model initial time. The relative vorticity profile, which is mostly determined by the tangential wind, shows a monopole pattern with almost constant maximum between the center and 20-km radius, implying the solid body rotation inside 20-km radius. The vorticity decreases outward rapidly to about 60-km radius. Outside 60-km radius is another monopole associated with the second tangential wind maximum near radius 90 km. The divergence profile, which is determined by the radial flow, shows the maximum convergence around 90-km radius. This configuration of tangential wind and radial

wind in the initial condition leads to a quick adjustment that accounts for the drastic contraction in the first 6 hours.

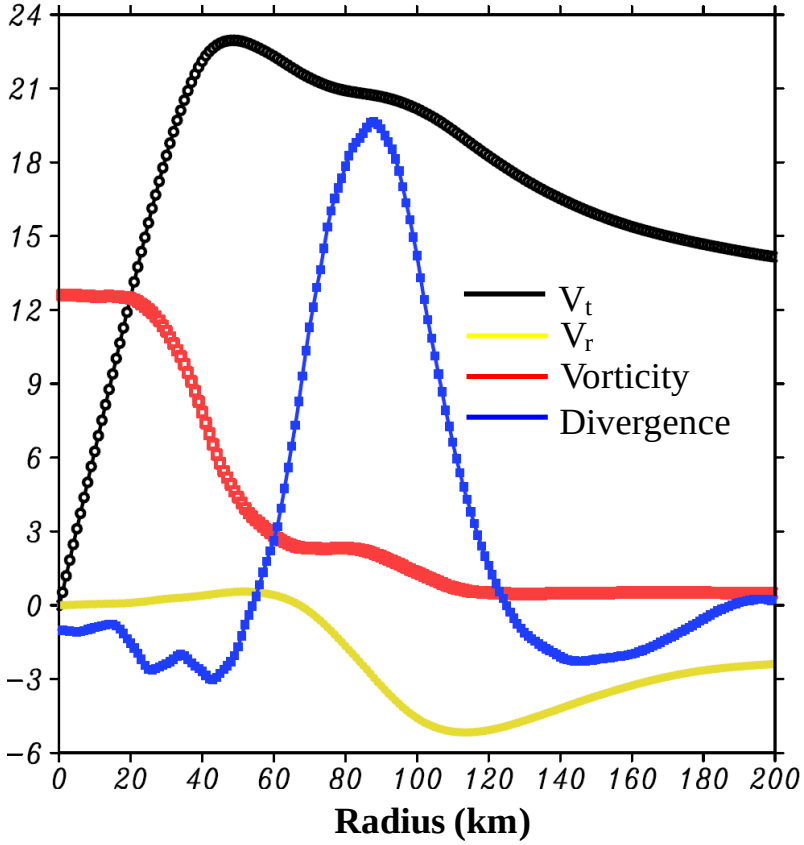


Figure 4.1: Radial profiles of the tangential wind (black line), radial wind (yellow line), relative vorticity (red line) and divergence (blue line) at z = 1 km at the model initial time. The unit is m $s^{-1}$ for the tangential wind and radial wind, $10^{-4}$ $s^{-1}$ for vorticity and $10^{-5}$ $s^{-1}$ for divergence. The sign of divergence is reversed in the plot and the positive value means convergence.

Fig. 4.2 shows the spin-up of the tangential winds over the first 3-h period at different levels and different radii. As can be seen, the tangential winds near the initial RMW and the initial maximum convergence both intensify near the surface (z = 100 m) with the tangential winds near the initial RMW showing more fluctuations. In contrast, the tangential winds at the midlevel (i.e., z= 8 km) show a very different

response. The tangential wind near the initial RMW intensified for about 45 minutes and weakens quickly while the tangential wind near the initial maximum convergence keeps increasing. The two different responses at the low and upper levels reveal the

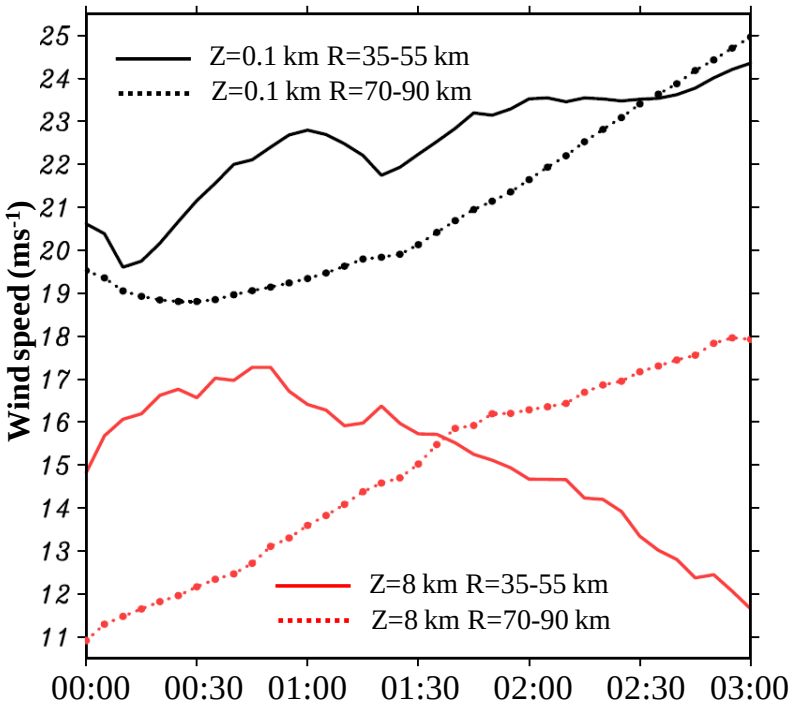


Figure 4.2: Time series of wind speeds averaged over rings between r = 35 - 55 km (solid lines) and between r = 70 - 90 km (dashed lines) at z = 0.1 km (black lines) and z = 8 km (red lines).

two different roles: conditional instability of the second kind (CISK) and wind-induced surface heat exchange (WISHE). WISHE, although important, can only spin up the wind field near the surface without the enhancement of secondary circulation. It can be inferred that the vertical motion associated with the inner wind maximum is much weaker than that associated with the outer wind maximum, which is confirmed in Fig. 4.3. As we can see here at 01:00 that the vertical motion associated with the inner wind maximum is not only weak but also much shallower, only confined to the boundary layer. In contrast, the vertical motion associated with the outer wind

maximum is not only much stronger but also penetrates to the much higher level with the maximum vertical motion located around 11-km height. This shallow secondary circulation associated with the inner wind maximum is attributable to the lack of diabatic heating which tends to promote the secondary circulation caused by the frictional convergence to a much higher level than it would be without diabatic heating, as described in Willoughby (1979).

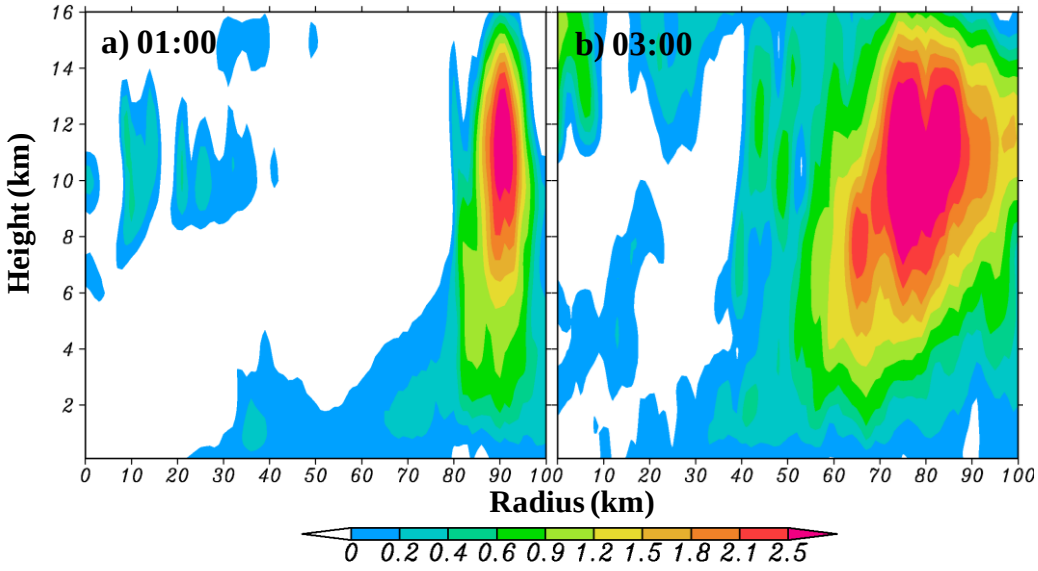


Figure 4.3: Radius-height cross section of azimuthally averaged vertical motion at a) 01:00 and b) 03:00.

In the presence of strong convergence outside the inner maximum wind, moisture in the boundary layer inflow will be blocked. In this sense, the wind field configuration in the initial condition resembles the situation in the double eyewall that approaches the end of the ERC. At 03:00, the outer vertical motion grows both in width and magnitude while contracting by 15 km. The upright feature also evolves into a slight slantwise fashion. From the above analysis, it seems that the convergence, which is determined by the radial wind, is more important than the

tangential wind. However, the rotational part is also important. Basically, the tangential and radial winds determine the balanced, rotation part and unbalanced, divergence part of the flow field, respectively. The secondary circulation only arises from the unbalanced part. In the unstable state, the unbalance part manifest as vertical motion to release the instability and in the stable state, the unbalance part takes the form of gravity wave. Usually gravity waves are not considered as important in the mesoscale and synoptic scale of atmospheric phenomena.

A recent paper of Nascimento and Droegemeier (2006) explores the dynamics of adjustment in deep convective storms by altering the horizontal velocity and vertical velocity in the initial condition. Their results show that the structural change of horizontal winds in the initial condition plays a significant role in the storm evolution while the change in the vertical motion field has no impact on the storm evolution. This result is not surprising since the vertical motion is determined by the distribution of the horizontal velocity and the vertical motion can quickly restore anytime after the reset.

### *4.3 Asymmetric contraction*

Before addressing the asymmetric contraction, we first take a look at why the storm shows an asymmetric pattern in the pre-RI stage. In chapters 2 and 3, we mentioned that the moderate shear and midlevel dry intrusion may be responsible for the partial eyewall that opens to the west. Next, we will show if these two factors contribute to the asymmetry of the eyewall convection in the present case.

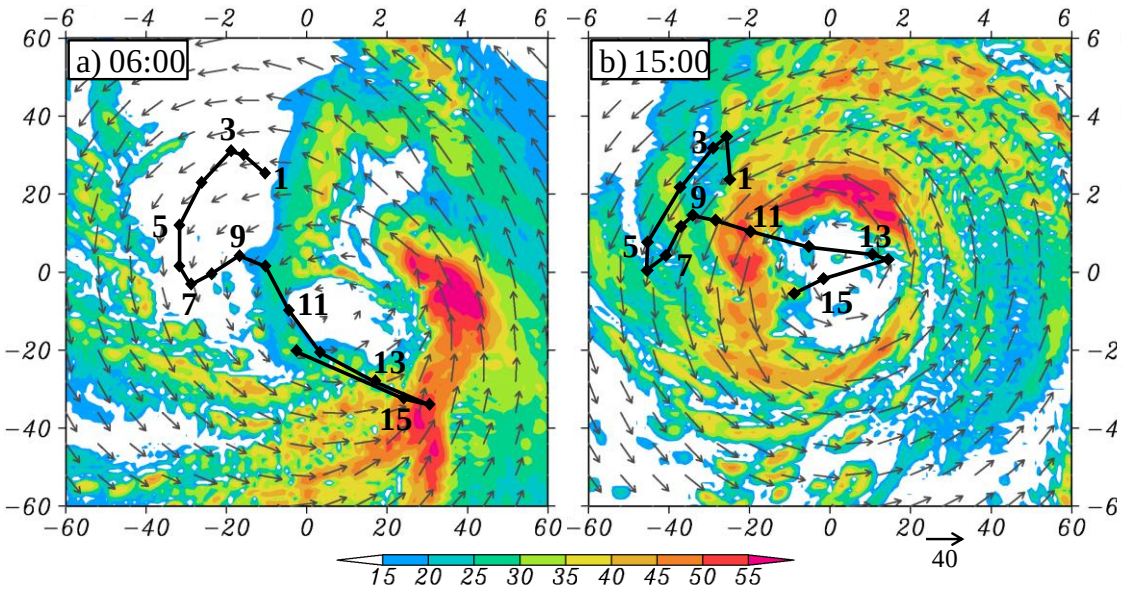


Figure 4.4. Horizontal distribution of radar reflectivity (shaded) and storm-relative flow vectors at 1-km altitude at a) 06:00 and b) 15:00. Hodographs with vertical shear vectors (solid) between 1 and 16 km, obtained by averaging them over an area of 1000 km x 1000 km surrounding the storm center, are sketched with the speed scale given on the top and right frames.

*4.3.1 Why is the asymmetric contraction important in RI?*

Many early studies have addressed the impact of VWS on the storm structure, track, and intensity. The overall detrimental effect of VWS on the storm structure has been explained as the "ventilation" effect (Gray 1968) in which the upper-level warm air is advected away from the inner-core region. In addition to this "ventilation" effect, more recent studies (Bender 1997; Frank and Ritchie 1999, 2001, 2002; Smith et al. 2000) showed that VWS produces asymmetry in the vertical motion and rainfall fields by inducing upward motion in the downshear left quadrant and downward motion in the upshear quadrant.

Fig. 4.4 shows the horizontal distribution of radar reflectivity and SRF at 1-km altitude at 06:00 (pre-RI stage) and 15:00 (RI onset). Hodographs in the figure indicate that the VWS between 3 km and 14 km represents the overall shear relatively well, which is equivalent to 700 - 100 hPa VWS. This is different from the traditional 850 hPa - 200 hPa VWS. This is because Hurricane Wilma is a very deep storm with an usually high-altitude outflow layer and warm core, as discussed in chapter 3. At 06:00, precipitation is concentrated in the downshear region and the flow fields take on an elliptical shape with the major axis parallel to the VWS. The circulation center is close to deep convection in the downshear region. At the onset of RI, VWS decreases and both radar reflectivity and flow fields take on a circular shape. Despite the overall symmetry, deep convection is still favored in the downshear left quadrant.

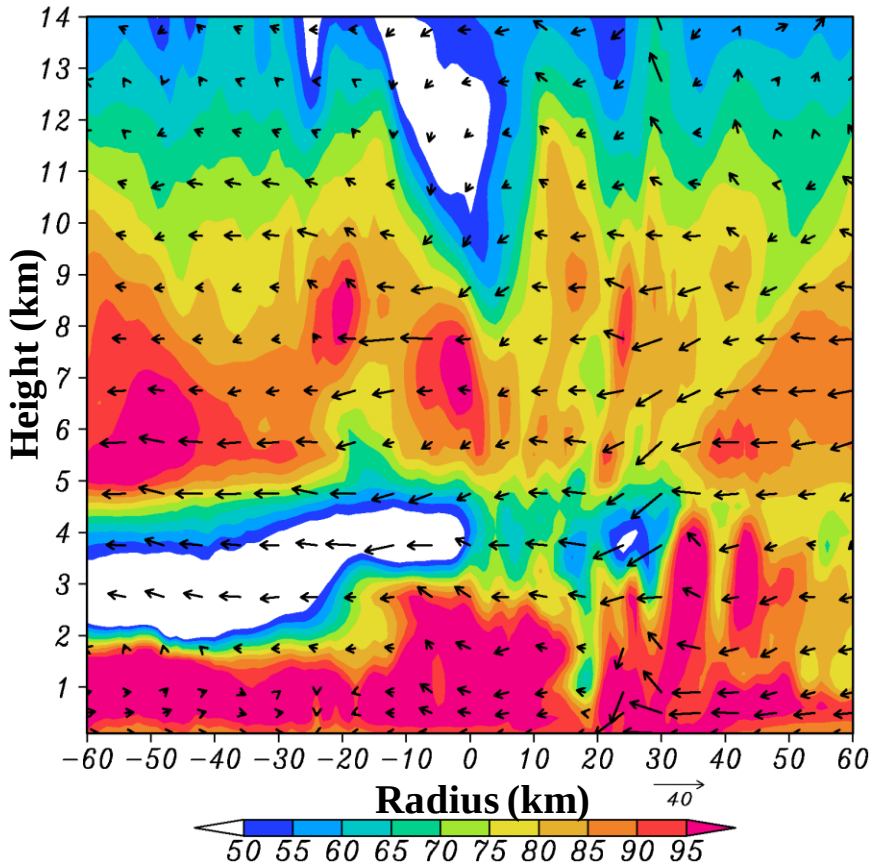

Figure 4.5. West-east cross section of the relative humidity (shadings) and SRF vectors in the eye at 06:00. The vertical motion is multiplied by 5.

Fig. 4.5 shows the west-east vertical cross section of the relative humidity and SRF vectors in the eye at 06:00. It is clear that the absence of deep convection to the west of the storm center is due to the presence of dry air in the middle level. However, the SRFs indicate that the dry air does not originate from the environment in the midlevel. A further examination reveals that the dry air results from the descending motion that initiates at 10-km altitude, which is caused by the VWS. This clarifies that VWS is the sole reason that accounts for the asymmetry in the pre-RI stage.

The horizontal asymmetry induced by VWS has a significant impact on the vertical structure of the storm. Deep convection concentrated in the downshear region will draw the circulation center toward this region and produce a vertical tilt, which has been shown in Hogsett and Zhang (2010) but the tilt is much more significant in their study. Fig. 4.6 shows that despite the compactness of the storm, the horizontal asymmetry induced tilt can be as large as 30 km with the 5-km circulation center being displaced downshear. The displacement reaches a small value around the onset of RI and remains small till the end of the 72-h model integration. This vertical tilt certainly has a negative impact on the storm intensity and is one major reason that symmetric eyewall favors intensification.

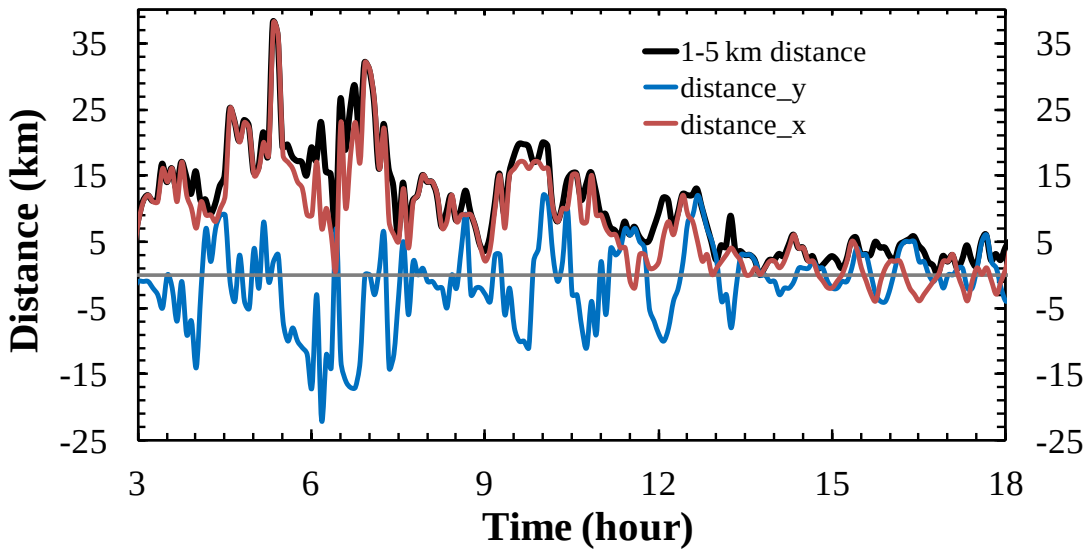


Figure 4.6: Time series of displacement of circulation centers between 1 km and 5 km (black line), the zonal component of the displacement (red line) and meridional component (blue line).

*4.3.2 Formation of new rainbands*

One interesting phenomena observed in the asymmetric contraction is the formation of new bands inside the eyewall, which accounts for the fast contraction in the pre-RI stage. Fig. 4.7 shows the evolution of new bands formation. At 07:00, the partial eyewall A is located at the downshear region while there is a rainband B developing inside this patial eyewall. With the development of rainband B and its

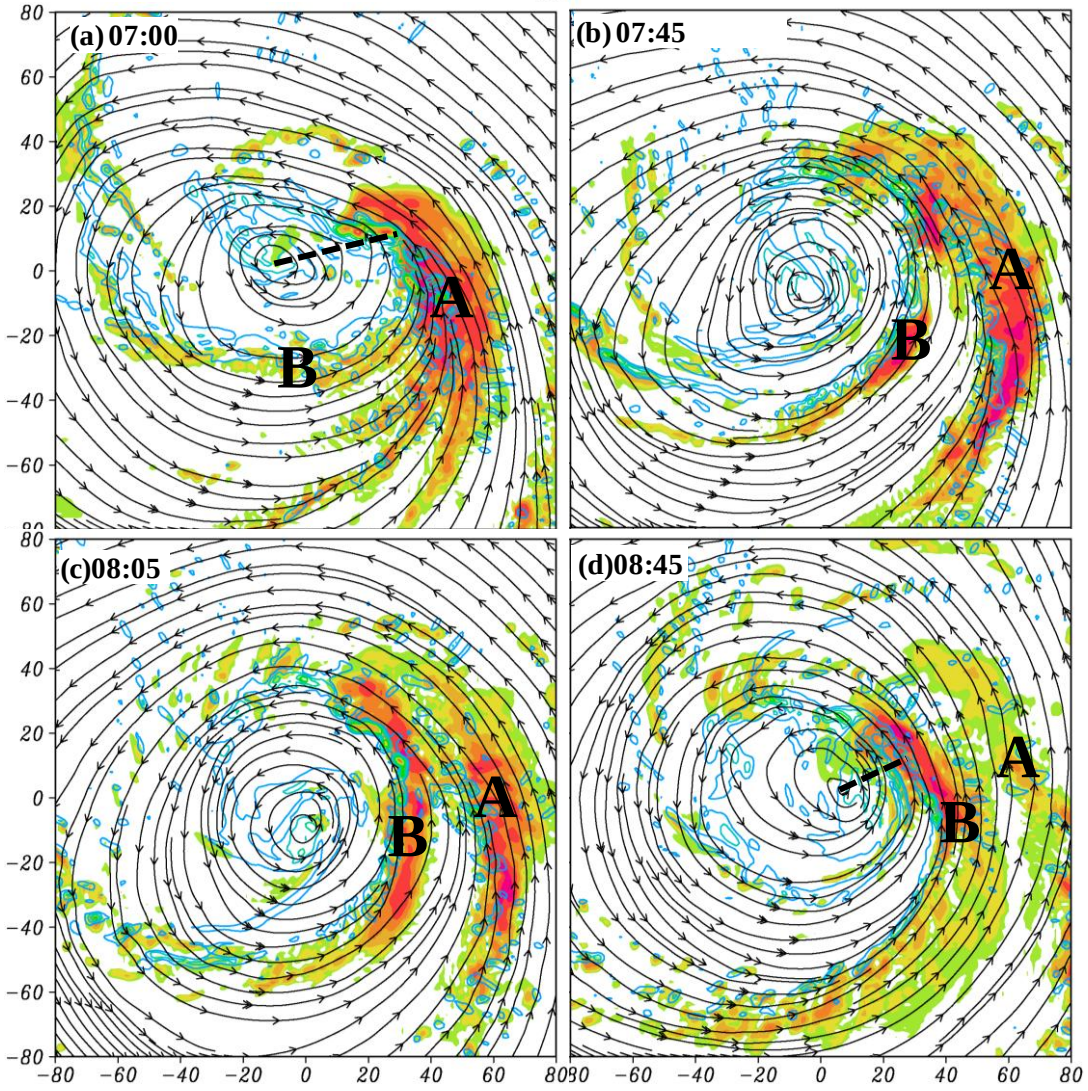


Figure 4.7: Horizontal distribution of radar reflectivity (shaded) superposed with streamlines and vorticity (contoured) at z = 1 km at a) 07:00, b) 07:45, c) 08:05 and d) 08:45. Letters, “A” and “B”, denote two different rainbands.

outward propagation due to VRWs and dissipation of partial eyewall A, the rainband B becomes the new partial eyewall in about 2 hours. In contrast to the stark asymmetric pattern of radar reflectivity is the symmetry of the vorticity field, which is especially obvious in Fig. 4.7d where vorticity shows a symmetric ring pattern. The

comparative horizontal structures of the precipitation and vorticity fields are the key to the formation of new bands, as we will be shown in the next.

Before we answer why the new band forms, we first quantify the asymmetry of the precipitation and vorticity fields by using the wave decomposition. As we can see, wavenumber (WN)-1 dominates the precipitation filed, especially in the first 11 hours, after which it starts decreasing, implying that the eyewall begins to wrap around. In contrast, the amplitudes of WN-1, WN-2 and WN-3 are comparable for the vorticity field, implying that the vorticity field is more symmetric. Why is the vorticity field more symmetric than the precipitation field? This has something to do with the conservativeness of the vorticity. An animation shows that the vorticity generated in the downshear region by strong convection is advected downstream with only slight dissipation due to the numerical diffusion. However, the hydrometeors evaporate quickly when they are advected downstream to the dry region on the upshear side. Despite the absence of precipitation on the upshear side, the evaporation of hydrometeors can moisten the dry air and precondition for the generation of rainbands at a later time.

Based on the above results, we propose that the downstream advected vorticity associated with surface frictional convergence contributes to the formation of new bands in a favorable condition with high moisture content. In order to verify this hypothesis, we plot the horizontal distribution of relative vorticity, radar reflectivity and convergence at 05:30 and 06:00, as in Fig. 4.8.

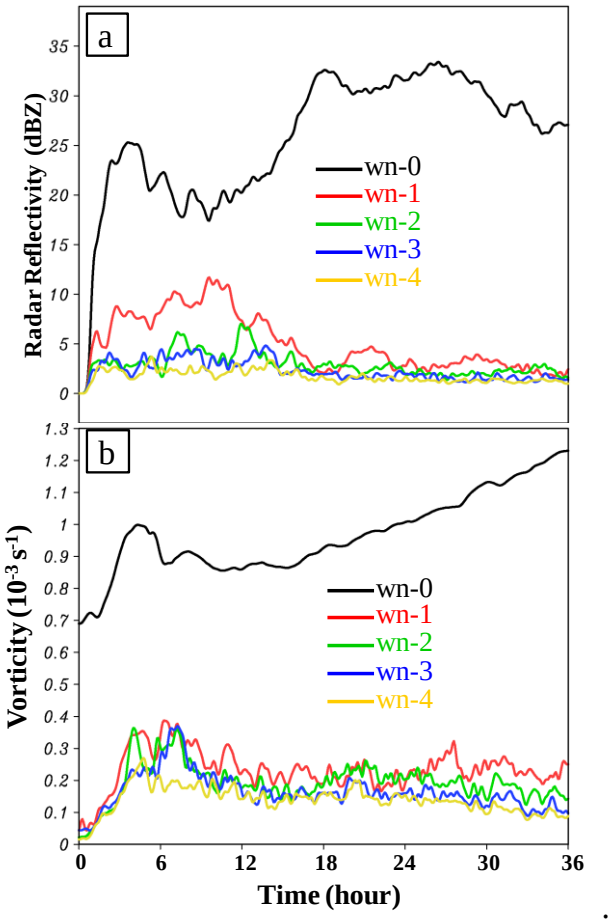


Figure 4.8 Time series of the amplitudes of WN-0, WN-1, WN-2, WN-3, WN-4 for a) radar reflectivity, and b) relative vorticity at 1-km altitude in 60 km X 60 km subdomain surrounding the storm center.

At 05:30, the horizontal distribution of the relative vorticity and radar reflectivity show a very different picture. The radar reflectivity with a partial eyewall near 40 km radius and another rainband occur far away from the center to the west near 100 km radius, indicates a highly asymmetric pattern. The wind speed also shows a similar asymmetric pattern as radar reflectivity with the maximum winds

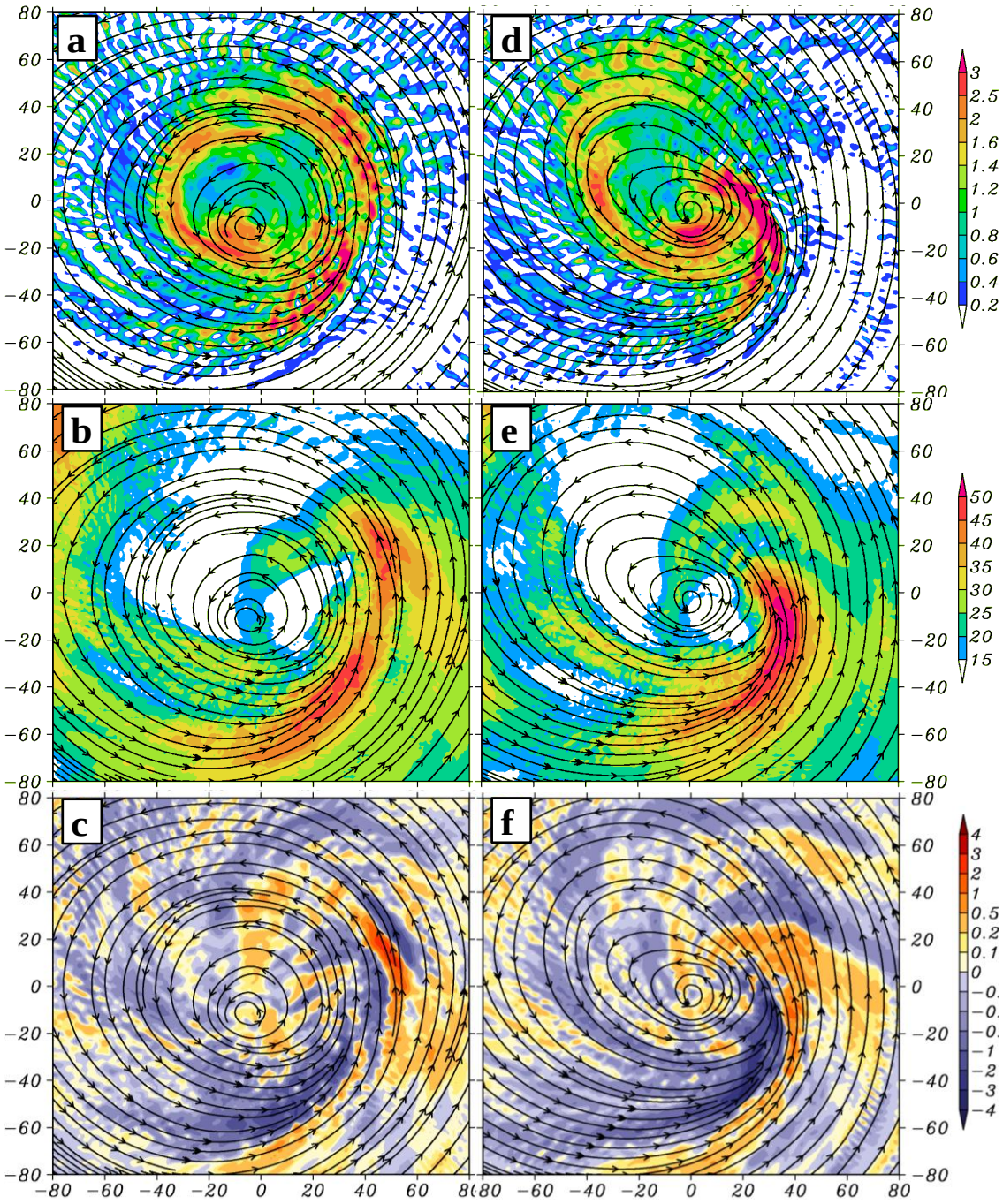


Figure 4.9: Horizontal distribution of a) the relative vorticity (unit: $10^{-3}$ $s^{-1}$) at 05:30, b) radar reflectivity (unit: dBz) at 05:30 at z = 1 km, c) divergence (unit: $10^{-3}$ $s^{-1}$) averaged in the 0-1 km layer at 05:30, d) relative vorticity (unit: $10^{-3}$ $s^{-1}$) at 06:00, e) radar reflectivity (unit: dBz) at 06:00 at z = 1 km and f) divergence (unit: $10^{-3}$ $s^{-1}$) averaged in the 0-1 km layer at 06:00, superposed with streamlines.

located to the northwest of the storm center but downstream of the radar reflectivity maximum. In contrast, the vorticity field shows a relatively symmetric pattern with a circular ring surrounding the storm center and numerous arms of vorticity dipole adjacent to the northwest of the vorticity ring. The circulation center is close to the south branch of the vorticity ring where there is a positive vorticity anomaly inside the ring. With the downstream advection of vorticity into the favorable region at 06:00, the associated convergence triggers new convection and leads to the formation of new rainbands.

### *4.4. Thermally indirect circulations in the eye*

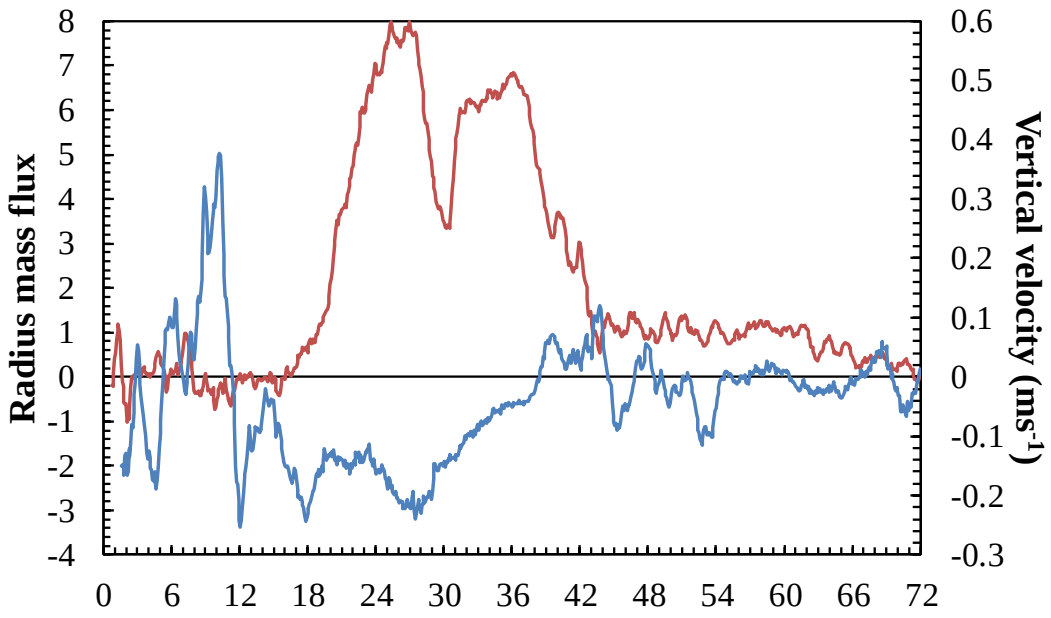


Figure 4.10 Time series of the vertical motion (blue line) that is averaged over a cylinder with 12 km height (5 km – 17 km) and a base of 10 km radius and the radial flux across 10 km radius.

Willoughby (1998) pointed out that the subsidence in the eye is associated with the eyewall contraction. In other words, the air in the eye has to be squeezed out

for the eye to shrink. However, the high inertial stability in the inner core region makes it difficult for any lateral movement and the vertical motion is required to complete the vacuum process. In order to diagnose the relationship between the subsidence, contraction and storm intensity, we calculated the time series of vertical motion averaged over a cylinder with 12 km height (5 km – 17 km) and a base of 10 km radius, as shown in Fig. 4.10. During the pre-RI period when the storm shows tilting, the area averaged vertical motion may capture part of the eyewall region and that is why we see a sharp spike around 9 h indicating strong upward motion. Around the onset of RI, the vertical motion decreases and reaches its minimum around 27 h, i.e., 9 hours earlier than the peak intensity of the storm, and increases in the subsequent 12 hours, after which it fluctuates around the zero line. Although subsidence is important in producing warming in the eye, the fundamental mechanism whereby the central pressure drops has to be outward mass flux, that serves as a vacuum to lower the central pressure. According to mass continuity, the radial mass flux should be related to subsidence in the eye and accounts for the storm intensification rate. A calculation of vertically integrated of radial mass flux across 10 km radii between 0.25-17 km (blue line in Figure 4.10) confirms the conjecture. The radial mass flux shows similar signals as the subsidence. The sudden drop between 27 and 30 h is caused by the fictitious ERC as mentioned in chapter 2. Without this fictitious ERC, the minimum vertical motion and maximum radial mass flux could lead the peak intensity around 6 hours.

Although we have shown that the radially outward mass flux accounts for the storm intensification, what does the vertical distribution of radial mass flux look like?

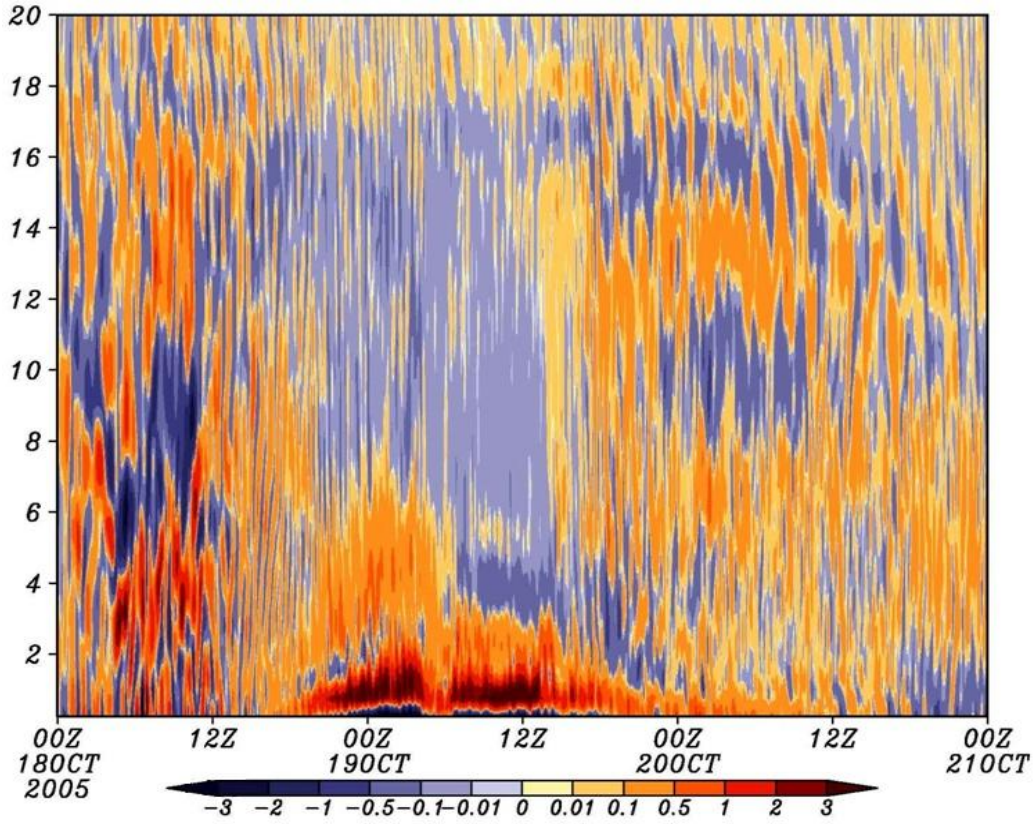


Figure 4.11 Time-height cross section of the radial mass flux across 10-km radii.

Which level is the maximum outward mass flux located? Liu et al. (1999) showed an outflow jet that slopes into the eyewall from the bottom of the eye center, which was referred to as the low-level return outflow (RO). This airstream, as noted in Liu et al. (1999), play an important role in (a) drawing air out of the eye to reduce the central pressure, and (b) transporting high-$\theta_e$ air from the bottom of the eye to support partly eyewall convection. Figure 4.11 shows that RO is responsible for most of air that is transported out of the eye, hence helping reduce the central pressure to a great degree. In contrast, the mass was transported inward toward the eye center above the layer of upper-level outflow. This implies that the upper level outflow can only transport air from eyewall updraft outward and cannot reduce central pressure directly. One

interesting feature is a sudden decrease of the depth of the outward mass flux layer after the fictitious ERC and an outward mass flux layer is replaced by an inward mass flux layer, which obviously decreases the intensification rate. The inward mass flux occurs between 7-17 km throughout 18-h RI period. After the peak intensity, the outward mass flux in the boundary layer decreases rapidly, and a much weaker RO can be inferred here.

### *4.5 Importance of a small eye size*

Previous study already showed the importance of small eye sizes on the intensification rate. We adapted a figure from Hack and Schubert (1986) to show this concept more clearly. Fig. 4.12 shows the time series of central pressure and RMW, which states one relationship: a storm intensifies much faster for a given contraction speed when the RMW becomes smaller. One stark difference between their result and the result we showed in Fig. 2.4 is that there is no onset of RI and the intensification rate increases smoothly. This is because they use an idealized model starting with a symmetric vortex without VWS. Hence, the contraction in Fig. 4.12 completely results from symmetric processes. The numerical prediction of Hurricane Wilma we conducted in this study also starts with a symmetric bogus vortex but the VWS sets in a few hours after the model initial time and produces an asymmetric pattern. Therefore, the trigger of RI is a combination of the eyewall closure and small eye size. If a storm forms a large convective ring, ever-contracting will show a rapid intensification but the intensification rate will become larger as the size shrinks with time.

Next, we will demonstrate the importance of the small size using a simple theoretical calculation based on two approximations that have been widely accepted when dealing with idealized hurricane situations: angular momentum conservation and gradient wind balance. Applying angular momentum conservation to the gradient wind balance equation and assuming a solid rotation between the hurricane center and the RMW, we got the following relationship between the RMW and the pressure drop from the RMW to the center with the angular momentum at $10^6$ $m^2$ $s^{-1}$ as in Fig. 4.13.

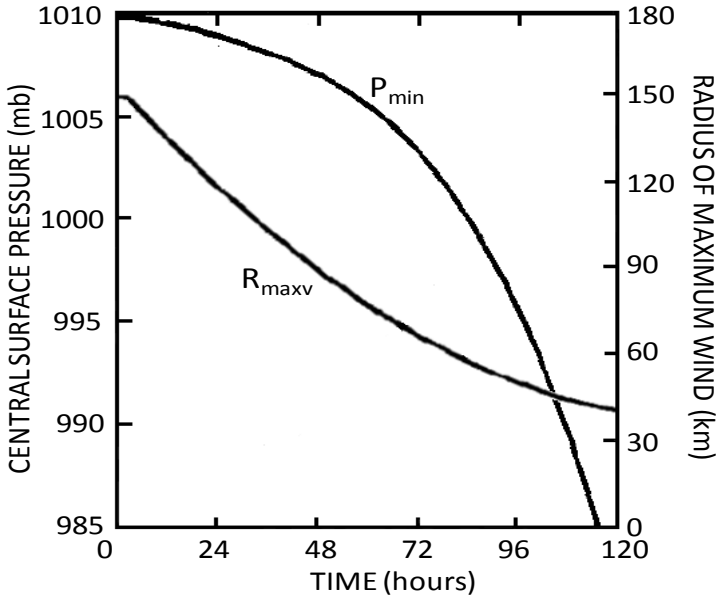


Figure 4.12 Time series of central surface pressure and radius of maximum wind from a nonlinear model. (Adapted from Hack and Schubert 1986).

It can be readily seen that the contraction of the RMW will not lead to much pressure drop until it reaches a small radius. When the RMW reaches a small radius, a further slight contraction will yield a huge pressure drop. This is physically understandable. The smaller the RMW is, the larger is the inertial stability. In order to overcome the increased radial resistance, the radial pressure gradient force has to increase, too.

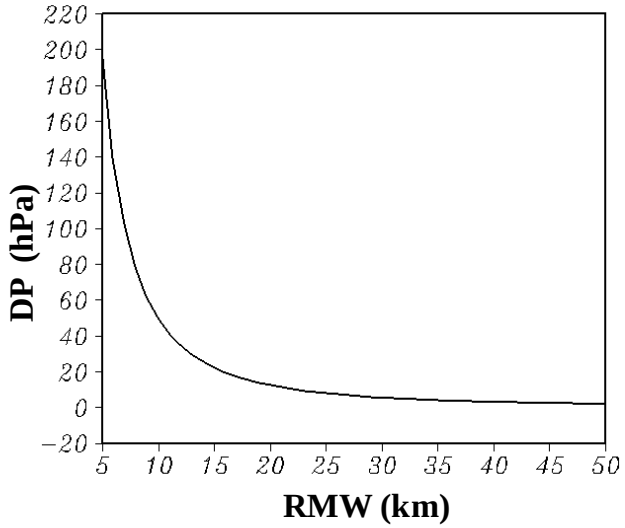


Figure 4.13 The relationship between RMW and pressure deficit in the eye.

### *4.6 Trochoidal oscillation*

Trochoidal oscillation has been observed and simulated in many hurricanes (Jordan 1966; Muramatsu 1986; Liu et al. 1999; Rogers et al. 2003) and its behavior can be divided into two different kinds: one is associated with the trochoidal oscillation of the whole tropical cyclone system and the other one associated with the low pressure center rotating cyclonically in the eye. Wavenumber-1 instability induced by VWS is usually considered as the main reason for trochoidal oscillation (Flatau and Stevens 1993; Nolan 2010). However, Yeh (1950) conducted a series of sensitivity tests and showed that the trochoidal oscillation can still occur in the absence of VWS. It only disappears when the diabatic heating is turned off and he concluded the trochodial oscillation is caused by the mutual adjustment of flow fields and diabatic heating in deep convection.

In the present case, we also observed trochoidal oscillation with the low pressure center rotating cyclonically in the eye. Fig. 4.14 shows the track based on 60 km X 60 km area-averaged minimum sea level pressure and single-point minimum sea-level pressure. The red track (single point minimum sea-level pressure) drifts randomly over the first 6 hours, which is caused by the adjustment of the bogus vortex embedded in the initial conditions to the model set up. After 6 h, the red track starts rotating cyclonically around the mean track (black line). The cross track displacement and along track displacement both decreases over time and two tracks almost coincide between 30-60 h, after which the red track resumes the trochoidal oscillation with ever-increasing cross track displacement till the end of the simulation.

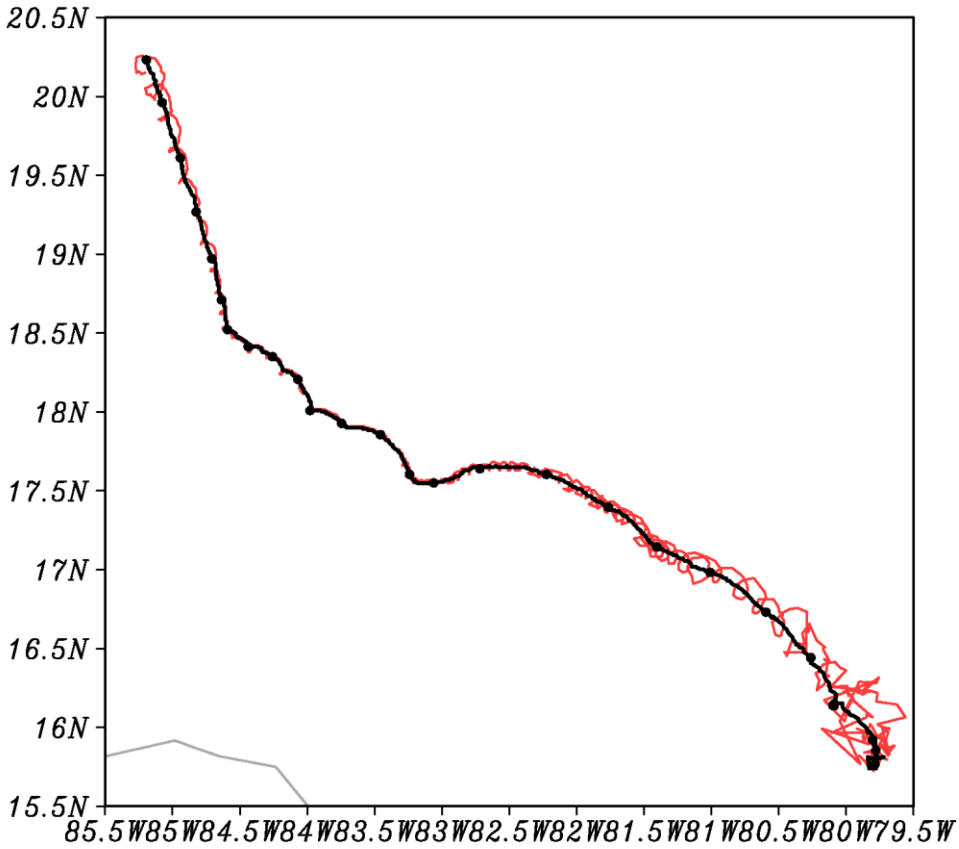

Figure 4.14: The track of localized pressure center (red line) and mean pressure center (averaged over 60 km X 60 km) at 5-min intervals for the 72-h prediction period. The black dots indicate 3-hour intervals.

Next, we focus on the trigger of the RI period and RI. The oscillation period decreases from about 2 h around 08:00 to 1 h at the onset of RI (15:00), further to 20 min at peak intensity time (36:00). The characteristic of trochoidal oscillation does not differ dramatically before and after the onset of RI, with ever-decreasing across track displacement. But there is one notable difference: the along track displacement does show dramatically changes. Before the onset of RI, the along track displacement is about 30 km for a cycle while it decreases rapidly to about 10 km after the onset of RI.

Overall, the amplitude of trochoidal oscillation is associated with the storm intensity and eye size and this is intuitively understandable. The storm with strong intensity tends to have more symmetric structures and therefore the oscillation amplitude is smaller. For a storm with a small size, the oscillation amplitude is also smaller because the oscillation is confined in the eye.

### *4.7 Chapter summary*

In this chapter, we addressed the eyewall contraction and demonstrated the importance of a small eye size in RI.

It is found that the formation of the small eye size can be divided into three stages: spin-up (0 – 6 h), asymmetric contraction (6 – 15 h) and symmetric contraction. The spin-up process accounts for about 50-km radius contraction, which is caused by the unbalanced state in the model initial condition. The asymmetric

contraction is associated with the formation of new bands inside the eyewall. The vorticity, generated in the downshear region by deep convection, is advected downstream. In the presence of friction, the vorticity can induce convergence and contribute to the formation of new rainbands. The symmetric contraction, although contributing less significantly to the size change, is responsible for the record RI rate. This is due to the fact that the eyewall size reaches a very small value when it becomes symmetric.

The importance of the eye size is demonstrated by citing previous work and by a simple theoretic calculation based on AAM conservation, solid body rotation and gradient wind balance. It was shown that the storm intensifies much faster for a given contraction speed when the RMW is very small.

During the eyewall contraction, the air in the eye descends and is transported outward in the boundary layer. In the meantime, air moves inward toward the eye center at the upper level. This circulation is referred to as thermally indirect circulation since it is not driven by buoyancy as the secondary circulation.

Trochoidal oscillation is also observed in this study and the amplitude of trochoidal oscillation is associated with the storm intensity and eye size. The amplitude is smaller for the storm with stronger intensity and a smaller eye size.

# Chapter 5. Conclusions and future work

## *5.1 Conclusions*

The RI issue is addressed in this dissertation by analyzing 72-h cloud-permitting model predictions of Hurricane Wilma (2005) with the Weather and Research Forecast (WRF) model at the finest grid sizes of 1-2 km. With the implementation of the GFDL bogus vortex in the initial conditions and our specified vertical level distribution, the WRF model captures a 15-h pre-RI stage with slow deepening rate, an RI stage with the rate of more than 4 hPa $h^{-1}$ for an 21-h period, 889 hPa minimum central pressure and the 36-h weakening period after the peak intensity.

The model prediction is verified against available observations, including satellite, flight data. Results show that the model reproduces several major features reasonably well, such as a partial eyewall open to the west in the pre-RI stage, a small symmetric eywall in the RI stage and an ERC after the peak intensity.

After analyzing the model prediction, we found that an upper level warm core, resulting from the subsidence of stratospheric air associated with the detrainment of CBs, is critical in determining the record RI rate of Hurricane Wilma. The warm core forms in the same layer as the upper outflow, which serves as a protection role in preventing it from being ventilated away by the environment flow. Results show that the CBs are most active during the pre-RI stage and the subsidence warming they produced cannot accumulate in the eye because of the strong divergent flow in the downshear quadrant that advects the warming all the way outward. Most of the warming is also propagated away by gravity waves in the pre-RI stage because of an

unbalanced state. In contrast, the upper level becomes symmetric and more balanced and the subsidence warming due to the detrainment of CBs can accumulate efficiently and contribute to the rapid development of the upper level warm core. The fact that the upper level warm core is more efficient in reducing surface pressure has been stated implicitly in the hydrostatic equation but it does not receive much attention.

Besides the upper level warm core, the small size is another important factor that leads to the record RI of Hurricane Wilma and this is demonstrated by a theoretic calculation by applying gradient wind balance, angular momentum conservation and solid body rotation. It was found that the storm intensifies much faster for a given contraction speed if the RMW is very small.

The process of small eyewall formation can be divided into three stages: spin-up, asymmetric contraction and symmetric contraction. The asymmetric contraction is associated with the formation of new rainbands inside the eyewall. Convectively generated vortiticity bands in the downshear region and advected downstream can induce convergence in the presence of surface friction. In the presence of high moisture content, the convergence can trigger deep convection in the aid of diabatic heating and leads to the formation of new rainbands.

In summary, given the favorable background, such as warm SSTs and weak VWS, the following four inner-core factors contribute to the record RI rate of Hurricane Wilma:

- The upper level warm core, which is more efficient in reducing surface pressure, when it is located higher up;

- A large amount of convective bursts, which tends to detrain in the lower stratosphere, accounting for the formation of the upper-level warm core;
- The small size: a slight contraction could lead to a huge surface pressure drop in the eye;
- The symmetric eyewall, which makes diabatic heating the eyewall more efficient in spinning up the hurricane vortex.

### *5.2 Future work*

Despite significant results from the study above mentioned, there are still some questions in need of further and more systematic study in order to address the upper level warm core issue comprehensively and provide the guidance for RI forecast.

First, what determines the warm core altitude? Previous studies on observation and model simulations indicate that the warm core altitude can vary from 4 km (Hurricane Debby 2006) to 14 km (Hurricane Wilma 2005). What sets the drastic differences between warm cores in different storms? Even for the same storm, the warm core altitude changes from stage to stage. As shown in Fig. 1, the warm core is located at 12 km in pre-RI and post-RI stages and 14 km in RI stages. No matter what the altitude is, the warm core in the eye has to result from the subsidence and different mechanisms driving subsidence can have a great impact on the warm core altitude and the storm intensity. We already mentioned above that the rapid development of the upper level warm core in RI stage, especially above 14 km, is due to the detrainment subsidence of CBs. In contrast, the detrainment subsidence contributes little to the upper level warm core in pre-RI and post-RI stages since most

warming due to CBs is propagated away by internal gravity waves and advected away by strong SRF in the eye for the former and little CBs-induced warming occurs for the later. Hence, the warm core altitude in pre-RI and post-RI stages, which is still very high compared to other observations, is determined by a mechanism different from CBs-induced subsidence. The unusually high warm core altitude in pre-RI and post-RI stages is one key factor that contributes to RI of Hurricane Wilma. Then what drives subsidence to form a warm core without the aid of subsidence-induced by CBs? Unfortunately, these have no consensus on this issue and it remains enigmatic because the subsidence in the eye is a thermally indirect. In despite of lacking clear explanations, it has been well established that the warm core is determined by the thermal wind balance relationship based on the gradient wind approximation. By examining the basic dynamic and thermodynamic equations, Smith (1980) showed that subsidence is driven by an adverse axial gradient of perturbation pressure which is associated principally with the decay and/or radial spread of the tangential wind field with height at those levels of the cyclone where the tangential winds are approximately in gradient wind balance. This study does show a dynamical consistent picture of warm core but the warm core is treated passively as a response to the wind fields. It also did not shed light on how the storm structure respond to large scale factors and impacts the storm intensity. In this proposal, we would like to explore the impact of environment factors on the warm core altitude.

In order to conduct this experiment, we will first choose 20 storms, 10 with upper level warm core ( $z \geq 10$ km) and 10 with middle level warm core ($z \leq 5$ km), based on the National Centers for Environmental Prediction (NCEP) final analysis.

Second, two datasets based on the composite analysis of these two groups will be obtained, one for upper level warm core and one for middle level warm core. The main environmental factors included in these two datasets are: SST, vertical distribution of temperature (static stability and tropopause height), vertical wind shear (VWS) and vertical distribution of moisture distribution. The two datasets will provide initial and boundary conditions for two sets of idealized simulations. In order to run an idealized simulation, an initial vortex is needed. The height of the warm core in the initial vortex is not expected to play a role in the evolution of warm core height, which can be seen from Fig.1a. The warm core is initially located at 8 km while it quickly adjusts to 12 km 3 hours after the model kicks off, which strongly implies that environmental factors take control on the altitude of the warm core. The two idealized simulations using different initial and boundary conditions are expected to produce storms with different warm core altitudes. If this is the case, a series of sensitivity tests will be performed to identify which environmental factors are responsible for determining the warm core altitude.

Another question related to the warm core issue is how fast its magnitude increases. As we mentioned above, the upper level warm core develops slowly in pre-RI stage and intensifies rapidly in RI stage because of different storm structures in these two stages, which pinpoints a key feature that influences the warm core development — asymmetry vs. symmetry. The eyewall closure is demonstrated to be the trigger of RI of Hurricane Wilma and the unusally high altitude of the warm core is proved to be responsible for the record RI rate. This raises another question in addressing the warm core issue: when does the eyewall close? It is well known that

VWS produces asymmetry by inducing upward motion downshear and downward motion upshear (Frank and Ritchie 1999, 2000) while some studies show that in some cases storms can withstand to VWS because shear-forced secondary circulation can oppose the destructive role of the VWS (Zhang and Kieu 2005). The storm structure does not only depend on VWS but also on SST and moisture distribution in the stratosphere. Warm SST can produce substantial sea-to-air flux and help and speed up the spin-up process while dry air in the lower troposphere can significantly delay the spin-up by the entrainment that suppresses the deep convection. Apparently, the interaction of different environmental factors and different scales makes it difficult to predict the timing of the formation of a symmetric eyewall even though the forecast of environmental factors has advanced to the point where they can be relatively accurately predicted.

As the second step in this proposal, we would like to perform a series of sensitivity tests to explore the interactions of different environment factors and different scales. The two main factors we would like to test are SST and VWS. First, a control simulation will be conducted using 28 ºC uniform SST and 7.5 m $s^{-1}$ unidirectional VWS. Then 25 sensitivity tests will be conducted by using 5 different SST (26, 27, 28, 29, and 30 ºC) and 5 different VWS (2.5, 5, 7.5, 10 and 12.5 m $s^{-1}$). The results from the sensitivity tests will be compared and analyzed to provide guidance on how the storm structure interacts with the change in environmental factors and impacts the warm core development.

The analysis based on the control run presented also indicates that there exists a relationship between convective bursts activity, thermally indirect circulation in the

eye, secondary circulation and primary circulation. It was found that strongest convective bursts activity leads the onset of RI a few hours while the weakening of thermally indirect circulation and the secondary circulation leads the weakening of the primary circulation. This result has great potential in advancing forecast of RI but it is only from one case. Hence, an analysis of the corresponding changes in the secondary circulations and thermal plume characteristics during the intensification process will also be undertaken for all the sensitivity tests proposed above.

With the accomplishment of the experiments proposed here, the forecast of RI can be greatly advanced for two reasons. First, the environmental factors can be predicted relatively accurately from the global model but their impacts on the storm intensity and structure are not monotonic and linear. With the help of understanding the mechanisms by which they impact on the storm structure, the forecast of large scale factors can be much more meaningful and useful in adding the forecast of RI. Second, the warm core is the fundamental and key feature of a hurricane and the impact of warm core height on storm intensity is theoretically solid.

In addition to the work related to the upper level warm core, diagnostic study from sensitivity tests is also desirable in order to help forecasting intensity change. Over the course of obtaining a successful prediction, a series of sensitivity tests have been conducted, including bogus vortex, vertical resolution, microphysics and SST. Result show the prediction of Hurricane Wilma is sensitive to these parameters but in-depth analysis has not been carried out to understand how and why these parameters impact the storm structure and intensity. A preliminary analysis of microphysics sensitivity test using Lin et al. (1983) microphysics scheme is given in

Appendix A. Most of the sensitivity tests we have conducted adopt coarse horizontal and vertical resolution. In the further, we would like to conduct these sensitivity test using the same resolution as the control run shown in chapter 2 and perform in-depth diagnostic analysis.

# Appendix A. A sensitivity experiment with the Lin microphysics scheme

In this study, we have conducted a microphysics sensitivity prediction with the Lin et al. (1983) microphysics scheme before obtaining a successful control run. Since the Lin scheme has been used to obtain several successful hurricane simulations, e.g., by Liu et al. (1997), and Zhu et al. (2002), it is of interest to examine how well the WRF model with the Lin scheme could reproduce the structures and evolution of Hurricane Wilma (2005). Thus, in this appendix, we present the sensitivity prediction with the Lin scheme, hereafter referred to as HRES_LIN, while holding all the other parameters identical to those presented in Chapter 2.

It should be mentioned that the track of the HRES_LIN storm is very similar to that shown in Fig. 2.3, so it is not shown herein. However, the intensity forecasts show a quite different picture.

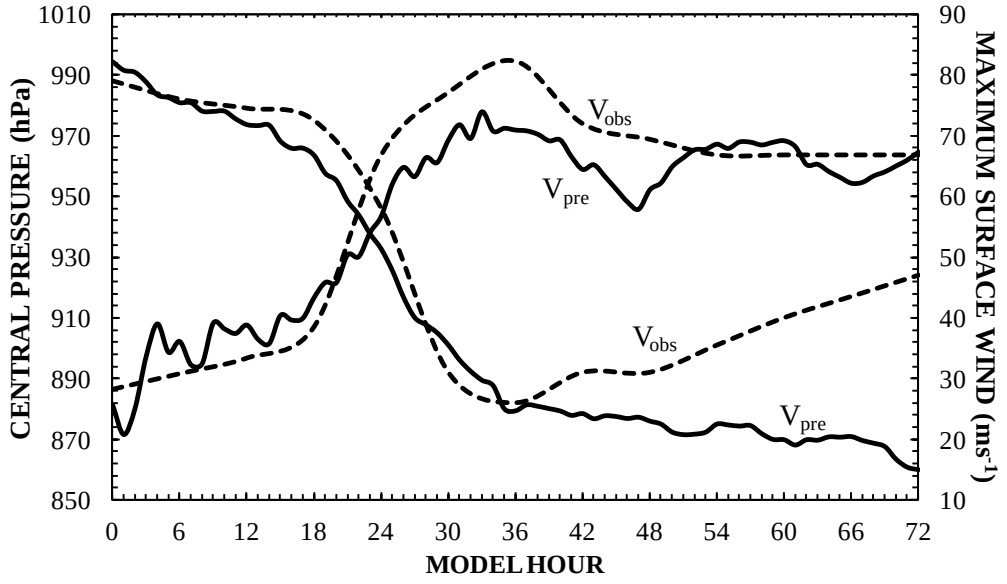

Figure A.1: Time series of model-predicted (PRE, solid) and the observed (OBS, dashed) maximum surface wind ($V_{MAX}$, m s-1) and minimum sea-level pressure ($P_{MIN}$, hPa) for during the period of 18/00-00 to 21/00-72.

Figure A.1 shows the time series of the HRES_LIN storm with a 5.25 hPa $hr^{-1}$ deepening rate for 12 consecutive hours, 74 m $s^{-1}$ peak maximum surface wind and 880 hPa central pressure. The results are more comparable to the observations over the RI period than the control run presented in chapter 2. However, after the peak intensity, the predicted central pressure keeps deepening despite the much slower intensification rate while the observations indicate the pressure starts weakening because of an eyewall replacement cycle. In contrast to the ever-deepening central pressure, the maximum surface wind starts weakening after the peak intensity but it shows significant fluctuations, which is associated with two ERCs as we will detail next. In addition to the drastic discrepancy between the prediction and the observation after the peak intensity, high frequency fluctuation in central pressure with 10-minute period and amplitude as large as 20 hPa is another reason we did not use HRES_LIN as the control run. The generation of the high frequency fluctuation is unclear but it only occurs when the horizontal resolutions increases to 1 km. Numerical instability might be one potential cause but decreasing time step does not eliminate the high frequency fluctuation.

Fig. A.2 shows the development of two ERCs, i.e., 12-h duration (i.e. 36 – 48 h) and 15-km width in the moat region, and 18-h duration (i.e. 54 – 72 h) and 20-km width in moat region. This seems to hint that the narrower the moat region is, the short the duration is. This is physically intuitive. If the contraction speed is fixed for

both the outer and inner eyewalls, it will take a longer time for the ERC to complete if the moat region is wider. Fig. A.2 indicates that the contraction speeds for two outer eyewalls are actually very similar. It also reveals that the contraction speed prior to the ERC is faster than that after the ERC. This is because the high inertial stability associated with the inner eyewall does not disappear immediately after the inner eyewall dissipates and it serves as a barrier to prevent the further contraction of the outer eyewall, which can also be discerned from Figs. 2.10 and 2.11. If we compare Fig. 2 with Fig.3, we notice that the maximum surface wind and the minimum central pressure respond to the ERCs in a very different way. As we mentioned,

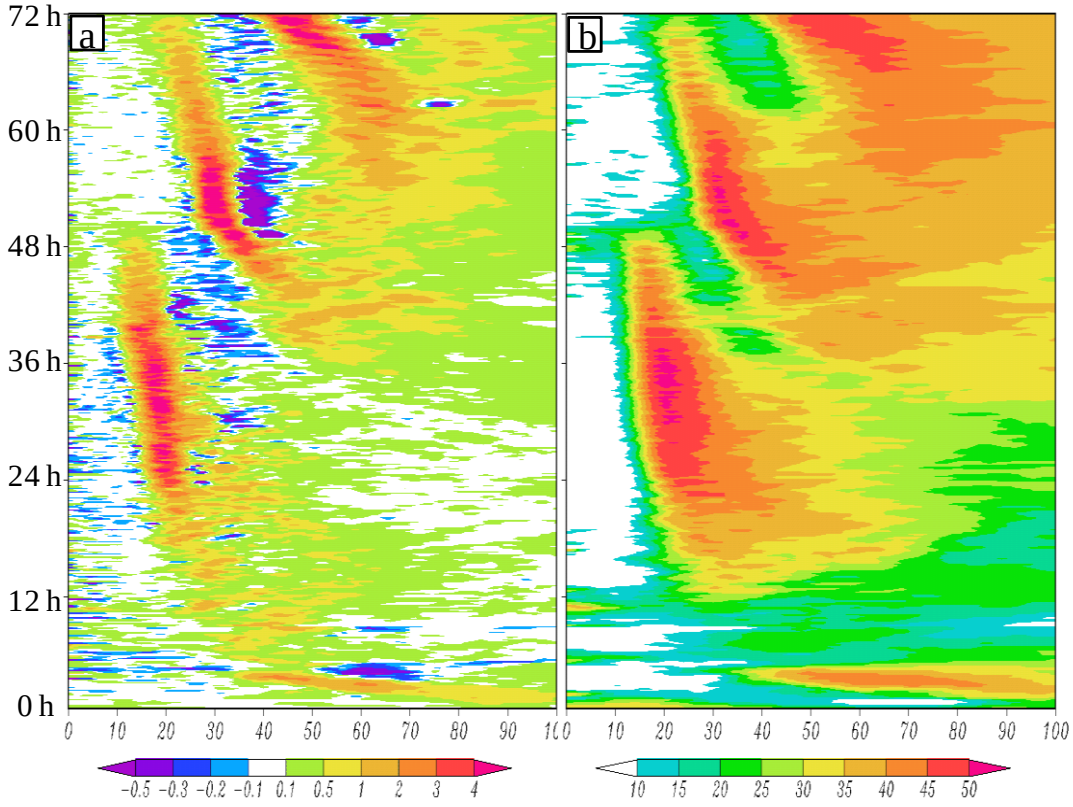


Figure A.2: Radius-time cross section of the azimuthally averaged a) vertical motion and b) radar reflectivity at z = 4 km.

The minimum central pressure keeps deepening while the maximum surface wind fluctuates with significant amplitudes; these all occur during the two ERCs. This result appears to contradict with the two convention wisdoms. First, it has been widely accepted that when the minimum central pressure rises the maximum surface winds weakens based on gradient wind balance (Harper 2002). Second, the ERC is believed to weaken the storm unless the new eyewall resumes contraction. These two points were well addressed in a recent paper (Kieu et al. 2010). By examining a Rankine vortex in the situation of double eyewall and small size, the authors found that the frictional forcing in the planetary boundary layer (PBL), which could explain the linear contributions of the peak surface winds to the pressure drops to a great degree, becomes increasingly important for intense TCs when the eye size becomes small and hence the radial inflows in the PBL could no longer be neglected. The presence of the double eyewalls will further complicate the revisited pressure-wind relationship.

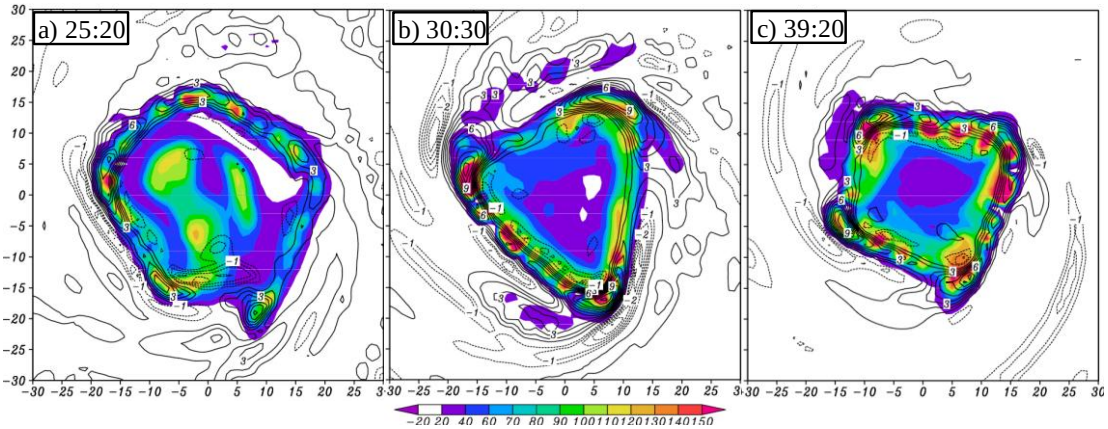


Figure A.3: Horizontal distribution of PV (shading) and vertical motion (contoured at 0.5 m $s^{-1}$ intervals for downward motion, and 1 m $s^{-1}$ for upward motion) at a) t = 25:20, b) t = 30:30 and c) t = 39:20 at z =1 km.

Figure A.3 shows polygonal shapes of the eyewall in terms of potential vorticity (PV) and vertical motion, ranging from triangle to pentagon, over the RI stage and a few hours following the peak intensity. This phenomenon has been documented in observations (Lewis and Hawkins 1982; Muramatsu 1986) and was explained based on internal gravity wave theories that was originally put forward to understand the formation of spiral rainbands by Willoughby (1978) and Kurihara (1976). A couple of recent papers (Schubert et al. 1999; KS2001) proposed a new explanation by applying vortex Rossby wave theory (Guinn and Schubert 1993; Montgomery and Kallenbach 1997). Schubert et al. (1999) examined the polygonal eyewall issue using an unforced barotropic nondivergent model and showed that polygonal eyewalls form as a result of barotropic instability near the RMW. The instability occurs when two counterpropagating vortex Rossby waves due to radial vorticity gradient changing sign become phase-locked. As the amplitude of the instabilities grows, the vorticity of the eyewall region pools into discrete areas, creating the appearance of polygonal eyewalls. The signal of barotropic instability is obvious in Fig. A.3, especially in Fig. A.4b where the eyewall takes on the shape of triangle. Spiral rainbands emanate from the three tips of vorticity triangles where vertical motion maximizes as vorticity is stripped off the outer edge. The wave decomposition analysis (not shown) indicates wavenumber 3 component dominates over wavenumber 1 and wavenumber 2 in the situation of vorticity triangles. The balanced flow fields (i.e., after removing divergence, not shown) show three cyclonic circulations associated with the three tips of the triangle.

Another interesting feature worthy of discussion is mesovortices inside the eyewall as shown in Fig. A.3a. The eyewall takes on the shape of pentagon and there are three mesovortices inside the eyewall. This feature has also been observed in Hurricane Isable (2003) (Kossin and Schubert 2004) and captured in an idealized simulation (KS2001) and the real-date simulation of Typhoon Nari (2001) by Zhang et al. (2011). KS2001 showed that mesovortices in the eyewall can chaotically migrate into the eye by examining the two-dimensional barotropic evolution of thin annular rings of enhanced vorticity embedded in nearly irrotational flow. When this happens, the vortex can experience drastic pressure fall. However, mesovortices migrating into the eye is not the main mechanism responsible for the RI in Hurricane Wilma. As mentioned in chapters 1 and 2, Wilma set record of a small eye size. With such a small eye, the high inertial stability will prevent any kind of lateral movement, especially at the later stage of RI. Indeed, mesovortices are not observed in the eye at the later stage of RI.

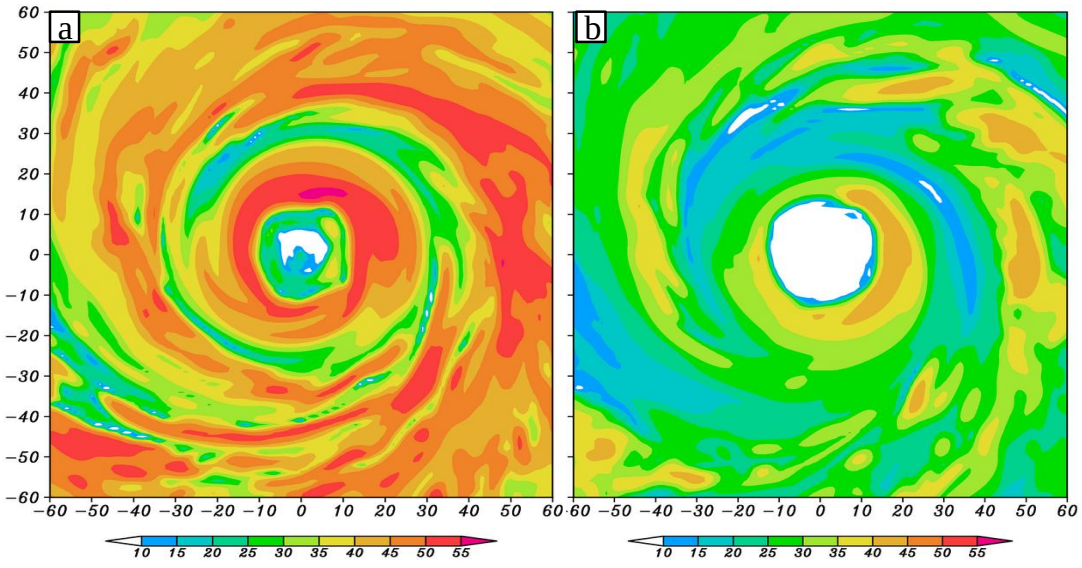

Figure A.4: Horizontal distribution of radar reflectivity averaged between a) 800 — 700 hPa and b) 350 — 450 hPa at t = 42 h.

The horizontal distribution of radar reflectivity 6 hours after the peak intensity is shown in Fig. A.4. As we can see, there are two eyewalls present and the inner eyewall is almost circular at this time, which is in distinct contrast to Fig. 3 which shows clear a polygonal eyewall. As discussed in KS2001, the polygonal eyewall with a PV ring will finally relax into a circular eyewall with a PV monopole. This PV ring-to-monopole transition has been observed in this HRES_LIN sensitivity test and the control run presented in chapter 2. A major difference between the numerical prediction presented in this dissertation and the idealized 2-dimensional barotropic simulation in KS2001 is that the monopole is surrounded by another PV ring associated with the second eyewall and it eventually merges with the new PV ring.

The moat region between the two eyewalls is very narrow, especially at the low levels (Fig. A.4a), which can be also seen from Fig. A.2. The double eyewalls feature in HRES_LIN is drastically different from the control run presented in chapter 2 in the following two aspects. First, HRES_LIN produces two ERCs while the control run only produces one ERC. Second, the moat region between two eyewalls is much narrower and the duration is much shorter in HRES_LIN as compared to the control run.

In addition to the different ERC features, the polygonal eyewall ranging from triangle to pentagon is not observed in the control run either.

Why two different microphysics schemes produce so much different storm structures? This certainly implies that cloud microphysics plays an important role in

the hurricane intensity forecast and the sensitivity results need to be further diagnosed in order to obtain conclusive results in terms of the role of cloud microphysics processes. This could be an important subject for future studies.

# Bibliography

Bender, M. A., I. Ginis, and Y. Kurihara, 1993: Numerical simulations of tropical cyclone-ocean interaction with a high resolution coupled model. *J. Geophys. Res*., **98**, 23 245-23 263.

——, 1997: The effect of relative flow on the asymmetric structure of the interior of hurricanes. *J. Atmos. Sci*, **54,** 703–724.

Betts, A. K., 1986: A new convective adjustment scheme. Part I: Observational and theoretical basis. *Quart. J. Roy. Meteor. Soc.*, **112,** 677–691.

——, and M. J. Miller, 1986: A new convective adjustment scheme. Part II: Single column tests using GATE wave, BOMEX, and arctic air-mass data sets. *Quart. J. Roy. Meteor. Soc.*, **112,** 693–709.

Black, M. L., and H. E. Willoughby, 1992: The concentric eyewall cycle of Hurricane Gilbert. *Mon. Wea. Rev.*, **120,** 947–957.

Blackwell, K. G., 2000: The evolution of Hurricane Danny (1997) at landfall: Doppler-observed eyewall replacement, vortex contraction/intensification, and low-level wind maxima. *Mon. Wea. Rev.,* **128,** 4002-4016.

Blanton, C. E., 2010: Polygonal eyewalls in a 2 km WRF simulation of Wilma (2005). *28th Conf. Hurr. Tropical Meteor.*, Amer. Meteor. Soc., 7.A6.

Bluestein, H. B., and D. S. Hazen, 1989: Doppler-radar analysis of a tropical cyclone over land: Hurricane Alicia (1983) in Oklahoma. *Mon. Wea. Rev.*, **117,** 2594-2611.

Blumen, W., 1972: Geostrophic Adjustment. *Rev. Geophys. Space Phys.*, **10,** 485-528.

Bosart, L. F., W. E. Bracken, J. Molinari, C. S. Velden, and P.G. Black, 2000: Environmental influences on the rapid intensification of Hurricane Opal (1995) over the Gulf of Mexico. *Mon. Wea. Rev.*, **128**, 322–352.

Braun, S. A., 2002: A cloud-resolving simulation of Hurricane Bob (1991): Storm structure and eyewall buoyancy. *Mon. Wea. Rev.*, **130,** 1573–1592.

——, and W. Tao, 2000: Sensitivity of high-resolution simulations of Hurricane Bob (1991) to planetary boundary layer parameterizations. *Mon. Wea. Rev.*, **128,** 3941–3961.

Chen, H., D.-L. Zhang, J. Carton, and R. Atlas, 2011: On the rapid intensification of Hurricane Wilma (2005). Part I: Model prediction and structural changes. *Wea. Forecasting*, **26,** 885-901.

Corbosiero, K. L., J. Molinari, and M. L. Black, 2005: The structure and evolution of Hurricane Elena (1985). Part I: Symmetric intensification. *Mon. Wea. Rev.*, **133,** 2905-2921.

Davis, C. A. and L. F. Bosart, 2001: Numerical simulations of the genesis of Hurricane Diana (1984). *Mon. Wea. Rev*., **129,** 1859-1881.

——, and L. F. Bosart, 2002: Numerical simulations of the genesis of Hurricane Diana (1984). Part II: Sensitivity of track and intensity prediction. *Mon. Wea. Rev*., **130,** 1100-1124.

——, W. Wang, J. Dudhia and R. Torn, 2010: Does increased horizontal resolution improve hurricane wind forecasts? *Wea. Forecasting*, **25**, 1826–1841.

Dudhia, J., 1989: Numerical study of convection observed during the winter monsoon experiment using a mesoscale two-dimensional model. *J. Atmos. Sci.*, **46,** 3077–3107.

Eliassen, A., 1951: Slow thermally or frictionally controlled meridional circulation in a circular vortex. *Astrophys. Norv.*, **5,** 19-60.

Elsberry, R. L., W. M. Frank, G. J. Holland, J. D. Jarrell, and R. L. Southern, 1987: A global view of tropical cyclones. Univ. Chicago Press, 185pp.

Emanuel, K. A.,1986: An air-sea interaction theory for tropical cyclones. Part I: Steady-state mainenance. *J. Atmos. Sci.*, **43,** 585-604.

——, 1988: The maximum intensity of hurricanes. *J. Atmos. Sci*., **45**, 1143-1155.

——, 1991: The theory of hurricanes. *Annual Rev. Fluid Mech.*, **23**, 179-196.

Fierro, A. O., and J. M. Reisner, 2011: High-resolution simulation of the electrification and lightning of Hurricane Rita during the period of rapid intensification. *J. Atmos. Sci.*, **68**, 477–494.

Flatau, M., and D. E. Stevens, 1993: The role of outflow-layer instabilities in tropical cyclone motion. *J. Atmos. Sci.*, **50,** 1721–1733.

Foley, G., 1998: A marked upper tropospheric temperature anomaly observed by an aircraft near a thunderstorm over inland Western Australia. *Aust. Met. Mag.*, **47,** 321-326.

Fortner, L. E., 1958: Typhoon Sarah, 1956. *Bull. Amer. Meteor. Soc*., **39,** 633-639.

Fovell, R. G., D. R. Durran, and J. R. Holton, 1992: Numerical simulations of convectively generated stratospheric gravity waves. *J. Atmos. Sci.*, **49**, 1427–1442.

Frank, W. M., and E. A. Ritchie, 1999: Effects of environmental flow on tropical cyclone structure. *Mon. Wea. Rev*, **127,** 2044–2061.

——, and ——, 2001: Effects of vertical wind shear on the intensity and structure of numerically simulated hurricanes. *Mon. Wea. Rev*, **129,** 2249–2269.

Gentry, R. C., T. T. Fujita, and R. C. Sheets, 1970: Aircraft, spacecraft, satellite, and radar observations of Hurricane Gladys, 1968. *J. Appl. Meteor.*, **9,** 837–850.

Gray, W. M., 1968: Global view of the origin of tropical disturbances and storms. *Mon. Wea. Rev*, **96,** 669–700.

——, 1998: The formation of tropical cyclones. *Meteor. Atmos. Phys.*, **67,** 37–69.

Guimond, S. R., G. M. Heymsfield, and F. J. Turk, 2010: Multiscale observations of Hurricane Dennis (2005): The effects of hot towers on rapid intensification. *J. Atmos. Sci.*, **67,** 633–654.

Guinn, T. A., and W. H. Schubert, 1993: Hurricane spiral bands. *J. Atmos. Sci.*, **50,** 3380–3403.

Hack, J. J., and W. H. Schubert, 1986: Nonlinear response of atmospheric vortices to heating by organized cumulus convection. *J. Atmos. Sci.*, **43**, 1559-1573.

Harnos, D. S. and S. W. Nesbitt, 2011: Convective structure in rapidly intensifying tropical cyclones as depicted by passive microwave measurements. Geophys. Res. Lett. **38**, L07805, doi:10.1029/2011GL047010.

Hawkins, H. F., and D. T. Rubsam, 1968: Hurricane Hilda, 1964. II: Structure and budgets of the hurricane core on October 1, 1964. *Mon. Wea. Rev.*, **96,** 617-636.

——, and S. M. Imbembo, 1976: The structure of a small, intense Hurricane—Inez 1966. *Mon. Wea. Rev.*, **104,** 418–442.

Heymsfield, G. M., J. B. Halverson, J. Simpson, L. Tian, and T. P. Bui, 2001: ER-2 Doppler radar investigations of the eyewall of Hurricane Bonnie during the Convection and Moisture Experiment-3. *J. Appl. Meteor*., **40**, 1310 – 1330.

Hirschberg, P. A., and J. M. Fritsch, 1993: On understanding height tendency. *Mon. Wea. Rev*., **121,** 2646–2661.

Hogsett, W., and D.-L. Zhang, 2009: Numerical simulation of Hurricane Bonnie (1998). Part III: Energetics. *J. Atmos. Sci.*, **66,** 2678-2696.

Holland, G. J., 1997: The maximum potential intensity of tropical cyclones. *J. Atmos. Sci.*, **54**, 2519–2541.

——, T. D. Keenan, and G. D. Crane, 1984: Observations of a phenomenal temperature perturbation in Tropical Cyclone Kerry (1979). *Mon. Wea. Rev.*, **112**, 1074–1082.

Holliday, C.R., and A. H. Thompson, 1979: Climatological characteristics of rapidly intensifying typhoons. *Mon. Wea. Rev.*, **107,** 1022-1034.

Hong, S.-Y., and Y. Noh, and J. Dudhia, 2006: A new vertical diffusion package with an explicit treatment of entrainment processes. *Mon. Wea. Rev.*, **134,** 2318–2341.

Houze**,** R. A., Jr., W.-C. Lee, and M. M. Bell, 2009: Convective contribution to the genesis of Hurricane Ophelia (2005). *Mon. Wea. Rev.*, **137**, 2778–2800.

Janjic, Z. I., 1994: The step-mountain eta coordinate model: further developments of the convection, viscous sublayer and turbulence closure schemes. *Mon. Wea. Rev.*, **122,** 927–945.

Jordan, C. L., 1966: Surface pressure variations at coastal stations during the period of irregular motion of Hurricane Carla of 1961. *Mon. Wea. Rev.*, **94,** 454–458.

Jorgensen, D. P., and M. A. LeMone, 1989: Vertical velocity characteristic of oceanic convection. *J. Atmos. Sci.*, **46,** 621–640.

Kaplan, J., and M. DeMaria, 2003: Large-scale characteristics of rapidly intensifying tropical cyclones in the North Atlantic basin. *Wea. Forecasting*, **18,** 1093–1108.

——, ——, and J. A. Knaff, 2010: A Revised tropical cyclone rapid intensification index for the Atlantic and Eastern North Pacific Basins. *Wea. Forecasting*, **25**, 220–241

Kelley, O. A., J. Stout, and J. B. Halverson, 2004: Tall precipitation cells in tropical cyclone eyewalls are associated with tropical cyclone intensification. *Geophys. Res. Lett.*, **31,** L24112, doi:10.1029/2004GL021616.

Kieu, C. Q., and D.-L. Zhang, 2009: An analytical model for the rapid intensification for tropical cyclones. *Quart. J. Roy. Meteor. Soc.*, **135,** 1336-1349.

——, and ——, 2010: A piecewise potential vorticity inversion algorithm and its application to hurricane inner-core anomalies *J. Atmos. Sci.*, **67**, 2616–2631.

——, H. Chen, and D.-L. Zhang, 2010: An examination of the pressure - wind relationship in intense tropical cyclones. *Wea. Forecasting*, **25,** 895-907.

Kimball, S. K., and F. C. Dougherty, 2006: The Sensitivity of idealized hurricane structure and development to the distribution of vertical levels in MM5. *Mon. Wea. Rev.*, **134,** 1987–2008.

Kossin, J. P., and W. H. Schubert, 2001: Mesovortices, polygonal flow patterns, and rapid pressure falls in hurricane-like vortices. *J. Atmos. Sci.*, **58**, 2196-2209.

Kurihara, Y., 1976: On the development of spiral bands in a tropical cyclone. *J. Atmos. Sci.,* **33,** 940–958.

——, M. A. Bender, and R. J. Ross, 1993: An initialization scheme of hurricane models by vortex specification. *Mon. Wea. Rev.*, **121,** 2030–2045.

LaSeur, N. E., and H. F. Hawkins, 1963: An analysis of Hurricane Cleo (1958) based on data from research reconnaissance aircraft. *Mon. Wea Rev*., **91,** 694-709.

Lee, W., and M. M. Bell, 2007: Rapid intensification, eyewall contraction, and breakdown of Hurricane Charley (2004) near landfall. *Geophys. Res. Lett.,* **34,** L02802, doi: 10.1029/2006GL027889.

Leipper, D., 1967: Observed ocean conditions and hurricane Hilda, 1964. *J. Atmos. Sci.,* **24,** 182-196.

Lewis, B. M., and H. F. Hawkins, 1982: Polygonal eye walls and rainbands in hurricanes. *Bull. Amer. Meteor. Soc.*, **63,** 1294–1300.

Li, X., and Z. Pu, 2008: Sensitivity of numerical simulation of early rapid intensification of Hurricane Emily (2005) to cloud microphysical and planetary boundary layer parameterizations. *Mon. Wea. Rev.*, **136,** 4819–4838. MacDonald, N. J., 1968: The evidence for the existence of Rossby-like waves in the hurricane vortex. *Tellus,* **20,** 138-150.

Lin, Y.-L., R. D. Farley, and H. D. Orville, 1983: Bulk parameterization of the snow field in a cloud model. *J. Climate Appl. Meteor.*, **22,** 1065–1092.

Liu, Y., D.-L. Zhang and M. K. Yau, 1997: A multiscale numerical study of Hurricane Andrew (1992). Part I: Explicit simulation and verification. *Mon. Wea. Rev.*, **125,** 3073-3093.

——, ——, and ——, 1999: A multiscale numerical study of Hurricane Andrew (1992). Part II: Kinematics and inner-core structures. *Mon. Wea. Rev.*, **127,** 2597-2616.

Malkus, J. S., and H. Riehl, 1960: On the dynamics and energy transformations in steady-state hurricanes. *Tellus*,**12,** 1–20. Marks, F. D., and R. A. Houze, 1984: Airborne Doppler radar observations in Hurricane Debby. *Bull. Amer. Meteor. Soc.*, **65,** 569-582.

——, and ——, 1987: Inner core structure of Hurricane Alicia from airborne Doppler radar observations. *J. Atmos. Sci.*, **44,** 1296-1317.

——, L. K. Shay, and Co-authors, 1998: Landfalling tropical cyclones: Forecast problems and associated research opportunities. Report of the Fifth Prospectus Development Team to the U.S. Weather Research Program. *Bull. Amer. Meteor. Soc*., **79,** 305-323.

Mlawer, E. J., S. J. Taubman, P. D. Brown, M. J. Iacono, and S. A. Clough, 1997: Radiative transfer for inhomogeneous atmosphere: RRTM, a validated correlated-k model for the longwave. *J. Geophys. Res.*, **102,** D14, doi:10.1029/97JD00237.

Molinari, J., P. K. Moore, and V. P. Idone, 1999: Convective structure of hurricanes as revealed by lightning locations. *Mon. Wea. Rev.*, **127,** 520–534.

——, and D. Vollaro, 2010: Rapid Intensification of a Sheared Tropical Storm. *Mon. Wea. Rev.*, **138,** 3869–3885.

Möller, J. D., and M. T. Montgomery, 1999: Vortex Rossby Waves and Hurricane Intensification in a Barotropic Model. *J. Atmos. Sci.*, **56**, 1674–1687.

——, and L. J. Shapiro, 2005: Influences of asymmetric heating on hurricane evolution in the MM5. *J. Atmos. Sci.*, **62**, 3974–3992.

Montgomery, M. T., and R. J. Kallenbach, 1997: A theory for vortex Rossby-waves and its application to spiral bands and intensity changes in hurricanes. *Quart. J. Roy. Meteor. Soc.*, **123,** 435-465.

——, M. E. Nicholls, T. A. Cram, and A. B. Saunders, 2006: A vortical hot tower route to tropical cyclogenesis. *J. Atmos. Sci.*, **63,** 355–386.

Mrowiec, A. A., S. T. Garner, and O. M. Pauluis, 2011: Axisymmetric hurricane in a dry atmosphere: Theoretical framework and numerical experiments. *J. Atmos. Sci.*, **68**, 1607–1619.

Muramatsu, T., 1986: The structure of polygonal eye of a typhoon. *J. Meteor. Soc. Japan*, **64,** 913–921.

——, 1986: Trochoidal motion of the eye of Typhoon 8019. *J. Meteor. Soc. Japan*, **64,** 259–272.

Nascimento, E. L., and K. K. Droegemeier, 2006: Dynamic adjustment in a numerically simulated mesoscale convective system: Impact of the velocity field. *J. Atmos. Sci.*, **63**, 2246–2268.

Nolan, D. S., 2007: What is the trigger for tropical cyclogenesis? *Aust. Meteor. Mag.*, **56,** 241–266.

——, M. T. Montgomery, L. D. Grasso, 2001: The Wavenumber-One Instability and Trochoidal Motion of Hurricane-like Vortices. *J. Atmos. Sci.*, **58**, 3243–3270.

——, and L. D. Grasso, 2003: Three-dimensional, nonhydrostatic perturbations to balanced, hurricane-like vortices. Part II: Symmetric response and nonlinear simulations. *J. Atmos. Sci.*, **60**, 2717–2745.

——, Y. Moon, and D. P. Stern, 2007: Tropical cyclone intensification from asymmetric convection: Energetics and efficiency. *J. Atmos. Sci.*, **64**, 3377–3405.

Ooyama, K., 1969: Numerical simulatin of the life cycle of tropical cyclones. *J. Atmos. Sci*., **26,** 3-40.

Parrish, J. R., R. W. Burpee, F. D. Marks, and R. Grebe, 1982: Rainfall patterns observed by digitized radar during the landfall of Hurricane Frederic (1979). *Mon. Wea. Rev*., **110**, 1933-1944.

Pasch, R. J., E. S. Blake, H.D. Cobb III, and D.P. Roberts, 2006: Tropical Cyclone Report Hurricane Wilma 15-25 October 2005 [Available online at http://www.nhc.noaa.gov/pdf/TCR-AL252005-Wilma.pdf].

Price, C., M. Asfur, and Y. Yair, 2009: Maximum hurricane intensity preceded by increase in lightning frequency. *Nature Geosci.*, **2,** 329–332.

Rappaport, E. N., and Coauthors, 2009: Advances and challenges at the National Hurricane Center. *Wea. Forecasting*, **24,** 395–419.

Reasor, P. D., M. D. Eastin, and J. F. Gamache, 2009: Rapidly intensifying Hurricane Guillermo (1997). Part I: Low-wavenumber structure and evolution. *Mon. Wea. Rev.*, **137,** 603–631.

Rodgers, E. B., W. S. Olson, V.M. Karyampudi, and H. F. Pierce, 1998: Satellite-derived latent heating distribution and environmental influences in Hurricane Opal (1995). *Mon. Wea. Rev.*, **126**, 1229–1247.

——, W. S. Olson, J. Halverson, J. Simpson, and H. Pierce, 2000: Environmental forcing of Supertyphoon Paka's (1997) latent heat structure. *J. Appl. Meteor.,* **39,** 1983–2006.

Rogers, R., 2010: Convective-scale structure and evolution during a high-resolution simulation of tropical cyclone rapid intensification. *J. Atmos. Sci.*, **67**, 44–70.

——, R., S. Aberson, J. Kaplan, and S. Goldenberg, 2002: A pronounced upper-tropospheric warm anomaly encountered by the NOAA G-IV aircraft in the vicinity of deep convection. *Mon. Wea. Rev.*, **130**, 180–187.

——, S. Chen, J. Tenerelli, and H. E. Willoughby, 2003: A numerical study of the impact of vertical shear on the distribution of rainfall in Hurricane Bonnie (1998). *Mon. Wea Rev.*, **131,** 1577–1599.

Rotunno, R., and K. A. Emanuel, 1987: An air–sea interaction theory for tropical cyclones. Part II: Evolutionary study using a nonhydrostatic axisymmetric numerical model. *J. Atmos. Sci.*, **44**, 542–561.

Schubert, W. H. and J. J. Hack, 1982: Inertial stability and tropical cyclone development. *J. Atmos. Sci.*, **39**, 1687-1697.

Shapiro, L. J., and H. E. Willoughby, 1982: The response of balanced hurricanes to local sources of heat and momentum. *J. Atmos. Sci.,* **39**, 378–394.

——, 2000: Potential vorticity asymmetries and tropical cyclone evolution in a threelayer model. *J. Atmos. Sci.*, **57**, 3645–3662.

Shen, B.-W., W.-K. Tao, W. K. Lau, R. Atlas, 2010: Predicting tropical cyclogenesis with a global mesoscale model: Hierarchical multiscale interactions during the

formation of Tropical Cyclone Nargis (2008). *J. Geophys. Res*., **115**,D14102, doi:10.1029/2009JD013140.

Skamarock, W. C., J. B. Klemp, J. Dudhia, and Co-authors, 2005: A description of the advanced research WRF Version 3. NCAR Tech Notes-475+STR, 125pp.

Smith, R. K., 1980: Tropical cyclone eye dynamics. *J. Atmos. Sci.*, **37,** 1227–1232.

——, W. Ulrich, and G. Sneddon, 2000: On the dynamics of hurricane-like vortices in vertical shear flows. *Quart. J. Roy. Meteor. Soc*, **126,** 2653–2670.

Squires, K., and S. Businger, 2008: The Morphology of eyewall lightning outbreaks in two Category 5 hurricanes. *Mon. Wea. Rev.*, **136**, 1706–1726.

Steranka, J., E. B. Rodgers, and R. C. Gentry, 1986: The relationship between satellite-measured convective bursts and tropical cyclone intensification. *Mon. Wea. Rev.*, **114,** 1539–1546.

Thompson, G., R. M. Rasmussen, and K. Manning, 2004: Explicit forecasts of winter precipitation using an improved bulk microphysics scheme. Part I: Description and sensitivity analysis. *Mon. Wea. Rev.*, **132,** 519–542.

Velden, C. S., and W. L. Smith, 1983: Monitoring tropical cyclone evolution with NOAA satellite microwave observations. *J. Climate Appl. Meteor.*, **22**, 714–724.

Willoughby, H. E., 1978: A possible mechanism for the formation of hurricane rainbands. *J. Atmos. Sci.*, **35,** 838–848.

——, 1979: Forced secondary circulations in hurricanes. *J. Geophys. Res.*, **84,** 3173–3183.

——, J. A. Clos, and M. Shoreibah, 1982: Concentric eye walls, secondary wind maxima, and the evolution of the hurricane vortex. *J. Atmos. Sci.*, **39,** 395–411.

——, F. D. Marks, and R. J. Feinberg, 1984: Stationary and moving convective bands in hurricanes. *J. Atmos. Sci.*, **41**, 3189–3211.

——, 1988: The dynamics of the tropical cyclone core. *Aust. Meteor. Mag.*, **36,** 183–191.

——, 1998: Tropical cyclone eye thermodynamics. *Mon. Wea. Rev.*, **126,** 3053 3067.

Yamamoto, R., 1963: A dynamical theory of spiral rain band in tropical cyclones. *Tellus*, **15,** 153-161.

Yang, M.-J., D.-L. Zhang, and H.-L. Huang, 2008: A modeling study of Typhoon Nari (2001) at landfall. Part I: Topographic effects. *J. Atmos. Sci.*, **65,** 3095-3115.

Yeh, T. C., 1950: The motion of tropical storms under the influence of a superimposed southerly current. *J. Meteor.*, **7,** 108–113.

Zhang, D.-L., and J. M. Fritsch, 1988: Numerical sensitivity experiments of varying model physics on the structure, evolution and dynamics of two mesoscale convective systems. *J. Atmos. Sci.*, **45**, 261–293.

——, Y. Liu, and M. K. Yau, 2000: A multiscale numerical study of Hurricane Andrew (1992). Part III: Dynamically induced vertical motion. *Mon. Wea. Rev.*, **128,** 3772–3788.

——, L. Tian, and M.-J. Yang, 2011: Genesis of Typhoon Nari (2001) from a mesoscale convective system. *J. Geophys. Res.*, **116**, D23104, DOI: 10.1029/2011JD016640.

——, and H. Chen, 2012: Importance of the upper-level warm core in the rapid intensification of a tropical cyclone. *Geophys. Res. Lett.*, **39**, L02806, doi:10.1029/2011GL050578.

——, and C. Q. Kieu, 2006: Potential vorticity diagnosis of a simulated hurricane. Part II: Quasi-balanced contributions to forced secondary circulations. *J. Atmos. Sci.*, **63**, 2898-2914.